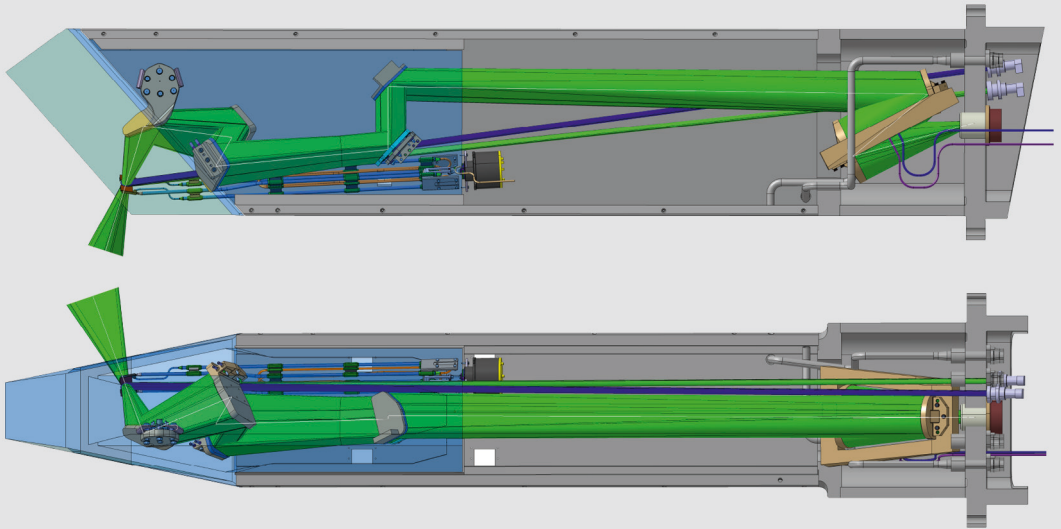


# Diagnostic Mirror Concept Development for Use in the Complex Environment of a Fusion Reactor

Andreas Joachim Krimmer







Forschungszentrum Jülich GmbH  
Institute of Energy and Climate Research  
Plasma Physics IEK-4

# Diagnostic Mirror Concept Development for Use in the Complex Environment of a Fusion Reactor

Andreas Joachim Krimmer

Schriften des Forschungszentrums Jülich  
Reihe Energie & Umwelt / Energy & Environment

Band / Volume 341

---

ISSN 1866-1793

ISBN 978-3-95806-180-4

Bibliographic information published by the Deutsche Nationalbibliothek.  
The Deutsche Nationalbibliothek lists this publication in the Deutsche  
Nationalbibliografie; detailed bibliographic data are available in the  
Internet at <http://dnb.d-nb.de>.

Publisher and  
Distributor: Forschungszentrum Jülich GmbH  
Zentralbibliothek  
52425 Jülich  
Tel: +49 2461 61-5368  
Fax: +49 2461 61-6103  
Email: [zb-publikation@fz-juelich.de](mailto:zb-publikation@fz-juelich.de)  
[www.fz-juelich.de/zb](http://www.fz-juelich.de/zb)

Cover Design: Grafische Medien, Forschungszentrum Jülich GmbH

Printer: Grafische Medien, Forschungszentrum Jülich GmbH

Copyright: Forschungszentrum Jülich 2016

Schriften des Forschungszentrums Jülich  
Reihe Energie & Umwelt / Energy & Environment, Band / Volume 34 1

D 82 (Diss. RWTH Aachen University, 2016)

ISSN 1866-1793  
ISBN 978-3-95806-180-4

The complete volume is freely available on the Internet on the Jülicher Open Access Server (JuSER)  
at [www.fz-juelich.de/zb/openaccess](http://www.fz-juelich.de/zb/openaccess).



This is an Open Access publication distributed under the terms of the [Creative Commons Attribution License 4.0](https://creativecommons.org/licenses/by/4.0/),  
which permits unrestricted use, distribution, and reproduction in any medium, provided the original work is properly cited.

# Kurzfassung

Optische Spiegel werden in Diagnostiken von Fusionsreaktoren eingesetzt, um Licht durch die das Plasma umgebenden Strukturen zu leiten. Mit zunehmender Baugröße, Reaktorleistung und Plasmabrenndauer erhöhen sich dabei die Anforderungen an die Spiegel verglichen mit aktuell realisierten Systemen und es kommen neue hinzu. Im Rahmen der Arbeit wird die Auslegung von diagnostischen Spiegeln innerhalb der Vakuumkammer des Versuchsreaktors ITER (lat. "der Weg") und nachfolgender Fusionskraftwerke diskutiert.

Auf Basis der Umgebungsbedingungen nahe dem Fusionsplasma werden bestehende Konstruktionen sowie Optionen für die Spiegeloberfläche auf ihre Eignung untersucht. Problematisch sind hier nicht einzelne Randbedingungen sondern deren Kombination mit den daraus entstehenden Wechselwirkungen. Abgeleitet aus dem Stand der Technik werden Teillösungen für zentrale Punkte der Konstruktion allgemein dargestellt. Einbezogen sind die Auswahl des Substrats, dessen Montage, Einstellung und thermischen Kontaktierung sowie Positionierung des Zusammenbaus kompatibel mit Wartung in Heißen Zellen.

Aufbauend auf diesen Überlegungen wird eine Konstruktion für die Spiegel der Charge Exchange Recombination Spectroscopy (CXRS) Diagnostik für den Plasmakern in ITER erstellt und mittels Simulation untersucht und bewertet. Zusätzlich werden anhand von Prototypen Versuche durchgeführt, um kritische Teilaspekte des vorgeschlagenen Konzepts auch experimentell nachzuweisen. Dies umfasst die Positionierung mittels Stiften, Herstellung eines innen liegenden und an die Spiegelform angepassten vakuumdichten Fluidkanals und Versuche mit einer Interferenzbeschichtung aus  $\text{SiO}_2$  und  $\text{TiO}_2$  auf Edelstahl unter ausgesuchten ITER-Bedingungen.

Mit den allgemeinen Überlegungen zur Konstruktion wurde eine Basis geschaffen die auch zur Spiegelentwicklung anderer Diagnostiken Anwendung finden kann. Für das Spiegelkonzept von core CXRS konnte die generelle Eignung gezeigt werden und es wurden die kritischen Punkte identifiziert, die weitere Entwicklungsleistung benötigen.

# Abstract

Light-based diagnostic systems of fusion reactors require optical mirrors to channel light through the structures surrounding the plasma. With increasing plasma volume, power and plasma burn time, the environmental conditions grow more demanding and new requirements arise. In this dissertation, the design of optical mirrors inside the vacuum chamber of the prototype reactor ITER (Latin "the way") and future fusion power plants are investigated.

Comparing the state of the art with the boundary conditions close to the fusion plasma, existing mirror designs and choices for the reflective surface are evaluated. For the design, it is not the individual boundary conditions that are critical, but rather, their combination and the resulting interactions. Drawing from the existing designs, possible realizations for central functionality are discussed. Included in the discussion are substrate choice, mounting, adjustment and thermal contacting as well as positioning of the mirror assembly compatible with hot cell maintenance.

Building on the general discussion, mirror concepts for the charge exchange recombination spectroscopy (CXRS) diagnostic system for the ITER plasma core are proposed and simulated. In addition, prototypes are manufactured and tested to assess critical aspects of the proposed design. Testing includes positioning by pins, manufacturing of a stainless steel substrate with fluid channels adapted to the mirror shape, and tests with an  $\text{SiO}_2/\text{TiO}_2$  dielectric coating under selected ITER conditions.

As a result of the work, the fusion reactor mirror design considerations given in the principal design discussion can be used as a basis for other diagnostic systems as well. In the case of the core CXRS mirror concept for ITER, the basic suitability was shown and critical topics were identified where additional work is necessary.

# Acknowledgements

This thesis would not have been possible without the support of a number of people, especially from the Forschungszentrum Jülich and the RWTH Aachen University, whom I would like to thank here.

My sincere gratitude goes to Prof. Dr. rer. nat. Hans-Josef Allelein for supervision and the discussions we had during the Ph.D. symposia and other meetings on- and off-subject. I especially want to thank my technical supervisors Dr. Olaf Neubauer and Dr. Philippe Mertens for the discussions, support and review of this work. They gave direction and encouragement when it was required which I am deeply grateful for. I am also grateful to Prof. Dr. rer. nat. Ulrich Samm, who enabled me to undertake this work, supported me throughout and reviewed the thesis. Special thanks go to Prof. Dr.-Ing. Lorenz Singheiser who agreed to review on short notice.

Many thanks to Guido Offermanns, Dr. Eberhard Rosenthal, Dr.-Ing. Josef Remmel, Dr. Wolfgang Biel and the other colleagues at the Institute of Energy and Climate Research – Plasma Physics (IEK-4) and Central Institute of Engineering, Electronics and Analytics (ZEA) for their support. Without the discussions, their inputs and help realising the prototypes and testing, the present thesis would not have been possible. Special thanks go to Christoph Bläsius for his sustained work on the subject in a number of roles.

I am immensely grateful to my parents for their support, the rest they provided, and their belief in me.



# Contents

<b>1</b>	<b>Introduction</b>	<b>1</b>
1.1	Thermonuclear fusion . . . . .	1
1.2	Light-based diagnostic systems in fusion . . . . .	2
1.3	Aim and structure of the thesis . . . . .	5
<b>2</b>	<b>Diagnostic mirrors in thermonuclear fusion</b>	<b>7</b>
2.1	JET . . . . .	7
2.2	ITER . . . . .	9
2.2.1	The core CXRS and BES diagnostic systems of ITER . . . . .	10
2.3	Fusion power plant . . . . .	12
2.3.1	Feasibility and necessity of diagnostic mirrors in DEMO . . . . .	13
<b>3</b>	<b>Environmental conditions of the mirrors</b>	<b>15</b>
3.1	Vacuum compatibility . . . . .	16
3.1.1	Limitations on material choice and material condition . . . . .	16
3.1.2	Impact on general design . . . . .	17
3.2	Thermal environment . . . . .	17
3.2.1	Machine temperature . . . . .	17
3.2.2	Surface heat loads . . . . .	18
3.3	Nuclear environment . . . . .	19
3.3.1	Limitations on material choice . . . . .	21
3.3.2	Volumetric heat loads by radiation . . . . .	21
3.3.3	Design for the nuclear environment . . . . .	22
3.4	Electromagnetic environment . . . . .	23
3.5	Fluid ingress events . . . . .	25
3.6	Mirror surface contamination . . . . .	26
3.7	System lifetime and maintenance . . . . .	27
<b>4</b>	<b>Mirror design state of the art</b>	<b>28</b>
4.1	Mirror mechanical design . . . . .	28
4.2	Mirror surface treatment . . . . .	34
4.3	Conclusion on environmental conditions and state of the art . . . . .	37
<b>5</b>	<b>Principal considerations on mirror design in fusion reactors</b>	<b>38</b>
5.1	Mirror substrate material selection . . . . .	38
5.2	Adjustment during assembly . . . . .	42
5.2.1	Adapting the interface . . . . .	43

5.2.2	Flexible hinges . . . . .	45
5.2.3	Extended shaped contact . . . . .	46
5.2.4	Pre-loaded small contacts . . . . .	47
5.2.5	Conclusions on adjustment mechanisms . . . . .	49
5.3	Thermal design . . . . .	50
5.3.1	Conclusions thermal design . . . . .	53
5.4	Conclusions on principal design considerations . . . . .	53
<b>6</b>	<b>Concept design for ITER core CXRS secondary mirrors</b>	<b>54</b>
6.1	ITER UPP#3 layout . . . . .	54
6.2	Baseline design fixed mirrors . . . . .	57
6.2.1	Stainless steel substrate . . . . .	59
6.2.2	Interface for mirror positioning and mounting . . . . .	60
6.2.3	Mirror thermal control . . . . .	63
6.2.4	Remote handling mirror exchange . . . . .	64
6.3	Design of two-axis adjustable mirror . . . . .	66
6.4	Thermo-mechanical simulation of Mirror 2 . . . . .	68
6.4.1	FEM model and boundary conditions . . . . .	69
6.4.2	Temperature progression and distribution . . . . .	73
6.4.3	Mechanical stresses . . . . .	74
6.4.4	Mirror surface shape . . . . .	75
6.4.5	Conclusion from FEM modelling . . . . .	79
<b>7</b>	<b>Prototypes and testing</b>	<b>81</b>
7.1	Interface prototype . . . . .	81
7.1.1	Testing and results . . . . .	83
7.1.2	Conclusions on interface prototype . . . . .	84
7.2	Mirror substrate prototype . . . . .	84
7.2.1	Determination of weld method and parameters . . . . .	84
7.2.2	Mirror substrate diffusion bonding . . . . .	87
7.2.3	Conclusions substrate prototype . . . . .	90
7.3	Dielectric mirror coating on stainless steel substrate . . . . .	90
7.3.1	Manufacturing and initial characterisation of the mirrors . . . . .	90
7.3.2	Long-term thermal testing . . . . .	92
7.3.3	Blister formation and flaking . . . . .	96
7.3.4	Exposure to water vapour . . . . .	97
7.3.5	Reflectivity measurements at elevated temperature . . . . .	98
7.3.6	Composition of the coating . . . . .	99
7.3.7	Conclusions on dielectric mirror coating . . . . .	100
<b>8</b>	<b>Summary and discussion</b>	<b>101</b>
	<b>Bibliography</b>	<b>103</b>
	<b>List of symbols</b>	<b>113</b>
	<b>List of abbreviations</b>	<b>115</b>

---

<b>Appendices</b>	<b>117</b>
A Fitting of optical tolerances . . . . .	117
A.1 ANSYS APDL script for tolerance fitting . . . . .	118
A.2 Achieved fitting accuracy . . . . .	120
B M2 welded prototype drawings . . . . .	121

# List of Figures

1.1	Basic configuration of the (a) stellarator and (b) tokamak [63]. . . . .	2
1.2	Vacuum window as first optical element with all other diagnostic components in air: MSE system in JT-60U, adapted from [94]. . . . .	3
1.3	Basic diagnostic layout with optical mirror inside the torus vacuum to aim the field of view as used in a number of current fusion diagnostic systems. . . . .	4
1.4	Principle overview of an in-vacuum mirror train to divert light from the plasma chamber to the outside of the vacuum vessel. . . . .	5
1.5	Extent of the system ‘mirror’ with main functional groups and design considerations. The main components are labelled in bold. . . . .	6
2.1	Overview of the JET tokamak with ex-vessel components and the remote handling booms (yellow; extended into the torus) [62]. . . . .	9
2.2	Overview of the ITER tokamak with the diagnostic ports as the main location of optical diagnostic systems in the ITER labelled. Image adapted from [39]. . . . .	10
2.3	Overview of the core CXRS diagnostic system front-end in ITER. . . . .	11
2.4	Pre-conceptual layout of DEMO for remote handling maintenance assessment [57]. . . . .	13
3.1	Wall incidence angular distribution for neutral D and Be in ITER at the upper (UP) and equatorial ports (EP) [47]. $\Theta=0^\circ$ at perpendicular incidence to wall. . . . .	19
3.2	Effects of the nuclear environment on the mirror design. . . . .	20
3.3	$\gamma$ heating in the ITER CXRS-core UPP ( $\log[W\text{ cm}^{-3}]$ ) [16] with structure outlines overlaid. . . . .	22
3.4	Magnetic field and derivative during a VDE at the core CXRS first mirror [76]. r: radial, z: vertical, $\phi$ : toroidal. . . . .	23
3.5	Moments acting on components in a changing magnetic field through the Lorentz force by the induced eddy currents. . . . .	24
4.1	Example of a sophisticated spring-loaded clamped small mirror mount. (From [75]) . . . . .	29
4.2	Mirror design with polycrystalline silicon substrate for the divertor Thomson scattering diagnostic system. Images adapted from (a) [70], (b) [71]. . . . .	29

4.3	Metallic substrate with flexures machined from the substrate material for strain-free mounting ([111] from [75]). . . . .	30
4.4	Design of the JET KL-11 endoscope second mirror: Aluminium floating substrate with aluminium holder and structure. . . . .	30
4.5	Shortwave Fold Flat Mirror Assembly of the James Webb Space Telescope NIRCcam instrument [29]. . . . .	31
4.6	Rail welded to the JET vacuum vessel for remote handling positioning and mounting of diagnostic assemblies [3]. . . . .	32
4.7	Positioning principles suggested by ITER for remote handling operations [93]. . . . .	33
4.8	Heat exchanger concepts for mirrors in high-energy laser systems [5]. . . . .	33
4.9	Principle of a heat pipe with wick. . . . .	34
4.10	Structure of (a) multilayer dielectric coatings and (b) enhanced metallic mirrors. H: high index of refraction; L: Low index of refraction. . . . .	35
4.11	Damaged dielectric coating after heating to 250 °C [74]. . . . .	36
5.1	Stiffness against external forces versus thermo-mechanical stability. Values from [32] (Si, SiO <sub>2</sub> , Al 6061-T6), [88] (Schott N-BK7), [7] (316L(N)-IG, CuAl) . . . . .	40
5.2	2D sketches of the adjustment principles. Each principle has a number of possible realizations that can differ even in the basic features such as the number of degrees of freedom for adjustment. . . . .	43
5.3	Designs for bolted, shimmed interfaces. Left: single, machined-to-fit shim. Right: three stacks of shims selected to compensate deviations (with angular compensation on bolts). . . . .	44
5.4	Assortment of spring elements: (a) Single rotation stage with flat spring. (b) Flexible post for two rotational degrees of freedom and limited lateral movement. (c) Flexure pivot by C-Flex Bearing Co., Inc. for one rotation. . . . .	46
5.5	Extended shaped contacts as bearing: (a) Gliding axis in pre-loaded bushing. (b) Goniometer arrangement with, e.g. dovetail sliding contact. . . . .	47
5.6	Kinematic mounting for two rotational adjustments with three point contacts and a line contact. . . . .	48
5.7	Combination of the large surface and flex element to minimise stress from adjustment in the flexible element. . . . .	50
5.8	Design options for temperature contact. . . . .	51
6.1	Overview of UPP#3 with the main optical path ('Large M1') in green and standardised UPP shell in grey. . . . .	55
6.2	Available design space in UPP#3 (DSM) compared to the optical path size. Additional systems in UPP#3 and functions restricting the design space are hidden for clarity. . . . .	56
6.3	Baseline design for the core CXRS second mirror. . . . .	58
6.4	Mirror positioning interface for the secondary mirrors. a) Top view and b) isometric view. The mirror substrate is shown in brown, bolts and pins in green, and DSM with threaded inserts in blue. . . . .	61

6.5	Features, dimensions and tolerances of the brass positioning pins in the substrate and DSM. . . . .	62
6.6	Mirror interface with shim (yellow). The shim is bolted to the mirror, and the mounting pads with vacuum venting are moved to the shim as structure with the best manufacturing possibilities. . . . .	63
6.7	Routing of the cooling channel inside the mirror substrate. All dimensions in mm. . . . .	64
6.8	Digital mock-up of RH mounting of the mirror. (a) Positioning the mirror inside the hoisting tool to the DSM. (b) Moving the mirror into the DSM on rails. (c) Retracting of the frame after engaging the mirror mounting bolts. [14]. . . . .	65
6.9	(a) Moving the mirror into final position by the bolt at the longer pin. (b) Disassembly by push rod. . . . .	66
6.10	M4 design allowing adjustment with shims. . . . .	67
6.11	Extent of the model used in the simulation of the second mirror. The mirror is mounted to the DSM via contacts and bolt pretension. . . . .	68
6.12	Mesh of the M2 FEM model with internal cooling channel. . . . .	69
6.13	Placement of the thermal and mechanical boundary conditions (without fluid channels). . . . .	70
6.14	Application of MCNP brick mesh locally resolved volumetric heating. (a) Unfiltered MCNP brick mesh and MCNP mirror body. (b) Inter- and extrapolated heating as applied to mirror body. . . . .	72
6.15	Temperature distribution for the $70\pm 5$ °C feed-water temperature thermal transient simulation 336 s into the flat-top phase. (a) Internally cooled mirror. (b) Bulk substrate. Both substrates from 316L(N)-IG. . . . .	73
6.16	Von Mises operational stress for the mirror substrate with mounting bracket during operation with elastic material model. Note: Scale is shifted and logarithmic above 1 MPa. . . . .	74
6.17	Shape of the ‘TIRR’ aberration as used in ZEMAX with the astigmatism shown at 45° for a normalised, circular mirror. . . . .	76
6.18	Tip/Tilt deviations as calculated for the mirror. The deviations are well within limits in all cases. Green/yellow lines: Tolerances of M2 and M7. . . . .	77
6.19	Change in power (spherical aberration) and remaining surface irregularity after subtraction of the movements, rotations and change in power as peak-to-valley value. Green/yellow lines: Tolerances of M2 and M7. . . . .	78
6.20	Shape of the residual deviations after fitting of movements, rotations and spherical aberration. Scale in [mm]. . . . .	79
7.1	Interface prototype. (a) Interface configuration at the start of testing. (b) Experimental set-up with lead weight and orientation of M2 of core CXRS. . . . .	82
7.2	(a) Condition of the longer positioning pin after the first assembly at full weight. (b) Shavings from the conical section of the pin. . . . .	83
7.3	M2 prototype structures for welding of the cooling channel. . . . .	85

---

7.4	Test block geometry No. 3. Two blocks realise a weld test with internal channel. The sideways drill hole improves evacuation during welding, allowing easy vacuum leak testing after welding. . . . .	85
7.5	Welds with defects. (a), (b): UDW welds with remaining porosity where (b) includes a Ni-foil between the stainless steel blocks. (c) UDW weld with e-beam re-welding from the outside. . . . .	86
7.6	Metallographic sections of successful UDW welds and the machine parameters. . . . .	87
7.7	Vacuum press at KIT used in welding the prototypes, and plot of weld parameters and deformation progress for the second block. Image on left: IMVT [38] . . . . .	88
7.8	2D resolved time of flight ultrasonic examination of the front of test block 2. The weld surface does not give a signal, the depth plotted (around 40 mm) is due to machine settings. . . . .	89
7.9	Metallographic section of the full size prototype uniaxial pressure diffusion bond. The arrows show the location of the weld layer. . . . .	89
7.10	17.5 mm, 50 mm and 100 mm SiO <sub>2</sub> /TiO <sub>2</sub> dielectric coated mirrors on 1.4429 stainless steel substrate used in the testing. . . . .	92
7.11	Initial reflectance of representative mirror samples. Markers are shown every 20 data points. . . . .	93
7.12	Vacuum chamber test set-up for thermal stressing of the coating. . . . .	94
7.13	Mirror support structure for long-term and repeated cycles thermal testing. . . . .	94
7.14	Temperatures as measured in the centre of the mirror samples during a short test. At 68 h, the heating was interrupted shortly due to controller problems and restarted. . . . .	95
7.15	Reflectance of Mirror samples 1 and 11 after different thermal loads. . . . .	95
7.16	Details of flaked-off defects reaching all the way to the substrate with delamination visible on multiple depths. a) White light microscope at 100x. b) SEM image (surface coated with a thin Rh layer). . . . .	96
7.17	Advance of bubbles and flaking in the coating for a larger group on Sample 11. . . . .	96
7.18	Set-up for testing of coating stability under water vapour atmosphere at 120 °C with most of the Al foil used for thermal insulation removed. . . . .	98
7.19	Relative specular reflectivity of Mirror 8 during a temperature cycle. The embedded diagram shows the reflectivity evolution at different wavelength over the cycle. . . . .	99
A.1	Deviations in sag [mm] of meshes generated by the ANSYS Workbench. (a): Deviations in sag on edge nodes due from the limit of 10 significant digits with a 3D model located at 4 m from the model origin, calculated in mm. (b): Larger, single node deviations on mid-side nodes in the same model. . . . .	118

A.2 Rigid body motion fitting is limited to nodes in a point-symmetric area centred on the optical centre to account for influences of thermal expansion. The Zernike polynomials are evaluated on the whole mirror surface. . . . . 119

# List of Tables

2.1	High-level characteristics of current and projected fusion experiments and reactor concepts. Values given are, in general, achieved separately and not in the same shot. Sources for JET: [40][9], W7-X: [105][87], ITER: [35], DEMO: [30]. . . . .	8
2.2	Main wavelengths of interest for the optical system in UPP #3 of ITER.	12
3.1	Design targets for residual gas pressures after vacuum bake-out. . . . .	16
3.2	Machine temperatures in current and future fusion devices. . . . .	18
3.3	First wall radiative and particle heat loads. The values given represent upper bounds during normal operation. . . . .	19
5.1	General requirements on mirror substrates. . . . .	41
5.2	Comparison of machining the interface and shimming the interface. . . . .	45
6.1	Baseline mirror dimensions, shape and mirror surface materials for the large M1 option core CXRS in-port diagnostic mirrors. . . . .	57
6.2	Optical layout suggested tolerances for assembly position accuracy and stability during the nominal 20 years of operation. . . . .	60
6.3	Tolerances on the pins in the DSM and resulting position accuracy of the mirror substrate for a pin distance of 160 mm and pin diameter of 12 mm. . . . .	62
6.4	Details of Mirror 4 for the ITER core CXRS ‘large M1’ optical layout. . . . .	66
6.5	Overview on loads and boundary conditions for the M2 thermomechanical simulation. The letters in italics refer to the locations marked in Figure 6.13 . . . . .	71
6.6	Tolerances taken into account in the preliminary design of core CXRS second, toroidally shaped mirror. The distance $l$ of the location to the mirror optical centre is normalised to one for the furthest point from the optical centre. . . . .	75
7.1	Composition of 316 L(N)-IG and the materials used in testing. All values are given in mass-%. . . . .	81
7.2	Condition of representative mirrors. Standard deviation is given in parentheses ( $1\cdot\sigma$ , abs.). Specular reflectance (R) is given as mean in the full range of 460 to 663 nm under an angle of incidence of $25^\circ$ . . . . .	91
7.3	Overview on samples used during testing. . . . .	92
7.4	Main nominal thermal conditions of the samples. . . . .	93

7.5 Defects on $\varnothing 50$ mm samples with reduced coating and different first layer on the stainless steel found with microscope inspection after 28 days at 260 °C. . . . .	97
--	----

# Chapter 1

## Introduction

### 1.1 Thermonuclear fusion

Inside a nucleus, the neutrons and protons (nucleons) are bound together by the short ranged strong interaction. The maximum mean binding energy per nucleon is found in  $^{62}\text{Ni}$  at 8794.6 keV, closely followed by  $^{58}\text{Fe}$  and  $^{56}\text{Fe}$  [106]. Nuclear fusion as primary energy source aims at combining light nuclei and make use of the released binding energy.

In thermonuclear fusion, the electromagnetic repulsion of the nuclei is overcome by heating the fuel to energies where the fusion reaction cross section is sufficiently large for technical exploitation. The reaction with the highest maximum fusion cross section  $\sigma_{fus}$  is the combination of deuterium (D) and tritium (T), both heavy isotopes of hydrogen [80]:



Governed by conservation of momentum, the binding energy released is split between a 3.5 MeV alpha particle and a 14.1 MeV neutron.

For enabling fusion as a viable primary energy source, it is necessary to minimise the power spent on achieving and sustaining fusion conditions. Based on the ignition criterion which requires that the energy loss from the fusion volume is replaced by the  $\alpha$  particles of the fusion reaction, the temperature at which the highest fusion power output is achieved is somewhat below 30 keV\* [107]. At this temperature, hydrogen gas exists as a fully ionised plasma – a state of matter where the chemical bond between nucleus and electrons is broken, resulting in a macroscopically neutral mix of charged particles.

The current most promising method of confining the fusion plasma includes a magnetic field to steer the plasma along closed magnetic field lines, reducing the loss of energy from the plasma. Successful realizations of magnetic confinement are the tokamak and stellarator concepts, see Figure 1.1. In both layouts, the plasma (yellow) is formed into a doughnut shape, surrounded by a vacuum vessel (grey) and sets of magnetic coils (red, green). In case of the tokamak, the plasma acts as conductor and gives rise to a component of the confining magnetic field.

---

\*The temperature is given in eV based on the relation  $T(\text{eV}) = T(\text{Kelvin}) \times k_B$  with the Boltzmann constant  $k_B \approx 8.617 \times 10^{-5} \text{ eV K}^{-1}$ . 1 eV amounts to a temperature of 11 604.5 K.

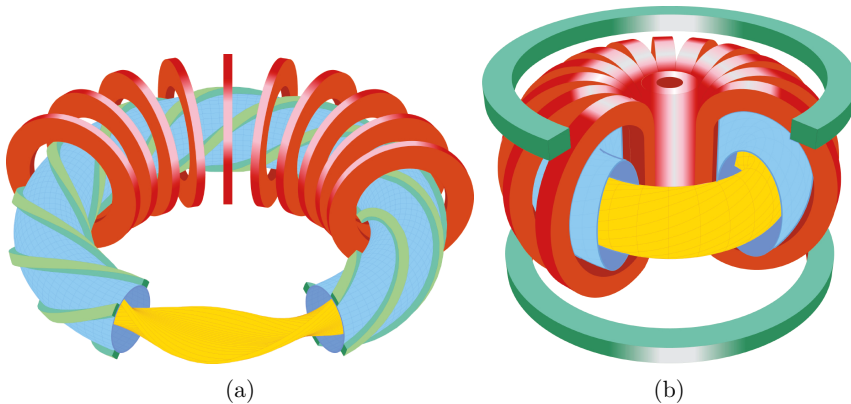


Figure 1.1: Basic configuration of the (a) stellarator and (b) tokamak [63].

The vacuum chamber is required to achieve the necessary cleanliness of the hydrogen gas in the plasma volume. Impurities, including the helium from the DT fusion reaction, have to be removed from the plasma as they decrease the fusion rate by diluting the fuel. Heavier impurities which are only partially ionised at 10 keV also radiate significant amounts of energy away from the plasma. The vacuum chamber also provides the low plasma particle density of  $5 \times 10^{20}$  particles per  $\text{m}^3$  [42] which can be confined with current large-scale steady-state magnet technology (peaking at about 12 T).

Taking the whole reactor as basis, the most relevant loads and environment conditions for components inside the vacuum vessel, close to the fusion plasma, are as follows:

- Fast (eV to keV) particles (ions, electrons, atoms): Heat load, sputtering of material, deposition of layers
- Radiation (neutrons, gammas): Heat load, material damage, maintenance implications due to activation and contamination
- Magnetic field: Restrictions on material choice, EM forces during transients
- Plasma purity: Design for vacuum environment, restrictions on material choice
- Reactor thermal environment: Elevated temperature, temperature gradients over time and location

## 1.2 Light-based diagnostic systems in fusion

Diagnostic systems in fusion experiments are necessary not only for machine control and protection, but also to advance the understanding of plasma and machine behaviour to a level where a commercial reactor can be realised. In current machines, a multitude of diagnostic systems is used to gather information on the machine and

plasma state, including but not limited to measurement of the fusion neutrons, probing by radio waves, magnetic field measurements, and even Langmuir probes in direct contact with the plasma edge. An overview on various diagnostic systems and the challenges for their use in a burning plasma experiment can be found in [99].

Light can act as a carrier of information of the plasma state for a diverse set of operational parameters. As the plasma is sufficiently transparent within the main plasma volume for light in and around the visible range over distances of a few metres, it can be used to probe the inside and through the plasma volume. Optical diagnostic systems, such as interferometry [17] and Thomson scattering [64] which probe the plasma with light from the outside, can give line-integrated and localised measurements of the plasma condition. Photons are also created inside the plasma by a number of interactions – e.g. as a result of electron excitation or capture by the ions and atoms. These photons encode in their wavelength and quantity the local plasma conditions, including e.g. the temperature, density and composition, all of which can be determined via spectroscopy [101]. Visible and infrared light is also used in monitoring the wall condition and temperature.

For these light-based diagnostic systems, it is necessary to provide locations where the light can enter and leave the vacuum vessel. Historically, a common and simple arrangement to couple light through the vacuum vessel consists of an optical window as the first component, directly followed by the remaining optical components to divert and relay light under ambient pressure. Figure 1.2 gives an example of this type of basic layout: the motional stark effect (MSE) system [94] used in the tokamak JT-60U in Japan.

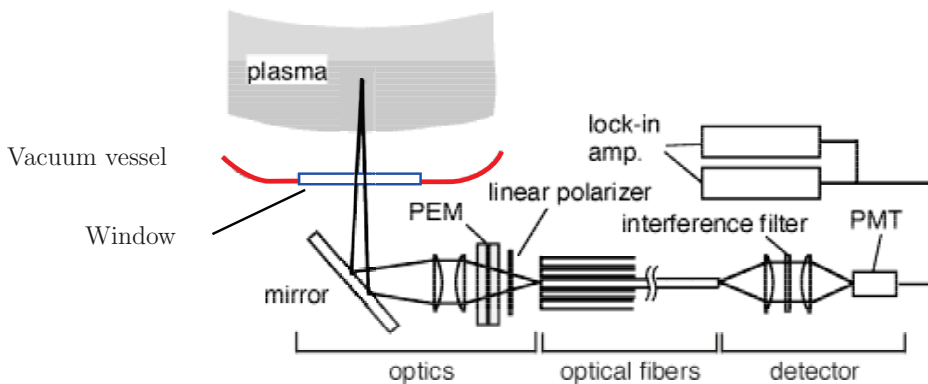


Figure 1.2: Vacuum window as first optical element with all other diagnostic components in air: MSE system in JT-60U, adapted from [94].

While the use of a vacuum window as first element in the optical system is convenient for the mechanical design, since the following optical components can be located outside the torus vacuum, it is not always feasible to place a vacuum window as the first component. In past and current systems, the main cause of problems are spatial restrictions and diagnostic set-ups, where the window has to be placed so close to the plasma that material erosion or deposition (depending on the location and surrounding structures), as well as high heat loads threaten the function of the window. In

these cases, optical elements inside the primary vacuum are used. Figure 1.3 shows the general layout for such a system. An realised example of this scheme is the optical system in the port KL-11 for divertor spectroscopy in the JET tokamak (UK), described in detail in [36]. It includes two in-vacuum aluminium mirrors mounted on an endoscope structure fixed to the vacuum vessel. Another similar diagnostic layout for the charge exchange recombination spectroscopy (CXRS) from the tokamak DIII-D (USA) is described in [31].

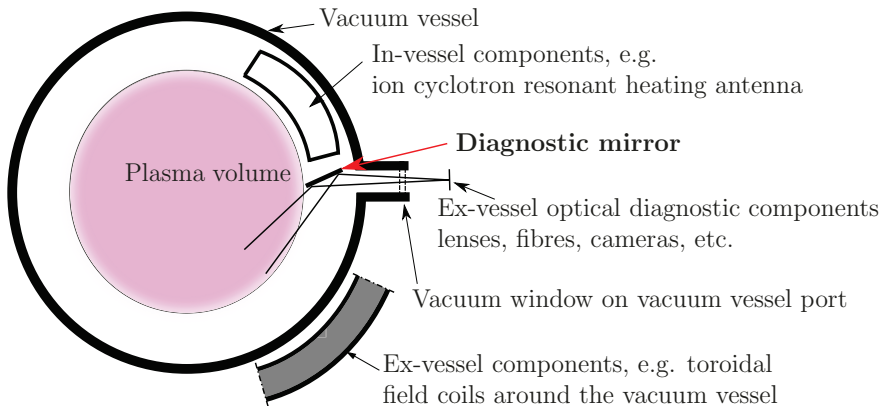


Figure 1.3: Basic diagnostic layout with optical mirror inside the torus vacuum to aim the field of view as used in a number of current fusion diagnostic systems.

With increasing fusion power and plasma operation time integrated over the machine lifetime, the approach of using transmissive optical elements (windows, lenses, fibres) close to the plasma inside the high neutron and gamma flux is not feasible any more because of effects degrading diagnostic performance:

- Transparent materials accumulate defects from the radiation, leading to increased absorption of light with increasing fluence [102], thus blinding the optical system over time.
- Light created via radioluminescence decreases the signal-to-noise ratio of the system. [69]

As an optical vacuum window is still required (locating the full diagnostic system inside the torus vacuum is in general not feasible), the window has to be placed far from the plasma where the shielding of the reactor allows the use of refractive optical elements. Depending on the diagnostic layout, the implementation of a dogleg in the radiation shielding to prevent steaming of radiation may be necessary. The increased distance, and possibly dog-leg, necessitates mirror systems consisting of multiple chained mirrors in front of the window, which are exposed to the primary vacuum of the fusion reactor. The basic set-up is shown in Figure 1.4.

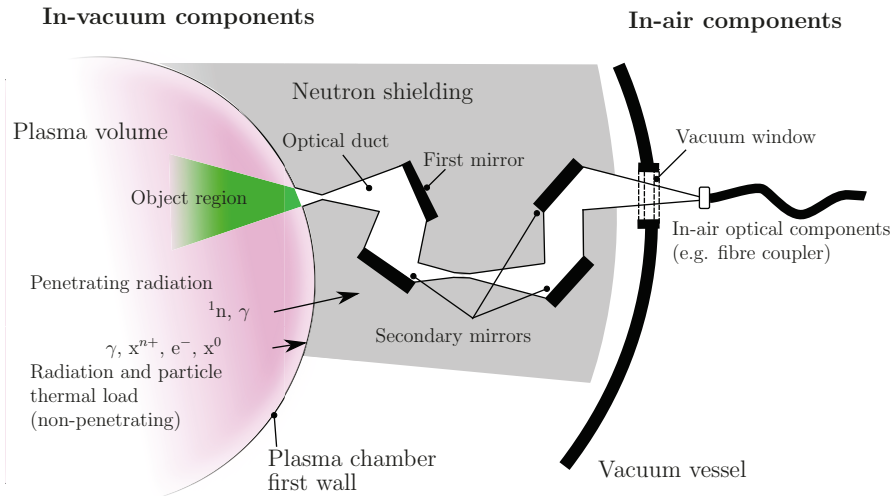


Figure 1.4: Principle overview of an in-vacuum mirror train to divert light from the plasma chamber to the outside of the vacuum vessel.

### 1.3 Aim and structure of the thesis

The present thesis discusses general design solutions for diagnostic mirrors in a fusion power plant, and proposes a mirror design for the secondary mirrors of the core charge exchange recombination spectroscopy (core CXRS) in the experimental reactor ITER.

A mirror in this work is a unit encompassing the reflective surface and all structures necessary to provide, align and sustain the surface. Thus, it includes the mirror mounting interface, alignment mechanisms and provisions as well as all interfaces to support systems, such as cooling the fluid circuit or maintenance, e.g. by remote handling during maintenance. An overview of the components is given in Figure 1.5. Depending on the system, only a subset of the given functionality may be necessary for a specific mirror.

Chapter 2 introduces the fusion experiments and concepts from which the requirements on the mirrors are derived. The target locations of the diagnostic mirrors are given and limitations based on the feasibility of mirror placement due to system restrictions are discussed. In Chapter 3, the boundary conditions, as found in current experiments and predicted for fusion reactors, are described in detail. Comparing the requirements with the state of the art, the shortcomings of the existing designs are worked out in Chapter 4.

Based on the boundary conditions and state of the art, design solutions for key aspects of the mirrors are discussed in Chapter 5. A full concept for mirrors of the core CXRS and beam emission spectroscopy (BES) diagnostic systems in the fusion experiment ITER is given in Chapter 6, and central aspects of the design are validated via calculations and testing of prototypes (Chapter 7). Conclusions are given in Chapter 8 and open questions are discussed.

The Appendix provides the calculation of optical deviations and aberrations from

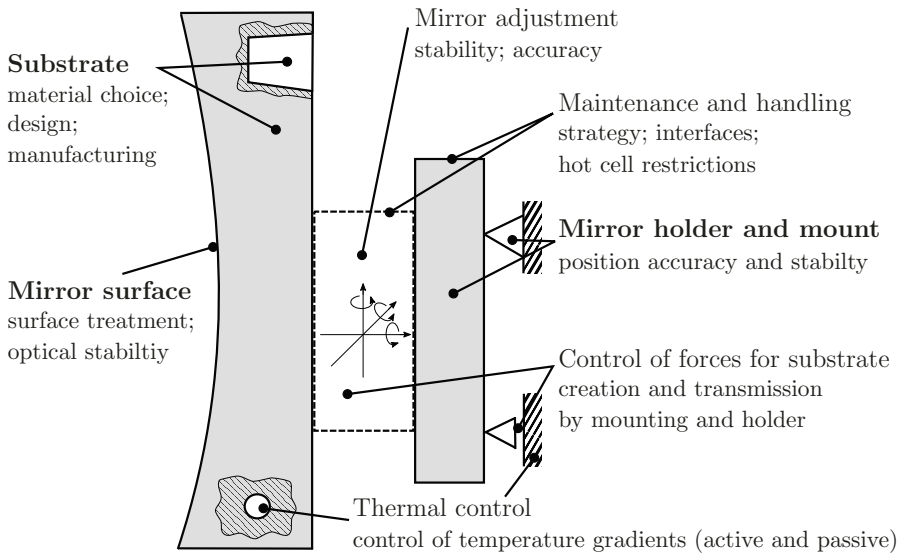


Figure 1.5: Extent of the system ‘mirror’ with main functional groups and design considerations. The main components are labelled in bold.

the finite element method (FEM) results for the large FEM node movement, as found when simulating the fusion environment. In addition, manufacturing drawings for the second mirror cooling channel prototype are given.

# Chapter 2

## Diagnostic mirrors in thermonuclear fusion

This chapter introduces current and future machines widely referenced in the present work. The mirror design state of the art as found in existing experiments is discussed and future machines are introduced as the target systems for the mirror concepts in this work.

The current configuration of JET with the ITER-like wall [62] is the machine in operation closest to a fusion reactor. Of the machines under construction, the tokamak ITER [35] represents the primary design target for the integrated mirror designs discussed in this work. The stellarator Wendelstein 7-X (W7-X) [105] is included where the inherent differences of the stellarator concept add to the parameter space for diagnostic mirrors.

For the fusion power plant, the European concept of a demonstration power plant (DEMO) developed within the Horizon 2020 road-map is used [30]. The requirements and loads of the near-term conservative baseline design (DEMO1) are taken where the two concepts in this proposal differ.

Table 2.1 gives an overview on the major parameters of the different machines. In the following sections, further details of JET, ITER and the DEMO fusion power plant concept relevant for the work are given. For ITER, the charge exchange recombination spectroscopy diagnostic system for the plasma core (core CXRS) is introduced. This diagnostic system serves as design target for the mirrors.

### 2.1 JET

JET, the Joint European Torus, is currently the only tokamak equipped to use a mixture of deuterium and tritium. Following its first plasma operation in 1983, JET is being used as a test-bed for mostly plasma and fusion technology research. The latest major overhaul of the machine was completed in 2011, with the ITER-like wall enabling integrated testing of the materials used in ITER [62].

Figure 2.1 gives an overview of the JET torus and in-air components connected to the torus. Maintenance of components inside the vacuum vessel is predominantly done by remote handling equipment; in the image, the two booms carrying the manipulators are shown extending into the torus. Limited, but hands-on access to the systems

Table 2.1: High-level characteristics of current and projected fusion experiments and reactor concepts. Values given are, in general, achieved separately and not in the same shot. Sources for JET: [40][9], W7-X: [105][87], ITER: [35], DEMO: [30].

Machine	JET	W7-X	ITER	DEMO*
Type	tokamak	stellarator	tokamak	tokamak
Plasma composition (H-species)	H, D, D+T	H, D	H, D, D+T	D+T
Major radius [m]	3	5.5	6.2	9
Minor radius [m]	1.25	0.53 (av.)	2.0	3
Magnetic field on axis [T]	4	3	5.3	5.2
Plasma heating power [MW]	35 for up to 20 s	10 to 30	75 to 133	50
Fusion power [MW]	16.1 short peak; 22MJ over 4 s	$\approx 0$	500	1800
Plasma shot time [s]	60 (max. shot time)	1800 (max. design)	500 (3000 at red. power)	>7200
D-T operation time [year]	minutes to hours	0	0.5	10+
Neutron production <sup>†</sup> [n/s]	$\approx 10^{16}$ (DD), $6.7 \times 10^{18}$ (D-T)	$10^{11}$ to $10^{16}$	$1.77 \times 10^{20}$ (500 MW)	$6.4 \times 10^{20}$
Av. first wall neutron flux [n/s m <sup>2</sup> ]	$> 10^{17}$ (at 14 MeV)		av. $2.6 \times 10^{17}$ at 14.1 MeV	
First wall neutron fluence [n/m <sup>2</sup> ]	up to $10^{20}$		av. $4.1 \times 10^{24}$ at 14.1 MeV	

\*DEMO concept: DEMO1 with a plasma aspect ratio of three.

<sup>†</sup>Neutrons at energy 14.1 MeV for D-T; 2.5 MeV for D-D

mounted on the outside of the vacuum vessel is possible with the radiation level found at JET.

The plasma-facing components in JET are cooled passively by heat conduction to the vacuum vessel. This is possible with the limited shot duration of no more than 60 s, which is reduced even further for higher power discharges. There is no thick radiation shield directly built into the machine and the access ports in the vacuum vessel are generally empty, apart from the structural material and components required for the systems inside the port.

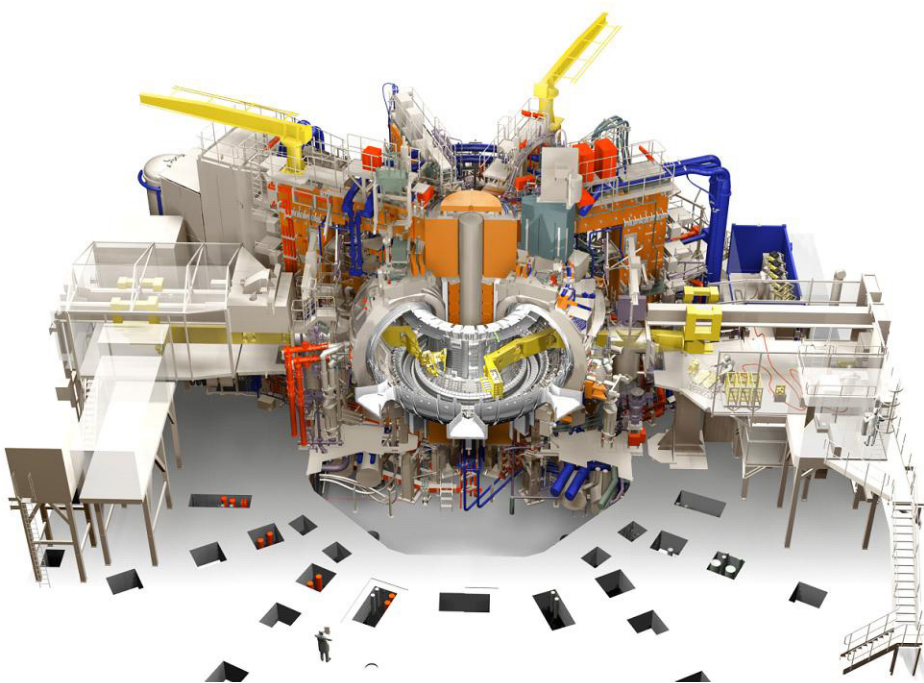


Figure 2.1: Overview of the JET tokamak with ex-vessel components and the remote handling booms (yellow; extended into the torus) [62].

## 2.2 ITER

ITER (lat. ‘The road’ and formerly acronym for International Thermonuclear Experimental Reactor) is a fusion experiment under construction in Cadarache, France [39]. The scientific goal of ITER is to demonstrate fusion plasma with a thermal fusion power 10 times the external heating power delivered to the plasma. In addition, the breeding of tritium and power plant-relevant plasma scenarios should be demonstrated. With 500 MW sustained fusion power over 400 s, ITER would achieve a large step towards a viable reactor. Figure 2.2 shows a simplified overview of the tokamak with in-vessel components, vacuum vessel and magnetic coils.

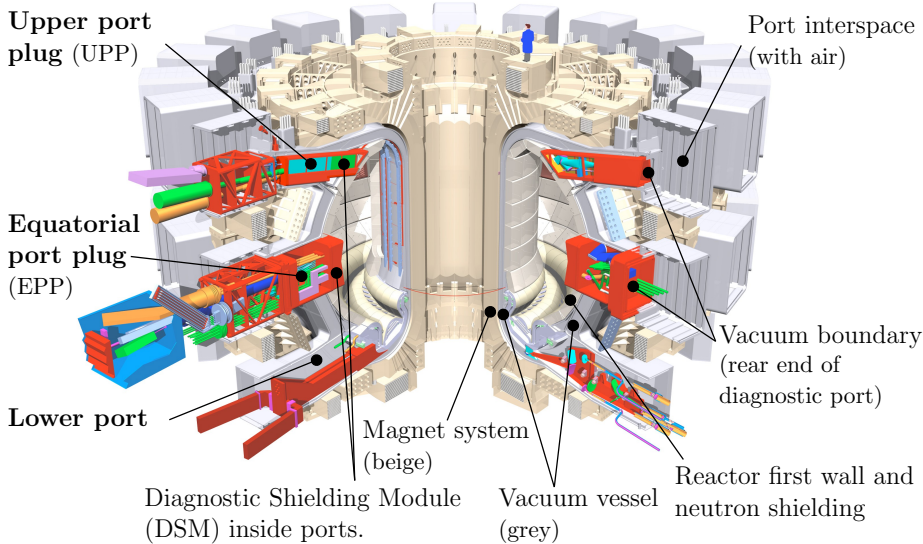


Figure 2.2: Overview of the ITER tokamak with the diagnostic ports as the main location of optical diagnostic systems in the ITER labelled. Image adapted from [39].

To achieve the goals of ITER, diagnostic systems for probing the plasma are required. The main locations for optical diagnostic systems in ITER are the ports of the vacuum vessel. Three levels of ports exist: the lower (divertor), equatorial and upper ports. In case of the equatorial and upper ports, standardised port plugs (PP) are provided for housing the diagnostic components. For maintenance, these PP are removed from the torus and transported to the hot cells. The generic design of the port plugs foresees a diagnostic shielding module (DSM) with an internal water circuit for neutron moderation and cooling. The DSM has to be adapted to the diagnostic systems in each port.

### 2.2.1 The core CXRS and BES diagnostic systems of ITER

The core charge exchange recombination spectroscopy (core CXRS) and the beam emission spectroscopy (BES) diagnostic systems in ITER are used as design targets for the mirrors in the present work.

Core CXRS and BES analyse light originating at the interaction volume between the diagnostic neutral beam (DNB), a beam of neutral hydrogen isotopes ( $H^0$ ) at 100 keV dedicated to diagnostic use, and the plasma. The Upper Port Plug (UPP) #3 channels light from the interaction zone to the outside of the vacuum vessel, where it is transmitted via fibres to spectrometers (see Figure 2.3). The field of view for the optical system starts at the geometrical plasma centre and extends 1.4 m towards the low field side (0.7 times the ITER minor plasma radius of 2 m) with a width of about 400 mm. The optical path length from object to the coupling into optical fibres amounts to roughly 10 m.

The light examined by CXRS is generated when the electrons brought into the

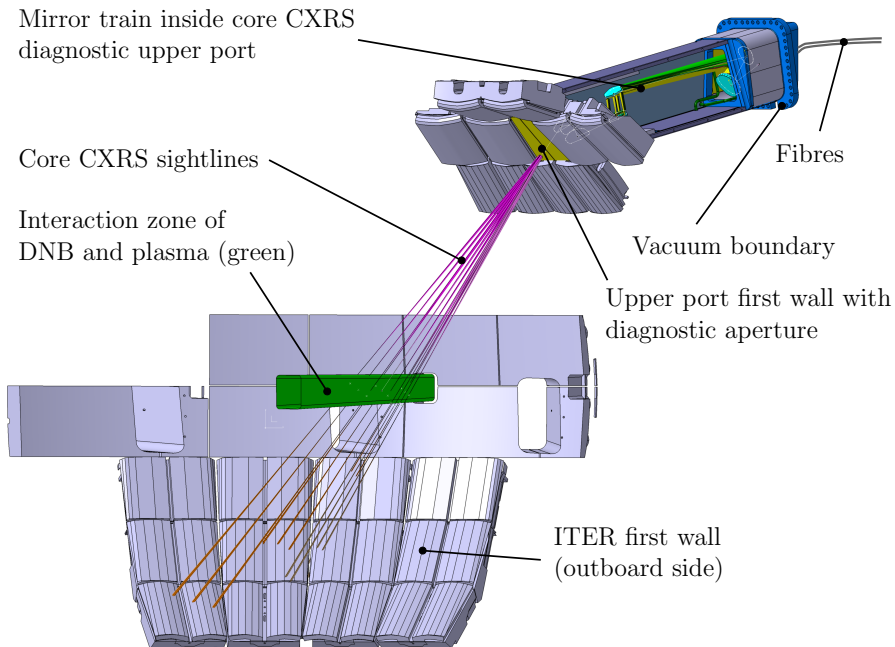


Figure 2.3: Overview of the core CXRS diagnostic system front-end in ITER.

plasma volume by the neutral beam are captured by the fully ionized nuclei  $X^{+z}$  in the plasma to form excited states (\*) of hydrogen-like ions  $X^{+z-1,*}$  (charge exchange):



These excited states quickly decay into less energetic states ('), radiating light at wavelengths affected by the conditions of the radiating ion, the beam energy and the local magnetic environment (recombination reaction):



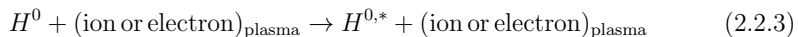
Based on the known line radiation wavelength and transition probabilities under fusion reactor conditions, a range of plasma parameters can be evaluated, including local plasma temperature from the line broadening, ion speed from the Doppler shift and relative impurity concentration via the intensity of the characteristic line radiation peaks of individual elements. Measurements are foreseen for the line radiation of hydrogen-like helium, beryllium, carbon, neon and argon [11]. Table 2.2 gives the wavelength ranges for these impurities. While the light of CXRS is partially polarized, the polarization direction is not evaluated.

BES analyses light originating from the hydrogen atoms of the neutral beam directly. While travelling through the plasma, the atoms in the neutral beam collide with the ions and, to a lesser extent, with the electrons in the plasma, resulting in

Table 2.2: Main wavelengths of interest for the optical system in UPP #3 of ITER.

Wavelength band [nm]	Diagnostic system and accessible spectral lines
460.8 to 473.6	CXRS: He II, Be IV
518.9 to 533.1	CXRS: C VI, Ne X, Ar XVII
649.0 to 663.0	BES: H- $\alpha$

excited states of the neutral beam hydrogen atoms [59]:



The  $H^{0,*}$  excited states decay under emission of line radiation. A suitable transition for analysis is the  $n = 3$  to  $n = 2$  transition (Balmer-Alpha line; see also Table 2.2). The fast atoms of the beam see an electric Lorentz field  $\mathbf{E}_L = v_{\text{beam}} \times \mathbf{B}$  as they move across the magnetic field and line splitting occurs (motional Stark effect). The resulting multiplet of wavelengths contains information about the plasma. For example, the polarization pattern allows determination of the local magnetic field. In addition, beam emission intensity allows the measurement of the local neutral beam density, an important quantity in interpreting the measurements of CXRS.

## 2.3 Fusion power plant

Several concepts are under development for the first-generation fusion power plant under the generic name ‘DEMO’ (demonstration reactor). While the operational parameters in the proposals vary significantly, most concepts assume a tokamak-based DEMO and all of them are in an early conceptual phase. In particular, the mechanical layout is not fixed for any of the concepts. Common to all proposals is a fusion power between 1 and 4 GW, multi-hour to steady-state pulse times, tritium self-sufficiency and maximised availability. With the mechanical concept in the early phase as it is, the choice of the DEMO concept is not critical for diagnostic mirror design considerations in this work. The basic machine parameters assumed for the concept considerations given in Table 2.1 are from the 2014 European DEMO1 concept (see [30]).

Figure 2.4 shows a pre-conceptual mechanical layout used for a remote handling maintenance study of the main in-vessel components: blanket and divertor [57]. While no plasma diagnostic systems are included in the model, it exhibits the most prominent design restrictions for diagnostic systems not present in ITER:

- Achieving tritium self-sufficiency requires the breeding blanket to cover the first wall as much as possible, thereby severely limiting access to the plasma for diagnostic systems even if suitable vacuum vessel ports are present, as is the case in the model
- Overall design and maintenance are aimed at the fast exchange of the blanket and divertor. Together with the requirement of high machine availability this limits the possibilities for maintenance of diagnostic systems

With the limited access and time available for maintenance, full replacement of damaged diagnostic systems is assumed as the maintenance strategy in DEMO. The general vacuum requirements are unchanged from ITER.

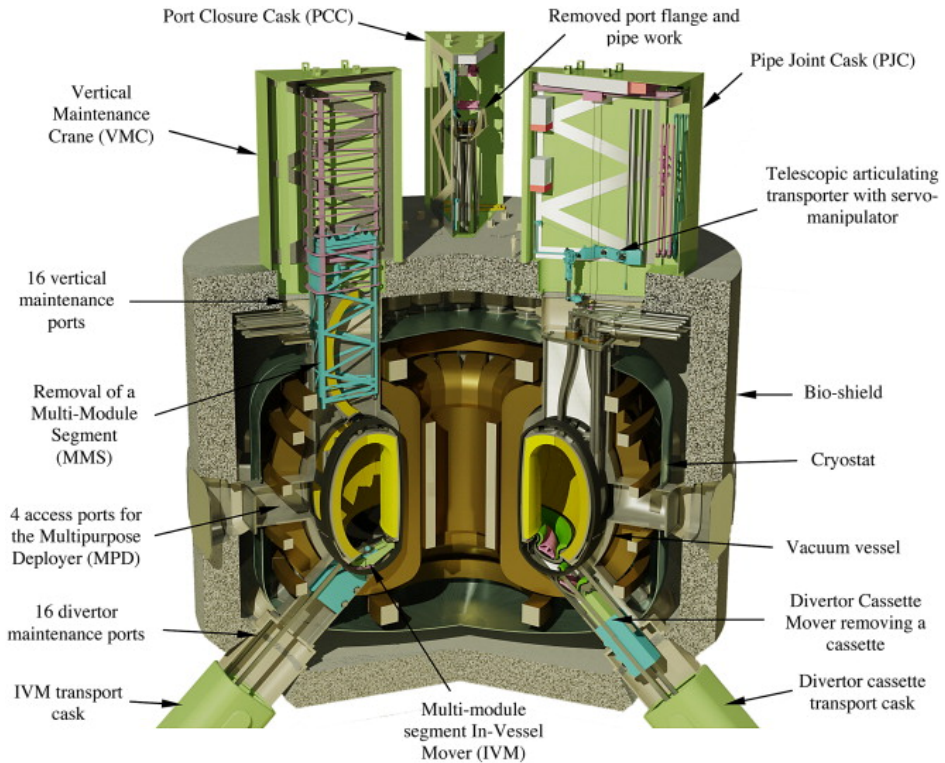


Figure 2.4: Pre-conceptual layout of DEMO for remote handling maintenance assessment [57].

While the DEMO's operational parameters are within the same order of magnitude as ITER, and many requirements, such as vacuum, are not different at all, the major difference in machine parameters to ITER is the lifetime integrated plasma operation time. A major goal of a power plant is to generate electricity, necessitating plasma operation times that possibly exceed the planned total ITER plasma time of about 0.5 full power years (FPY), already within the first year of power generation.

While DEMO will only show a moderate increase in neutron flux at the first wall of about three times the level in ITER, a significant increase in fluence over the lifetime is planned at 50 times the level encountered in ITER.

### 2.3.1 Feasibility and necessity of diagnostic mirrors in DEMO

In current experiments, mirrors are placed within some cm of the plasma edge, exposing them to the flow of light, fast neutral particles coming directly from the plasma as well as material sputtered from the first wall and diagnostic duct. These neutrals

result in a degradation of reflectivity through sputtering of the mirror surface and/or the growth of a layer of impurities sticking to the mirror surface.

While degradation can be accepted in current machines due to the ease of replacement and the short integrated plasma operation time, the mirror reflectivity lifetime problem in ITER is worse with the increasing plasma operation time and complications for maintenance with the D-T operation. Predictions for the mirror lifetime in ITER show high uncertainties [48]. Consequently, the lifetime issue of mirrors in ITER is studied widely and, especially, system-level mitigation technologies are investigated [55]— e.g. protective duct geometries and mirror cleaning systems.

The issues with material deposition and erosion on mirrors do not allow implementation of most of the diagnostic systems relying on light from inside the fusion chamber. Alleviating the issue to some extent, a fusion power plant only requires a reduced set of diagnostic systems for its operation: With a limited set of well-understood plasma scenarios, only diagnostic systems for machine protection and plasma control are foreseen [23]. Which diagnostic systems need to and can be feasibly implemented in the harsh environment of a fusion reactor is subject to discussion [12].

Based on the mirror reflectivity degradation testing conducted in preparation for ITER, it can be deduced that any diagnostic mirror in a fusion reactor needs to be located far away from the plasma in order to achieve a reasonable lifetime even in case all known mitigation techniques are used. Consequently, mirror placement in DEMO is restricted to locations at about 1 m distance from the plasma at the end of a narrow duct. As a result, the maximum loads for mirrors in DEMO are limited to loads present at the end of this duct. With the only moderate increase in mechanical and thermal peak loads in DEMO, it is ensured that the loads do not exceed the loads on ITER mirrors located directly behind the first wall. Despite the increased neutron flux at the first wall, the 1 m of shielding also ensures that the material damage and activation encountered for the mirrors in DEMO will not be higher than predicted for ITER.

Consequently, the DEMO mirrors can rely on the mirror designs created for ITER and no separate layouts are proposed for use in DEMO.

## Chapter 3

# Environmental conditions of the mirrors

In this section, the service conditions for mirrors inside the primary vacuum of fusion devices are discussed based on the machines, as introduced in Chapter 2. In addition to the general dependency on the target machine, most boundary conditions vary significantly with a number of additional parameters. These parameters are, among others, the location of the individual mirrors in the machine and the design of the mirrors' surroundings. For example, the neutron flux is strongly influenced by the type and amount of shielding around a mirror. Locations with a representative environment spanning from just behind the first wall up to the vacuum boundary of the diagnostic ports in the vacuum vessel are taken into account.

For a number of design aspects, the biggest sources of variance are the different diagnostic systems themselves – e.g. the available design space. Where a continuous spectrum of requirements can be given, a reasonable range is stated based on the existing and planned systems. Example requirements include mirror size and optical tolerances. Where requirements are inherently diagnostic system-specific and cannot be formulated in a general way, only values for the core CXRS system of ITER are given. A prime example for this type of requirement are the details of the construction space. These requirements are not addressed in the chapter on general design and are taken into account only for the design of the core CXRS mirror concepts.

Design requirements and environmental conditions unique to mirrors in fusion are discussed in detail. General loads such as gravity, but also common requirements including cost, manufacturability and availability of materials are not touched. These criteria are still taken into account in the general design exploration and specific design of the core CXRS mirrors.

Based on the current experimental character of fusion devices, boundary conditions often are not known as precisely as is desirable. In addition, requirements are bound to change considerably during the machine design phase and, in parts, during the operational phase of the experiments with future modifications. As it is impossible to anticipate all changes, this work can only represent a frozen view on the design requirements of the future machines ITER and, especially, DEMO, which are still in a pre-conceptual phase. The uncertainties also require the inclusion of additional margins where changes are anticipated. Where feasible more robust approaches are

chosen to account for the experimental and first-of-its-kind nature of the device. The introduction of single points of failure, especially for critical systems with a safety function, is avoided. Where applicable and known, the uncertainties are mentioned explicitly and taken into account in the design.

## 3.1 Vacuum compatibility

The need to guide light from close to the plasma towards a protected location where a vacuum window can be located requires mirrors to be placed inside the primary vacuum of the fusion device. Table 3.1 gives examples of the target base pressures after conditioning of the vessel. To achieve the vacuum and gas composition necessary for magnetically confined fusion in the reaction chamber, all components exposed to the vacuum have to be designed, manufactured, cleaned and handled according to vacuum requirements. With an impact on most aspects of the components life cycle, the vacuum requirement strongly influences the design.

For ITER, a comprehensive set of requirements on vacuum compatibility is given in [109]. It is used as the basis for the specific design proposed in this work.

### 3.1.1 Limitations on material choice and material condition

Material choice is limited for all parts in contact with the vacuum based on outgassing rates and the material vapour pressure. Examples of materials that cannot be used include mineral oil-based lubricants, wood and most plastics. Porous materials need to be limited and may require separate, higher-temperature vacuum baking to reduce initial outgassing.

In cases where a part represents a vacuum boundary – e.g. in the case of an internally cooled component – the material selection is further restricted by the leak tightness requirement. Materials with the potential for interconnected pores or cracks cannot be used. This includes materials that rely on manufacturing routes with an increased chance of leaks, as is the case for parts manufactured by powder metallurgy, if the pores cannot be reliably closed completely by the manufacturing route – e.g. hot isostatic pressing.

The surface condition of the component also influences the outgassing rate. The significant conditions include roughness as well as surface structure and composition as left by the manufacturing process, which e.g. can embed lubricants into the surface. In particular, abrasive surface treatments such as grinding result in surfaces with increased outgassing rates and should be minimised. Specifically for fusion, cutting fluids containing halogens, phosphorus and sulphur are not allowed in order to prevent contamination of the plasma.

Table 3.1: Design targets for residual gas pressures after vacuum bake-out.

ITER [19]	$1 \times 10^{-5}$ Pa (hydrogenic species) $1 \times 10^{-7}$ Pa (sum of all impurities)
Wendelstein 7-X [81]	$1 \times 10^{-6}$ Pa

### 3.1.2 Impact on general design

Minimization of outgassing and leak risk requires an adapted design for all vacuum-exposed components. The design needs to facilitate cleaning and cannot include trapped volumes, which act as virtual leaks – e.g. blind holes under bolts or large surfaces in contact. Leak risks can be decreased by reducing the extent and number of vacuum boundaries, especially welds. The design also needs to enable possibilities for inspecting and testing welds, e.g. by irradiation and ultrasonic methods.

The frictional relative motion of surfaces in contact inside a vacuum is highly problematic for most material combinations. Especially with metals where the protective oxide layer cannot reform after it is damaged, enhanced fretting and cold welding occurs on the exposed pure metallic surfaces [24]. The increased wear from the accumulated wear debris, which is slow to leave the contact in the vacuum, can be further influenced by the presence of magnetic fields [86].

In addition to wear problems, the actuation of the motion is complicated by the vacuum with limited in-situ actuation methods available, necessitating vulnerable feed-throughs across the vacuum boundary. Wherever possible, frictional movement in vacuum should thus be avoided. Where necessary, recommendations for material combinations and lubricants are given from the experience of fusion experiments and space systems in, e.g. [60] [65].

Heat transfer between components is limited inside the vacuum as no significant convective heat transfer can take place; only radiation and conductance through the materials are encountered. The reduced heat transfer is also present in the contact conductance between parts: The gas gap conductance, a strong contributor to the heat transfer, especially at interface stresses below 1 MPa, is not significant at gas pressures below 0.1 mbar [58]. As a result, steep thermal gradients can develop more easily and persist for longer times. Parts with limited contact to adjacent components and unfavourable geometry for thermal conduction – e.g. springs – need to be checked carefully for their thermal suitability.

## 3.2 Thermal environment

Fusion diagnostic systems are subject to a variety of thermal influences from the plasma and the surrounding machine. Temperature and, especially, thermal gradients over time and spatial location have a profound impact on the optical performance and need to be taken into account in the optical and mechanical design. In this section, the different non-nuclear thermal influences are discussed and the significant loads identified. Volumetric heating by neutrons and  $\gamma$ -radiation is discussed in Section 3.3.2.

### 3.2.1 Machine temperature

The machine temperature is the main driver for diagnostic component temperatures. In current fusion machines, the diagnostic inserts generally do not feature a separate means of temperature control but are heated and cooled together with the machine. In ITER and DEMO, a cooling medium will be present within all heavy in-vessel

components for vacuum bake-out heating as well as cooling and radiation shielding during operation.

Active and independent temperature control of diagnostic components can be implemented but is only done in cases where it is impossible to avoid – e.g. where required by the diagnostic principle. The infrared thermography system of Tore Supra features an endoscope head with an internal tube holding lenses cooled to 25 °C, thus achieving a reduction of the infrared background [34]. In this case, the low temperature structure is not in contact with the torus vacuum, which is made possible only by the ability to place the vacuum window as the first optical element in Tore Supra.

There are two strong arguments for maintaining the optical elements at machine temperature. First, the complexity of the set-up is increased with a dedicated temperature control system for a number of design aspects, including machine control and maintenance. Second, the more usual case of a stable temperature around room temperature for the optical elements is incompatible with exposure to the vacuum environment, as the increased retention of gasses would hinder vacuum conditioning and can lead to degradation of the optical performance from condensation (see also Section 3.6).

Consequently, the temperature of the diagnostic components is strongly coupled with the machine temperature. In current fusion experiments and ITER, this temperature ranges from room temperature to a maximum during vacuum baking. Table 3.2 gives details on the environment temperatures encountered. The maximum temperature of individual components may be higher during operation depending on operational loads.

Table 3.2: Machine temperatures in current and future fusion devices.

	Operational range	Vacuum bake-out
JET [108]	Up to 320 °C (vacuum vessel wall)	up to 500 °C
ITER [26]	60 ± 10 °C to 100 ± 10 °C (In-port components)	Room temperature to 240 ± 10 °C with ramps of +5 K h <sup>-1</sup> and -7 K h <sup>-1</sup> .
DEMO	Estimated 300 to 500 °C structural temperature of the blanket [30].	

### 3.2.2 Surface heat loads

Heat loads on the surface of diagnostic components from the plasma are present in the forms of fast neutral particles and non-penetrating radiation, such as infrared radiation. Table 3.3 gives the values for the first wall heat loads by radiation and neutral atoms on the first wall. The diagnostic mirrors are not subject to the same load as the first wall with its full  $2\pi$  sr solid angle to the plasma. Depending on the entrance aperture location, which can also be shadowed by other components, the duct geometry and the duct wall condition, the heat load on the mirrors is strongly mitigated.

The neutral particle flux at the first wall is also biased towards grazing incidence angles. For the ITER machine, computer simulations with the code B2-EIRENE [82]

Table 3.3: First wall radiative and particle heat loads. The values given represent upper bounds during normal operation.

Heat loads on the first wall	
JET [108]	96 kW m <sup>-2</sup> thermal radiation.
ITER [89][77]	Neutrals: 270 kW m <sup>-2</sup> Maximum average radiative load: 110 kW m <sup>-2</sup> (230 kW m <sup>-2</sup> peak)

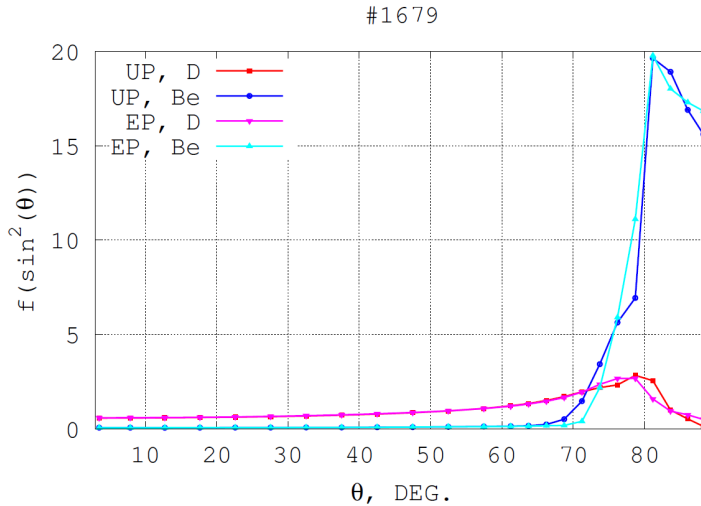


Figure 3.1: Wall incidence angular distribution for neutral D and Be in ITER at the upper (UP) and equatorial ports (EP) [47].  $\Theta=0^\circ$  at perpendicular incidence to wall.

– a Monte Carlo linear kinetic particle transport code – predict the maximum of the incidence flux distribution function at about  $\Theta = 80^\circ$  from normal incident [47]. Figure 3.1 shows the distribution over the incidence angle, where  $0^\circ$  signifies arrival perpendicular to the wall.

As for the neutral particles, the thermal radiation incidence angles are not uniformly distributed. The majority of the thermal radiation originates from regions with neutral and partially ionized atoms, which are able to emit line radiation. The main sources include the divertor region and the plasma edge. Bremsstrahlung, infrared radiation from hot components and reflection on the walls provide the more uniform background. As a result, exact calculation of the individual mirror heat load can only be done based on a specific diagnostic geometry.

### 3.3 Nuclear environment

Most fusion experiments in operation use only the two hydrogen isotopes  $^1_1\text{H}$  and  $^2_1\text{D}$ , as well as  $^4_2\text{He}$  in their experiments. While significant for plasma physics research,

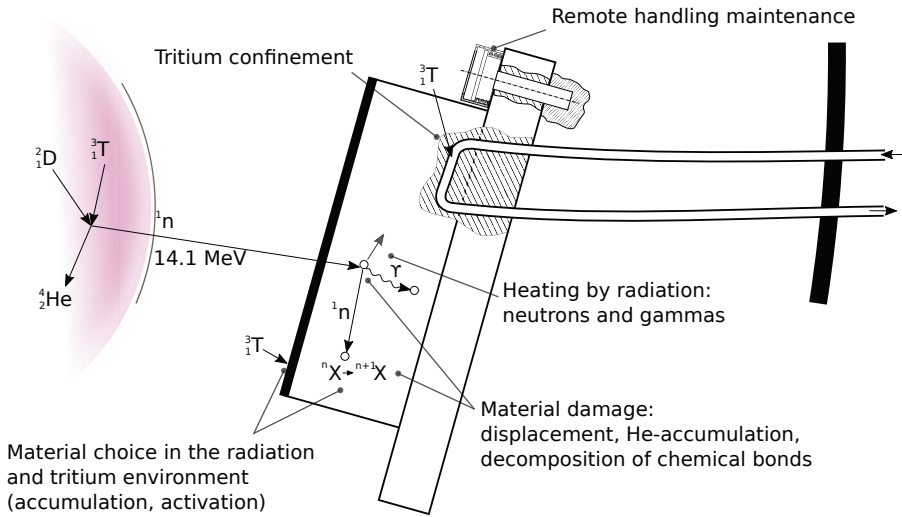


Figure 3.2: Effects of the nuclear environment on the mirror design.

the avoidance of tritium allows for a less complex design with the limited amounts of radiation from fusion reactions. The only magnetically confined fusion experiment in operation capable of handling tritium is JET. Here, tritium experiments constitute only a small part of the operational time, but tritium contamination and the slight activation requires maintenance of components inside glove boxes.

With ITER, the neutron ( $\text{n}$ ) and gamma ( $\gamma$ ) flux encountered by components is increased significantly to JET with an about 30-fold increase in fusion power and an orders of magnitude longer 50:50 mixture D-T operation time (see Table 2.1). In this environment, all components have to be designed for the nuclear environment to a much greater degree than in any previous fusion experiment.

Figure 3.2 gives an overview on the effects of the radiation environment. A detailed discussion is given in this section, split into restrictions for material choice, design considerations and the volumetric thermal effects.

While a number of consequences of the nuclear environment are equal throughout the system (e.g. contamination with tritium), others change based on location. These include local radiation flux, material damage and thermal effect for the diagnostic components. Calculation of the radiation fields taking into account the local and global geometry is possible with specialised codes; in this work, results from calculations using the Monte Carlo N-Particle (MCNP) code [56] are used. Calculations with the source term and geometry of ITER core CXRS reference layout give a fast neutron fluence ( $n_e \geq 0.1 \text{ MeV}$ ) for port-mounted first mirrors of about  $1 \times 10^{20} \text{ n/m}^2$  [16]. The values also exhibit a gradient of about four orders of magnitude within the first metre of shielding. The radiation field imposes requirements on general design, materials, use and maintenance to all components exposed to the field.

In case of ITER, the legal nuclear requirements on in-vessel components are limited

as these components are not seen to constitute a nuclear confinement barrier by the regulatory body. The first legal barrier is the vacuum vessel with the feed-throughs and in-air pipes up to the isolation valves. The internal components may not negatively influence the integrity of the regulatory confinement barrier in all design load situations.

### 3.3.1 Limitations on material choice

The presence of hard neutron radiation from the fusion reactions and gamma radiation from interactions of the neutrons with materials and tritium in the plasma results in restrictions on the choice of materials for ITER and DEMO. Activation of material from neutron capture should be minimised to reduce problems associated with handling during maintenance and waste disposal after shutdown.

Adsorption and, thus, accumulation of the tritium has to be limited by choosing materials with low chemical affinity for hydrogen. In addition, diffusion of tritium into cooling fluids needs to be minimised through use of materials that show a low rate of hydrogen diffusion or by using higher wall thickness for components in the design.

The combination of a radiation environment with the vacuum requirements leads to additional restrictions on material choices. Many materials show increased desorption under the influence of radiation, preventing their use in a fusion environment. Materials with covalent bonds can also decompose under the influence of radiation with outgassing rates exceeding the vacuum limits. The vacuum compatibility of materials under the influence of radiation has to be determined prior to their use.

At the anticipated locations of the mirrors in ITER and DEMO, changes in metallic materials due to transmutation and displacement of atoms are not a problem for the mirrors. Simulation of ITER predicts up to a maximum of 0.5 dpa (displacements per atom) during the operational lifetime at the feasible locations of diagnostic mirrors [16]. At this value, embrittlement, swelling and change in material properties are not significant with regard to the mechanical functions of components.

The radiation field is also sufficiently small not to degrade the optical properties of metallic mirrors. A collection of studies on the subject is given in [22].

Other optical coatings – e.g. multilayer dielectric coatings – are affected by the radiation: A material- and dose-dependent shift in reflectivity is reported but no deterioration of the reflectivity or damage to the mirror coating due to the radiation itself [92][74].

### 3.3.2 Volumetric heat loads by radiation

The fast neutrons from the plasma, and the  $\gamma$ -radiation from the interaction of the neutrons with the material of the machine, represent a volumetric source of heat for all components. The amount of heat deposited per volume depends on both the material of the component (interaction cross section) and the local radiation field.

Figure 3.3 shows the photon heating in a slice of the ITER core CXRS UPP layout of 2009 [16]. The structure mostly consists of the stainless steel 316L(N) in a special high-purity ITER grade (316L(N)-IG [7]) with a varying fraction of water for neutron

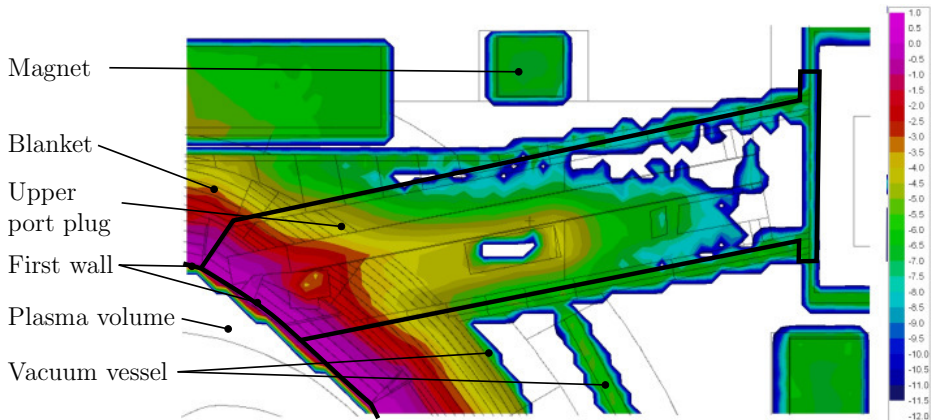


Figure 3.3:  $\gamma$  heating in the ITER CXRS-core UPP ( $\log[\text{W cm}^{-3}]$ ) [16] with structure outlines overlaid.

moderation and cooling. The heat distribution is visibly influenced by differences in material and streaming effects through gaps. The heating by neutrons contributes an additional 5% in the front first meter and matches the gamma heating after that. The non-linearity is due to changes in material composition and differences in the neutron and gamma spectrum along the port plug, highlighting the need for accurate calculations of the actual geometry during design.

A significant thermal impact of the radiation in ITER is only present close to the plasma. If a threshold of significance is assumed at  $1 \times 10^{-3} \text{ W cm}^{-3}$  for 316L(N)-IG, which results in an increase in temperature of about  $1 \text{ K h}^{-1}$  for a thermally isolated component, neutron and gamma heating may be neglected after about 1 m into the UPP of ITER core CXRS.

Heating up from decay heat after activation is encountered in ITER. For an older ITER scenario with 1.5 MW fusion power, the decay heat for materials activating similarly to 316L(N)-IG is predicted as  $0.01 \text{ W cm}^{-3}$  at the location of the mirrors (30 cm behind the wall) directly after shutdown [8]. One day later, the heat is already reduced by one order of magnitude. With the reduced fusion power and duty factor of the current ITER design, the decay heat is not significant for the mirrors, other than for strongly activating materials with short half-lives. Depending on the diagnostic location, decay heat may be a significant factor in DEMO.

### 3.3.3 Design for the nuclear environment

The exposure of components to the tritium inside the vacuum vessel and the activation of components by neutron irradiation necessitate maintenance inside a hot cell. All components foreseen for maintenance need to be designed with the requirements and limitations of the hot cell, where interaction is only possible by remote handling (RH). The operational experience of hot cells for fusion experiments and the associated maintenance procedures has been collected in JET and is available for the design of ITER [25] [68].

Helium production from neutron capture leads to problems with re-welding after irradiation depending on the material. For stainless steel 316, crack appearance in welds has been observed starting at 0.7 appm He-content [103]. No vacuum boundary requiring re-welding may be located in regions where the material-dependant critical levels of He production is exceeded before the last anticipated maintenance time slot. In case of ITER, helium production up to about 0.5 m of shielding is predicted to reach the critical limit for stainless steel 316L(N)-IG.

### 3.4 Electromagnetic environment

The tokamak and stellarator designs of fusion reactors rely on magnetic fields to confine and control the plasma. At the UPP in ITER, the operational magnetic field reaches a peak magnetic flux density of 5 T.

Plasma confinement is reduced in the presence of error fields as introduced by components with diamagnetic or paramagnetic properties. For ITER, the material choice within the cryostat boundary is restricted to materials with relative permeability of  $\mu/\mu_0 < 1.03$  [19]. The magnetic permeability also has to be considered in the manufacturing process, as it can be influenced by manufacturing operations. For example, welding of the steel 316L(N) can increase permeability significantly [50]. Heat treatment may be used to normalize magnetic properties.

In addition to the static magnetic field, fast transients are encountered in tokamaks during disruptions (loss of the confined plasma). In a disruption, the plasma touches the wall and cools within 1 ms (thermal quench). As a result of the increasing electric resistance of the plasma, the plasma current decays (current quench).

In ITER, the current quench is expected to last about 16 to 50 ms. Figure 3.4 shows the magnetic field (B) as encountered during a vertical displacement event (VDE) with a 36 ms) current decay time at the ITER core CXRS first mirror of the ‘Large M1’ optical layout in the diagnostic upper port.

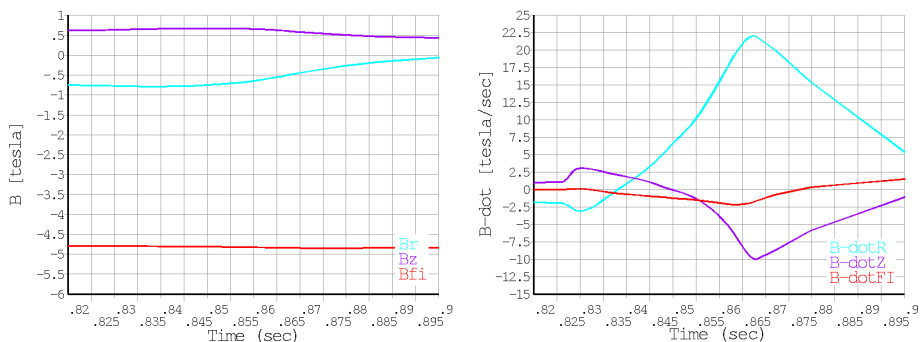


Figure 3.4: Magnetic field and derivative during a VDE at the core CXRS first mirror [76]. r: radial, z: vertical, fi ( $\phi$ ): toroidal.

The changing magnetic field gives rise to an electric field, as described by the

Maxwell-Faraday equation, with  $\vec{B}$  as the magnetic field and  $\vec{E}$  as the electric field.

$$-\dot{\vec{B}} = \nabla \times \vec{E} \quad (3.4.1)$$

Expressed in integral form, the equation integrates the electric field on a contour  $S$  and over the contour enclosed area  $A(t)$  on the magnetic field.

$$\oint_S \vec{E} ds = - \iint_{A(t)} \frac{\partial \vec{B}}{\partial t} d\vec{A} \quad (3.4.2)$$

Assuming that the feedback of the electric field to the magnetic field is small, the body is resting and the magnetic field derivative  $\dot{\vec{B}}$  is independent of location, the induced voltage  $\vec{U}_{ind}$  and current  $\vec{I}_{ind}$  in a stationary closed loop is given as

$$\vec{U}_{ind} = R\vec{I}_{ind} = -\frac{d\vec{B}}{dt} \iint_A d\vec{A} \quad (3.4.3)$$

Further, a cylindrical volume of electric resistivity of  $\varrho$ , radius  $r$ , thickness  $z$  and with the flat surface perpendicular to the z-direction is assumed (see Figure 3.5). For a magnetic field with  $\frac{d\vec{B}}{dt} = \dot{B}_z$ , the induced current  $dI_{ind}$  in an infinitesimal loop at the radius  $nr$  ( $n = 0$  in the centre and 1 at the outside edge) and radial thickness of  $nr dn$  is given as

$$dI_{ind} = -\frac{\dot{B}_z z r^2 n}{2\varrho} dn \quad (3.4.4)$$

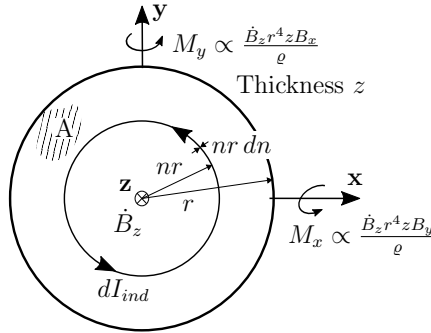


Figure 3.5: Moments acting on components in a changing magnetic field through the Lorentz force by the induced eddy currents.

The current interacts with the remaining magnetic field and a Lorentz force  $d\vec{F}$  arises. With the given assumptions and geometry the forces balance in the body but a moment  $d\vec{M}$  remains with

$$d\vec{M} = \vec{L} \times d\vec{F} = \vec{L} \times (dI_{ind} \vec{l} \times \vec{B}) \quad (3.4.5)$$

$$\vec{L} = \begin{pmatrix} n r \cos(\phi) \\ n r \sin(\phi) \\ 0 \end{pmatrix} \quad (3.4.6)$$

$$\vec{l} = \frac{d\vec{L}}{d\phi} \quad (3.4.7)$$

with  $\vec{L}$  being the lever arm of the Lorentz force and  $\vec{l}$  the circular path of the current loop. Integrating over  $\phi = 0..2\pi$  and  $n = 0..1$ , the resulting moment on the volume is calculated as

$$\vec{M} = \frac{\pi \dot{B}_z z r^4}{8 \varrho} \begin{pmatrix} B_y \\ B_x \\ 0 \end{pmatrix} \quad (3.4.8)$$

For a more complex geometry with changing magnetic field over location and feedback of the electric to magnetic field, the calculation is more complex but the base dependencies on geometry and material properties are retained. The force and moment on bodies by eddy currents can accordingly be reduced by the following design choices:

- Use of materials with higher electrical resistivity, reducing the current in the part
- Adopting the part geometry for smaller eddy current loops: Use an orientation to  $\dot{B}$  where only smaller areas lie perpendicular to the change in the magnetic field and introduce gaps to break up large connected volumes
- Isolate parts to prevent current loops through multiple parts in assemblies

As an example for the forces, exact calculations using the transient given in 3.4 for the core CXRS first mirror made from molybdenum (size of about 130 \* 280 mm<sup>2</sup>) results in peak moments of 1.48 kN m ( $M_{rad}$ ), 0.79 kN m ( $M_{fi}$ ) and 0.11 kN m ( $M_z$ ).

In addition to the generation of forces, eddy currents may lead to arcing. This can, e.g. damage the mirror surface and point contacts that may be used in mirror alignment mechanisms. The creation of electric potentials needs to be checked and geometries prone to arcing should be avoided.

## 3.5 Fluid ingestion events

In case the vacuum barrier is damaged, diagnostic components are exposed to the leaking fluid. As maintenance possibilities are limited and time consuming, the diagnostic components should survive exposure to the fluid even at operational and bake-out temperatures.

In the case of the water-cooled ITER, 15+ ingress of coolant events of varying magnitude are anticipated, exposing components inside the vacuum vessel to steam with pressures up to 0.2 MPa [85]. In addition, the need for venting with dry air and nitrogen at operational temperatures, lasting 2 to 10 hours, is foreseen [21]. For both cases, the diagnostic equipment should be left in a workable state.

### 3.6 Mirror surface contamination

Contamination of the mirror surface leads to reduced specular reflectivity, degrading diagnostic performance. If possible, the mirror design should minimise the build-up of contamination to preserve system performance. Inside the primary torus vacuum, three types of deposit are found:

- Dust may relocate and settle on the mirror surface due to disturbances – e.g. disruptions and gas-assisted migration while the vacuum is absent. Dust migration has to be addressed on the system design level: shutters, gas flows. The methods do not impose design requirements on the mirrors
- Deposition of metallic and ceramic layers due to sputtering by the plasma. Transport of the material and mitigation techniques, especially for the first mirror, are widely researched [47] [100] [70] [53]. Cleaning methods, including ablation by laser and local sputtering with plasma, are proposed. The cleaning methods require very specific provisions for the mirror to be cleaned – e.g. allowing an electric bias of the mirror surface or the use of sputter- or laser-resistant material, but no method is yet shown to work under ITER conditions. Consequently, the limitations on mirror design imposed by the cleaning systems are not included in this work
- Molecular contamination from adsorption or condensation of materials on the mirror surface (explanation below)

Molecular contamination has been studied extensively for space applications and is taken into account in the design of space equipment [97]. In a fusion reactor, the most critical time for significant condensation of materials is during the vacuum bake-out temperature ramp-up when contamination in the machine is evaporating. The amount of contamination in a fusion reactor is limited by the strict requirements on cleanliness to achieve the vacuum level and residual gas composition necessary for fusion. But the presence of contamination cannot be completely ruled out initially and after maintenance. For example, condensation to the point of dripping from internal structures has been observed in TEXTOR (private communication, O. Neubauer, 2012, Ph. Mertens 2014). While the majority of the condensate should re-evaporate once the maximum bake-out temperature is reached with equal temperature on all surfaces, chemical reactions and relocation of dust after significant condensation of, e.g. water from a water ingress event, may leave a mirror permanently degraded.

The residence time of molecular contaminants strongly depends on the temperature  $T$  of the surface and can be described as

$$\tau(T) = \tau_0 \exp^{E_a/RT} \quad (3.6.1)$$

where  $E_a$  is the binding energy of the molecule and  $\tau_0$  the molecule's oscillation period on the surface [97]. Consequently, accumulation of condensate can be mitigated by maintaining the mirror surface at least at or above the temperature of the environment where the contaminant evaporated. As the severity of the impact cannot be quantified based on the limited knowledge about the actual amount and the composition of contaminants inside future machines, and the possibility for maintenance is

limited, the ability to reach a mirror temperature during vacuum bake out above the environment is considered in the design.

### 3.7 System lifetime and maintenance

The target lifetime of fusion diagnostic components located inside the torus is the same as the machine lifetime or the time until the diagnostic system is no longer required because of the inherent complexity with all maintenance operations. As an example from DEMO, some diagnostic systems might be operational for initial operation only until the plasma behaviour is fully understood. While maintenance of diagnostic systems is possible, it is restricted to the hot cell facility with remote handling only after the first D-T operation due to the activation and contamination with tritium.

For ITER, the nominal diagnostic system lifetime is specified as 20 years, identical with the machine. Refurbishment of diagnostic systems is possible during the eight-month machine shutdown about once every two years, but the capacity of the hot cell facility is severely limited. Of the 15 diagnostic upper port plugs, only two can be refurbished per shutdown [10]. To minimise the amount of radioactive waste, replacement of damaged mirrors, rather than larger structures, is set as the maintenance goal of ITER.

# Chapter 4

## Mirror design state of the art

In this chapter, the state of the art for mirror design is explored, taking into account the fusion environmental conditions, as discussed in the previous chapter. The state of the art is taken from existing and proposed mirror designs aimed at conditions that are either comparable to a large sub-set of fusion conditions or even exceed the loads as predicted for ITER and DEMO. The fields included in the discussion are:

- Designs proposed for ITER
- Current-generation fusion diagnostic systems as they feature a large subset of the next-generation machine requirements
- Space applications for their maintenance-free design, forces during launch and vacuum environment
- High-energy laser systems for their thermal design

The general mechanical design, mirror adjustment, thermal design and mirror surface treatment are looked into in detail.

### 4.1 Mirror mechanical design

The two main goals of the mirror mechanical design are to position the mirror surface precisely and to prevent deformation and damage of the mirror surface by internal and external effects. In the long history of optics, numerous mirror designs achieving these goals within their intended use have been devised. Here, selected concepts are introduced and their applicability for ITER and DEMO for the topics of substrate, mounting, adjustment and fluid cooling is discussed briefly. The discussion assumes mirror sizes up to  $\varnothing 400$  mm.

**Substrate and mirror mount:** Mounting of the substrate includes retaining the substrate against external forces and mediating differences between environment and substrate, e.g. differential thermal expansion. This functionality can either be fulfilled by dedicated components or may be built into the substrate.

For small laboratory-grade equipment, irrespective of substrate material, mounting is often achieved with simple clamps in various combinations (see Figure 4.1 for an

example). The ease of replacement with this kind of mounting is not necessary in a reactor and the limited position stability precludes the use in a fusion reactor for non-flat mirrors or mirrors larger than a few mm.

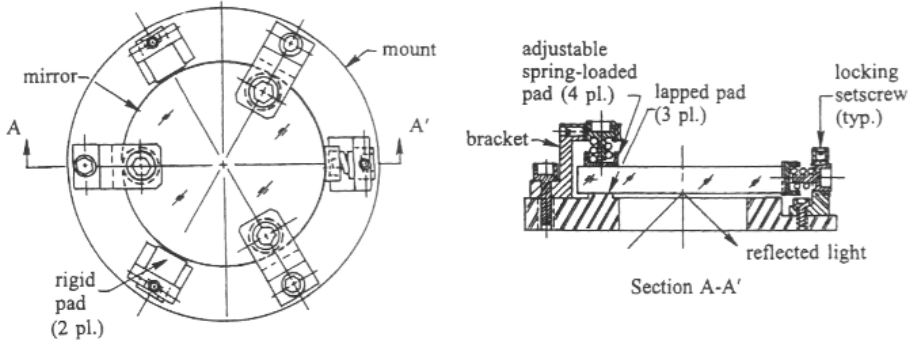


Figure 4.1: Example of a sophisticated spring-loaded clamped small mirror mount. (From [75])

More sophisticated clamped mounts are also used for larger metal and ceramic mirrors. Figure 4.2 shows a proposed design for the divertor Thomson scattering diagnostic system in ITER [70][71]. The design uses a polycrystalline silicon (PCS) mirror substrate with a silicon carbide (SiC) peg. The peg is clamped with pre-load in a stainless steel frame which in turn is bolted to the support structure of the diagnostic system. With the pre-load by spring elements, sufficient give to accommodate significant differences in thermal expansion can be designed into the mount. While the design of Figure 4.2 was found to be suitable for the SiC peg clamped in stainless steel, the combination of the SiC peg and Si mirror causes unacceptable deformation [71].

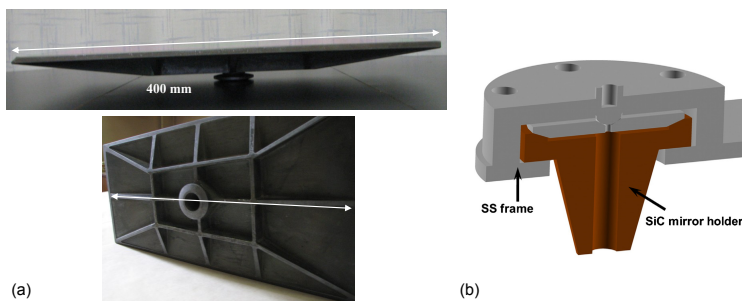


Figure 4.2: Mirror design with polycrystalline silicon substrate for the divertor Thomson scattering diagnostic system. Images adapted from (a) [70], (b) [71].

Direct bolting of the mirror substrate is often used for metallic substrates but also for brittle substrates with appropriate cushioning. With careful design, forces from the mounting can be decoupled from the optically important section of the mirror

substrate. One basic example with tabs machined directly from the metal substrate is shown in Figure 4.3. A second example is shown in Figure 4.5 for a fused silica cryogenic mirror mounted to a titanium plate where the flexures also compensate for the significant differential thermal expansion. The use of a thermoplastic as cushion for the substrate, as included in this design, is not possible within a fusion reactor.

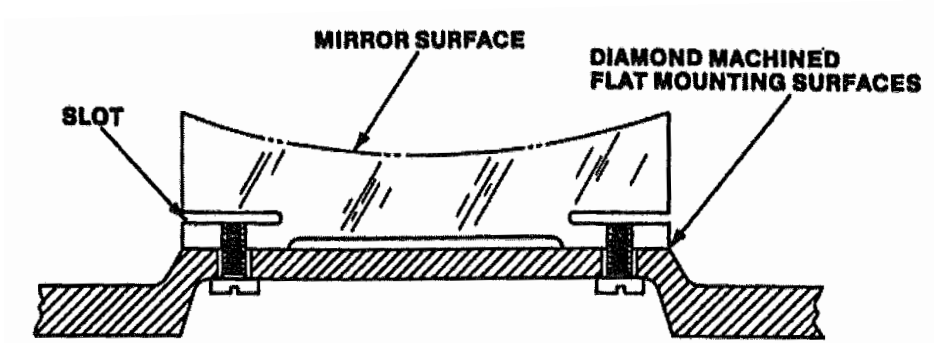


Figure 4.3: Metallic substrate with flexures machined from the substrate material for strain-free mounting ([111] from [75]).

A second option for preventing forces from reaching the mirror surface are flexible, shaped connections between two stiff sections (one used in the mounting and one to carry the mirror surface), as discussed in, e.g. [2].

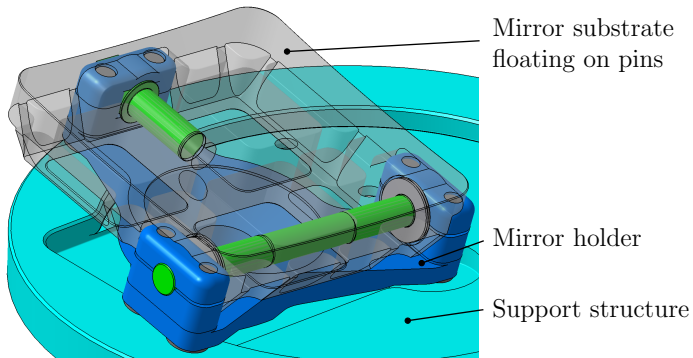


Figure 4.4: Design of the JET KL-11 endoscope second mirror: Aluminium floating substrate with aluminium holder and structure.

In addition to flexure elements, mirror mounts with a floating substrate are used to compensate differential expansion. A realization of this approach is shown in Figure 4.4. The design is used for the second mirror in the JET KL 11 endoscope [37]. The substrate, subject to external heating, is made of aluminium and is mounted to an aluminium support structure. The substrate can expand on the two pins (green) while being held free of play by disc springs.

High accuracy positioning of the mirror substrate can be achieved by precision machining of dedicated geometry. Often, the specialised machining operations used for the optical surface can also be used for the positioning geometry in case the component is designed in this regard. A common example is single-point diamond turning which, in the best case, enables machining of positioning elements in the same chucking as finalising the mirror surface.

**Mirror adjustment:** With the multi-mirror chains necessary for fusion diagnostic systems, assembly time adjustment of mirrors that later reside in vacuum is necessary. These adjustments may be realised as a separate interface or can be combined with the substrate mounting. For use in a fusion reactor, the main requirement for the adjustment mechanism is the stability of the mirror surface position during the reactor lifetime.

In current fusion diagnostic systems, shims are the common adjustment mechanism for in-vacuum mirrors in the limited number of cases where adjustment of in-vacuum mirrors is required. For example, the KL 11 endoscope shown in Figure 4.4 uses shims on the three bolts that clamp the mirror holder to the structure on the rear [37]. The mirror is not designed for re-adjustment in a hot cell.

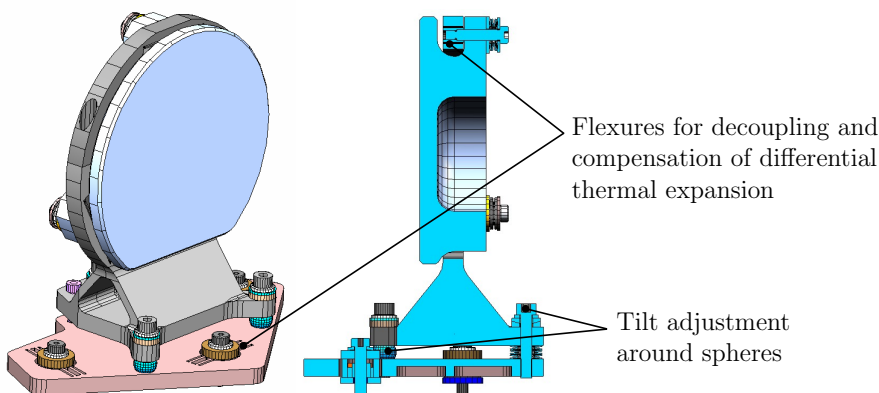


Figure 4.5: Shortwave Fold Flat Mirror Assembly of the James Webb Space Telescope NIRCam instrument [29].

In laboratory systems and for limited-size mirrors, kinematic mounts or quasi-kinematic variations are common: Pre-loaded point and small area contacts in a configuration minimising forces generated by the mounting, allowing differential thermal expansion and adjustment.

Figure 4.5 shows the alignment mechanism with one rotation for a space telescope mirror with two spheres and an adjustment screw as stands in a spring-preloaded, quasi-kinematic configuration.

**Design for remote handling:** For ITER, the exchange of single mirrors during maintenance in the hot cells is desired to minimise radioactive waste. As this is not a

common requirement for mirrors, designs aimed at remote handling maintenance are very limited. Of the existing fusion experiments, only diagnostic systems in JET have to take remote handling into account and it is mostly restricted to the positioning of assemblies in the torus. Outside, glove boxes are used in the maintenance operations.

For ITER, generic designs and guidelines are given to be used in all standard remote handling operations, including the cutting and welding of pipes, bolting of components and inspection [93]. Care must be taken that the whole system is designed for remote handling, including the surroundings of the component destined for maintenance. To enable maintenance by remote handling, access for tools, sufficient light and cameras for visual feedback are required. Standard parts shall be used whenever available.

Some designs and approaches for the installation of diagnostics in JET during the year 2010/11 upgrade are given in [3]. For the positioning of diagnostic assemblies in the torus, welded rails were used allowing the positioning and attaching of assemblies (see Figure 4.6).

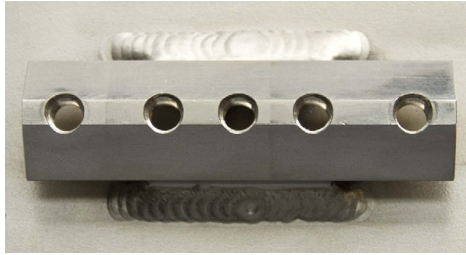


Figure 4.6: Rail welded to the JET vacuum vessel for remote handling positioning and mounting of diagnostic assemblies [3].

Figure 4.7 shows the positioning principles proposed by ITER to avoid wedging and jamming during the installation of components. The achievable positioning accuracy and stability has to be carefully checked for the used case of mirrors. The standard design of the dowel arrangement in 4.7(b) specifies a fit at the pins of  $\varnothing d_{10}^{D10}$ , thus allowing for a play of 80 to 196  $\mu\text{m}$  with a  $\varnothing 10$  mm pin. The Electron Cyclotron Resonance Heating system in ITER plans to use a concept with three pins for positioning of the microwave quasi-optical first mirror [44].

**Substrate thermal control:** Mirror substrates are in thermal contact with the environment by at least heat conduction at the substrate mounting interface and by radiation. In current fusion devices, all mirrors are heated and cooled via these two paths. This approach is possible due to the protected mirror location as well as the limited shot time and fusion power.

With ITER and DEMO, heat loads are increased and more direct cooling methods might be required to combat overheating of the material or exceeding of tolerances from deformation by thermal gradients. The cooling of extreme surface heat loads is encountered in high-energy layer systems with heat fluxes in the  $\text{kW m}^{-2}$  range. Figure 4.8 shows designs for fluid channels in laser mirrors, from basic layouts with

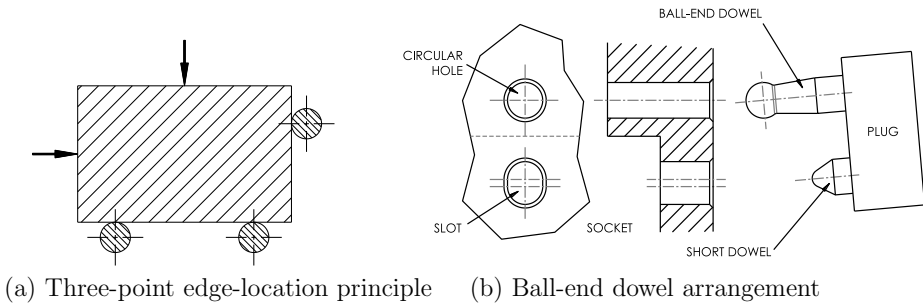


Figure 4.7: Positioning principles suggested by ITER for remote handling operations [93].

drilled holes to sophisticated structures with high surface areas and minimised shape aberrations of the mirror surface [5].

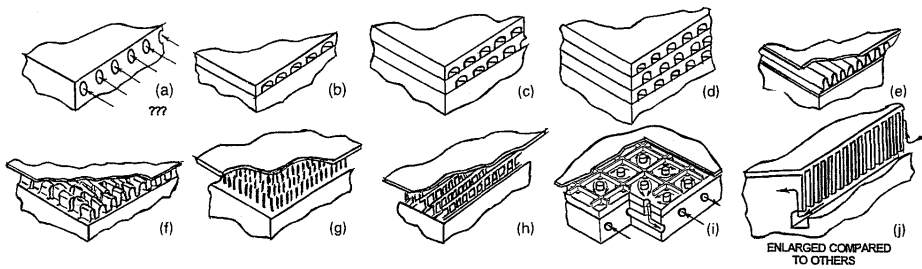


Figure 4.8: Heat exchanger concepts for mirrors in high-energy laser systems [5].

Heat pipes represent a second possibility with high heat transfer capacity over extended distances [95]. In fusion, these are interesting as no vacuum feed-through or welded connection is required. A heat pipe uses a recirculating material undergoing a state change: The material evaporates at the hot end and condenses on the cooled section. It is then returned by gravity or capillary forces to the hot end (see Figure 4.9). A temperature gradient is necessary for the heat pipe to start up. Bi-directional heat transfer for both heating and cooling is possible. Depending on the working material, different temperature ranges can be addressed, including the relevant temperatures for fusion diagnostic systems.

For all high-heat flux thermal management, care must be taken during operation so that surface deviations caused by local cooling or heating do not produce surface ripples, thereby leaving the mirror to exceed the optical tolerances.

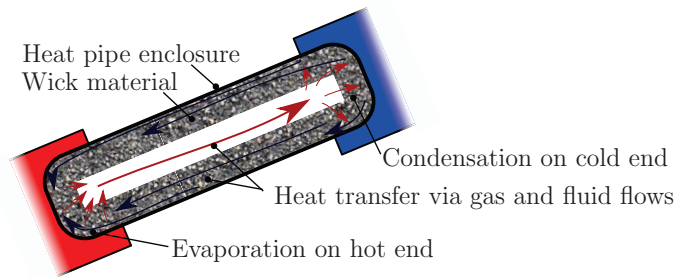


Figure 4.9: Principle of a heat pipe with wick.

## 4.2 Mirror surface treatment

The choice of mirror surface is governed by the need of the individual diagnostic system, based on reflectivity requirement, wavelength and environmental conditions. In the following, the available mirror surface treatment options with the level of knowledge about their application in fusion are introduced.

**Uncoated bulk metal mirrors:** The substrate is polished to optical quality and directly used as mirror surface. In the scope of this work, designs with a thick layer welded or brazed to the substrate are also included in this group as they show identical optical properties. The maximum reflectance of the mirrors is limited to the reflectivity of the substrate.

Bulk metal mirrors can be damaged by blister formation from the impact of fast particles [96] (polycrystalline molybdenum), but neutron and gamma radiation up to a fluence, as encountered in ITER, have been found to not pose a problem (overview in [22]). Depending on the material, chemical reactions may impact optical properties – e.g. oxidation during a water ingress event. Bulk metal mirrors, especially single crystalline substrates, have been found to be most resilient against loss of reflectivity under sputtering conditions and are investigated for the first mirror in direct view of the plasma [54][100][55]. Candidate materials include stainless steel, copper, molybdenum, tungsten and rhodium.

**Metallic coatings:** Coating with metals combine higher reflective materials of beneficial properties with a choice of substrate. Common metallic coatings are aluminium, gold, silver and rhodium. Where a substrate with limited ability for polishing or insufficient adhesion for the coating should be used, inter-layers between substrate and coating can be introduced with the required properties. Failure modes of the coating include cracking, blister formation and flaking.

For fusion applications, especially coatings with Rh are investigated for visible wavelength-range optical systems. Coating of Rh on stainless steel has successfully been used in JET [20]. The use of Rh coatings has also been tested for ITER conditions [61] [41]. As with the bulk metal mirrors, the radiation field of ITER has been found to be non-critical for the optical properties.

**Metallic mirrors with protective layers:** Depending on material and particle load, the use of a transparent protective layer – e.g.  $\text{ZrO}_2$  – to prevent oxidation and damage of the mirror surface due to sputtering by fast particles has been proposed for use in ITER [79]. For the oxide coating on the metal, the adhesion of the coating is critical. Failure of the coating not only removes the local protection for the metallic base but also increases diffuse reflection from the exposed edges of the remaining protective layer.

Build-up of partially reflective material deposits on top of the protective coating can lead to destructive interference, strongly reducing reflectivity for certain wavelengths, depending on the thickness of the protective coating layer [78]. Thus, the use of a protective layer is only seen as viable far into the optical duct where the build-up of deposits is not a problem. The migration distance of deposits depends on the duct geometry and environment, and has to be checked for the individual diagnostic system.

**Multilayer dielectric coatings:** A constructive interference is created on the mirror side of the coating by stacking  $\lambda/4$ -thick layers of alternating high (H) and low (L) index of refraction materials (see Figure 4.10). Specular reflectance in excess of 99 % can be achieved by dielectric coatings within a limited design bandwidth. Common layer materials of interest in fusion include  $\text{HfO}_2$ ,  $\text{Nb}_2\text{O}_5$ ,  $\text{TiO}_2$ ,  $\text{ZrO}_2$  and  $\text{SiO}_2$ .

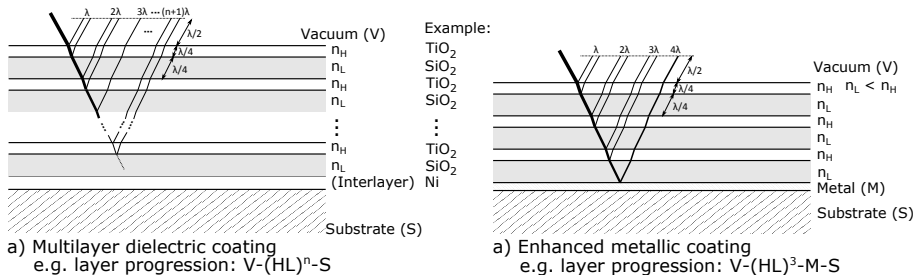


Figure 4.10: Structure of (a) multilayer dielectric coatings and (b) enhanced metallic mirrors. H: high index of refraction; L: Low index of refraction.

The width of the reflectance bands can be increased by stacking packets with different target wavelengths or varying the thickness between layer pairs. Stresses in the coating cannot be avoided and are generated already during deposition – e.g. due to lattice mismatch – but also depend on temperature since the thermal expansion between the coating layers differ. For application in fusion, the occurrence of destructive interference from partially transparent contamination deposits has to be taken into account, as described above for the metal mirrors with protective layer.

The reflectivity of multilayer dielectric coatings depends on:

- Angle of incidence (travel distance of the light through the layers)
- Polarization direction of the light

- Temperature of the coating (thermal expansion of the materials and substrate changing mechanical and optical thickness)
- Other changes of the coating – e.g. crystallization of a layer; different morphology by radiation

The dependencies cannot be avoided and lead to shifts of the reflectance curve up to collapse of the constructive interference. Testing under conditions approaching fusion reactor environments has shown that coating suitability differs between materials but also manufacturers [72] [73][92]. In these tests, elevated temperatures, as encountered in ITER with 240 °C during vacuum bake-out, were found to be among the critical loads.

Damages found under fusion conditions include permanent changes in reflectivity from elevated temperature. These can be caused by micro-structural changes in the coating. Especially for the  $\text{TiO}_2/\text{SiO}_2$  system, a strong effect of the temperature on the coating reflectivity has been observed above 200 °C for a commercial coating [72]. The proposed cause for this behaviour is crystallization of the amorphous  $\text{TiO}_2$ . Blister formation up to full failure of the coating has also been observed; see Figure 4.11 for examples with  $\text{TiO}_2/\text{SiO}_2$  (left) and  $\text{ZrO}_2/\text{SiO}_2$  (right) dielectric coatings on silica glass (KS-4V) substrate manufactured by the manufacturer “LOGF”, Lytkarino, Russia, after one excursion to 250 °C[74].

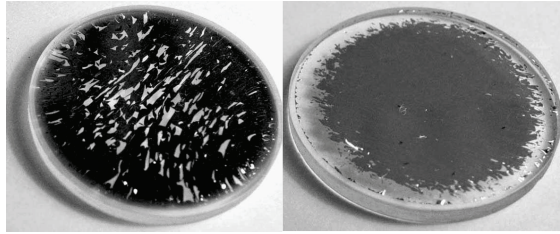


Figure 4.11: Damaged dielectric coating after heating to 250 °C [74].

Testing with neutron damage is available for a number of materials in the ITER-relevant range:  $\text{SiO}_2/\text{TiO}_2$  and  $\text{Nb}_2\text{O}_5/\text{SiO}_2$  with fast neutron flux ( $E > 0.1 \text{ MeV}$ ) up to  $2 \times 10^{17} \text{ cm}^{-2}$  with no change in the reflectance [72];  $\text{HfO}_2/\text{SiO}_2$ ,  $\text{Al}_2\text{O}_3/\text{SiO}_2$  and  $\text{HfO}_2/\text{Al}_2\text{O}_3$  for damage up to 0.1 dpa (displacements per atom) with the result of a material, annealing temperature, and irradiation dose-dependent shift in working wavelength range up to 20 nm [92][51]. The given dielectric coatings show high stability for the optical properties under irradiation up to 0.1 dpa, sufficient for use in ITER.

In two areas, test results are very limited for use of the mirrors in ITER: long-term coating stability under thermal conditions, where a single vacuum bake-out cycle at 240 °C may last up to four weeks, and coatings on substrates other than glass, which is not an easy choice as substrate material for use in ITER.

**Enhanced metallic mirrors:** A metallic reflective surface is enhanced at specific wavelengths with a limited number of dielectric layers on top (see Figure 4.10 (b)).

With increasing reflectivity requirement, the presence of the metallic surface has a diminishing effect. Enhanced metallic mirrors are subject to all failure modes of the protected metal mirrors and include the increased layer stress of the multilayer coatings. Where no extra-wide wavelength mirror with selective high reflectance bands is required, this type of mirror is not deemed beneficial in a fusion diagnostic system, as the decrease in price to a pure dielectric coating from the lower number of layers is not significant with the limited overall number of mirrors.

### 4.3 Conclusion on environmental conditions and state of the art

The individual general fusion reactor environmental conditions for diagnostic mirrors allow the use of existing mirror designs. Solutions for mirrors that are subject to a subset of the ITER and fusion reactor environment are available in current fusion experiments and outside the fusion field. For a number of loads, the requirements found in a fusion reactor are even exceeded, including for example surface heat load in high energy laser systems.

The challenge for the design of mirrors in a fusion reactor stems from the combination of boundary conditions. No existing system is subject to the same combination or a superset of the requirements as found in a fusion reactor with D-T plasma operation time of half a year and more. With the combination of environmental conditions, interactions arise where the resulting environment is more restricting than the sum of the individual components. One example are a number of covalent bound materials which have to be excluded if both high-energetic radiation and vacuum are present because of radiation induced out-gassing.

Taking into account the interactions of environmental conditions, the existing solutions for individual functional groups of mirror designs were reviewed for their applicability in fusion. It was found that especially the presence of tritium and the activation by neutrons, requiring the use of remote handling for any maintenance, are not well covered by existing designs. The discussed solutions are taken into account in the further design considerations and modified where necessary to account for the changed requirements of the fusion reactor environment.

# Chapter 5

## Principal considerations on mirror design in fusion reactors

As discussed in Chapter 4, individual systems with partially stricter requirements exist outside of fusion, but the specific combination of environmental conditions as found close to the fusion plasma requires an adapted design. In this chapter, solutions for singular functionality and fundamental design choices are discussed for the target requirements of ITER and DEMO. The topics of mirror substrate selection, mirror adjustment during assembly and in the hot cells, substrate temperature control and the overall maintenance approach are looked at in detail.

For this chapter, it is assumed that the support structure in between mirrors is made from stainless steel. While other materials can be used, the implications of different support structure materials are very diverse. With numerous effects also on the diagnostic system level design, a complete discussion is not feasible in the scope of this work. Stainless steel is used as a versatile general purpose material and represents the baseline for all structural components in ITER and DEMO. In addition, it is assumed that the diagnostic mirrors' design wavelength is located in the visible wavelength range in order to focus the discussion, but without limiting the general case.

### 5.1 Mirror substrate material selection

The choice of mirror substrate material is central to the design and operation of the mirror. In the fusion environment, two material groups are suitable given the restrictions inside the vacuum vessel: ceramics (including glass ceramics) and metallic substrates. A number of requirements, some partially contradictory, have to be weighed against each other:

- Thermomechanical stability: Substrate deformation is reduced for materials with high thermal conductivity ( $\lambda$ ) and low coefficient of thermal expansion ( $\alpha$ ). In general, volumetric heating by n- and  $\gamma$ -radiation tends to scale with density of a material ( $\rho$ ), but is also strongly governed by interaction cross section and the possible reactions.

- Mechanical stability: High rigidity (Young's modulus,  $E$ ) minimizes deformation due to external forces. Higher electric resistivity ( $\rho$ ) is preferable during magnetic transients. The dead weight of the individual mirror, governed in large parts by the density, is of secondary concern in a fusion reactor
- Material suitability: Coating adhesion for coated mirrors or sufficiently high base material reflectivity. Vacuum and radiation suitability as was discussed in Chapter 3
- Manufacturing and assembly suitability: Availability of manufacturing methods and procedures; complexity of the mirror design for manufacturing and assembly

For thermomechanical stability,  $\alpha/\lambda$  is an often-used figure of merit in optics to compare materials. For example, on a mirror with surface heating and cooling on the rear side, a conduction-driven temperature gradient arises and deforms the mirror substrate. For a plate of thickness  $z_c$ , the temperature difference between front and rear is given as

$$\Delta T = T_0 - T_z = \frac{\dot{q}z_c}{\lambda} \quad (5.1.1)$$

where  $\dot{q}$  is the heat flow. For an unconstrained finite plate with edge length  $l_0$ , the difference in expansion on the front and rear sides  $\Delta l$  is proportional to the change in mirror surface curvature and is calculated as

$$\Delta l = \alpha_m \Delta T = \frac{\alpha_m}{\lambda} \dot{q}z_c \quad (5.1.2)$$

with  $\alpha_m$  being the mean instantaneous coefficient of thermal expansion for the temperature range. Thus, the use of  $\alpha/\lambda$  allows comparison of different materials with regard to stability under surface heat loads.

In a fusion reactor, the less frequently encountered case of volumetric heating is found due to the presence of significant neutron and  $\gamma$ -radiation. For the volumetric heating, the steady-state energy balance for a volume  $dV=A^*dz$  with enthalpy  $H$ , a volumetric heat source  $\dot{\Gamma}$  and heat flow  $\dot{Q}(z)$  at the height  $z$  with  $z = z_0 = 0$  on the hot surface increasing towards the cooled side at  $z = z_c$  is described as

$$\frac{dH}{dt} = 0 = \dot{Q}(z) + \dot{\Gamma}A dz - \dot{Q}(z + dz) \quad (5.1.3)$$

The equations describing the heat transfer through the plate and boundary conditions are as follows:

$$\dot{Q} = -\lambda A \frac{dT(z)}{dz} \quad (5.1.4)$$

$$\left. \frac{dT}{dz} \right|_{z=0} = 0, T(z_c) = T_c \quad (5.1.5)$$

From 5.1.3, it follows that

$$\frac{d\dot{Q}}{dz} = \dot{\Gamma}A dz \quad (5.1.6)$$

Taking the derivative of 5.1.4 and inserting 5.1.6 leads to

$$\dot{\Gamma}A dz = -\lambda \frac{d^2T(z)}{dz^2} \quad (5.1.7)$$

5.1.7 is integrated once, then expanded with the independent variable  $dz$  and integrated again. With the boundary conditions given in 5.1.5, the temperature distribution is given as

$$T(z) = -\frac{\dot{\Gamma}}{2\lambda}(z^2 - z_c^2) + T_c \quad (5.1.8)$$

As for the first case, the temperature distribution is inversely dependent on  $\lambda$ . Because of the quadratic dependency on  $z$ , the mechanical deformation is modified, but the dependency proportional to  $\alpha/\lambda$  remains.

Plot 5.1 shows  $\alpha/\lambda$  for a selection of materials plotted against  $E$  as the merit number against deformation by external forces – e.g. through the interface. The materials are chosen based on general feasibility in a fusion reactor with the requirements given in Chapter 3 and cover a wide range of the feasible materials.

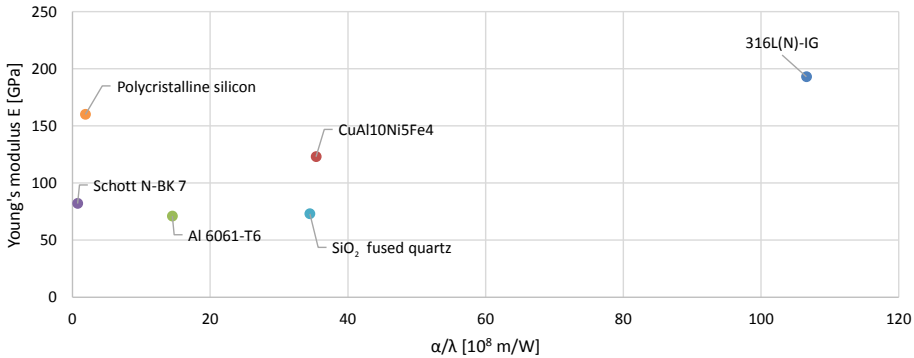


Figure 5.1: Stiffness against external forces versus thermo-mechanical stability. Values from [32] (Si, SiO<sub>2</sub>, Al 6061-T6), [88] (Schott N-BK7), [7] (316L(N)-IG, CuAl)

For material and design suitability, it is not possible to give single numerical values for suitability. The fitness of a material depends on a number of different, distinct needs with the relative importance of the influences depending on the diagnostic system requirements and overall system layout. In addition, a number of solutions exist that address very specific issues, thus preventing the formulation of a general selection choice. For example, a material with hard inclusion might be coated with a thick layer of nickel first, enabling polishing to optical roughness. Table 5.1 gives a high level evaluation on the fusion-relevant requirements of ceramics and metals for a number of considerations.

With the wide range of requirements, the actual selection of the substrate material depends on the specific system requirements. As for non-fusion optical systems, ceramics, including glass ceramics, provide overall higher optical quality. The increased mechanical complexity can be worthwhile for diagnostics requiring a maximum of stability against aberrations and diffuse reflectivity from surface roughness. Because of the complexity involved in connecting ceramic substrates to a cooling system, locations with elevated heat loads are problematic, especially for mirrors with heat sensitive coatings requiring cooling.

Table 5.1: General requirements on mirror substrates.

Requirement	Ceramics	Metals
Possibility for cooling and heating	Problematic: exchange of heat by limited contact conduction and radiation	Good: internal cooling channels feasible and better contact conductance (ductile material)
Suitability for elevated temperature	Limited: depending on coating (coating required)	High for uncoated mirrors, otherwise depending on coating
Substrate mounting interface complexity	Higher: conformal structure for brittle material, no material with $\Delta\alpha$ of $0\text{K}^{-1}$ to stainless steel	Lower: depending on $\Delta\alpha$ .
Versatility for general manufacturing	Limited: brittle material limits methods	High
Design space requirement	Higher: substrate may be small but mounting structure required	Lower: additional functionality easily built into substrate
EM forces (Disruption)	None to low: most materials are good isolators	Higher: rising with increasing electrical conductivity
Substrate requirements with no specific influence from fusion		
Ability to polish	High: best for glass ceramics.	Wide: range from very good (Al) to problematic (steels with carbides, nitrides)
Need for coating	High: translucent or low reflectivity in visible spectrum.	Less: bulk material reflectivity from $\approx 50\%$ (polished Mo, stainless steel) to $\approx 90\%$ (Al)
Ability to coat	Good: wide range of reflective coatings and know-how.	Partially limited: lack of coating experience for non-traditional mirror substrate metals

The main advantage of metallic substrates is the possibility of a smaller overall mirror footprint with integration of additional functionality into the mirror substrate where required by the fusion environment. Examples include direct active temperature control or the remote handling interface. The avoidance of interfaces between highly dissimilar materials, as are present with ceramic substrates, lends itself to reduced complexity in the design. For material combinations with zero difference in the coefficient of thermal expansion ( $\Delta\alpha = 0 \text{ K}^{-1}$ ) between support structure and mirror substrate, the optical system represents a passive athermal design as long as no spatial thermal gradients are present.

In diagnostic systems where the reflectivity of high-melting point metals such as Mo or Rh is sufficiently high, the use of a bulk polished substrate which can be allowed to heat up to high temperatures allows simplifying the thermal control of the mirror even for the most highly loaded mirrors in the direct line of sight of the plasma.

## 5.2 Adjustment during assembly

As the achievable manufacturing accuracy is in general below the positioning requirement of optical elements, it is necessary to provide adjustment options on a number of mirrors inside the multi-mirror optical chains of fusion diagnostic systems. Because of the complications arising from the environment inside the torus, it is beneficial to realise only a minimum set of adjustments inside the vacuum vessel. Additional alignment of the system should be realised with the in-air optical elements of the diagnostic system.

As a result, the first goal of alignment for the in-vacuum adjustments is to aim the light in order to enable imaging of the field of view through the vacuum window, which is limited in size and acts as an additional aperture located far from the entrance aperture of the optical system. This aiming can be realised by rotation around the mirror's local X and Y axes ( $R_x/R_y$ ; tip/tilt). The other four DOF influence mostly the imaging quality and are included in the considerations only where they can be provided without an increase in mechanical complexity.

Because of the limited access to systems inside the vacuum and complications arising from feed-throughs and movement of mechanisms, adjustment of in-vacuum mirrors for ITER and DEMO is deemed sensible only during assembly and maintenance times with direct access to the mirror. As a second consequence of the limited access, it is critical that the mirror adjustment mechanism is stable over the long term against all operational loads. For ITER, the design goal of the in-vacuum diagnostic components is to provide the operational time of 20 years with no maintenance.

Owing to the wide range of possible mirror sizes, loads and adjustment requirements of the different diagnostic systems, no single proposal of a mirror adjustment mechanism is given. Four groups of principal alignment mechanisms, based on common advantages and disadvantages inside the fusion reactor primary vacuum chamber, have been identified and are discussed (see also Figure 5.2): a) adapting the interface, b) flexible hinges, c) extended shaped contact and d) pre-loaded small contacts. In the discussion, the general design requirements, such as adjustment step width, locking of the alignment and cross talk between alignment directions, are only addressed in passing and have to be included in the diagnostic design on a per-system basis.

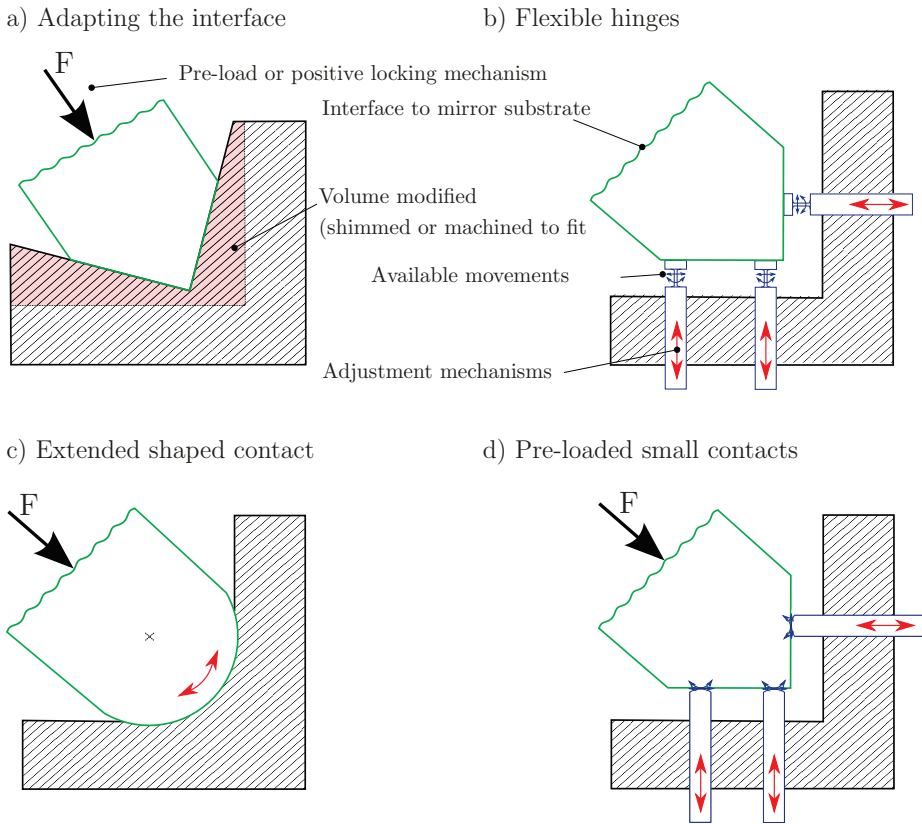


Figure 5.2: 2D sketches of the adjustment principles. Each principle has a number of possible realizations that can differ even in the basic features such as the number of degrees of freedom for adjustment.

### 5.2.1 Adapting the interface

The adjustment principle of the first concept group is to provide a mirror mounting interface with a location and orientation where the optical system is in alignment. Two approaches are possible: Machine the interface to compensate the deviations or introduce intermediate element(s) – e.g. shims.

For the first solution of machining the interface to fit, the compensation parameters for the mirror chain needs to be known before final machining of the adjusted interface can take place. The available degrees of freedom for adjustment depend on the amount of machining that can be realised. All six DOF may be used to compensate for deviations, but the required adjustment accuracy may not exceed the combined inaccuracies of measurement and machining the assembly interface.

For shimming, either machining of the shim element to size or the use of multiple pre-fabricated shims is possible. For the simplest solution with a bolted, shimmed interface, example realizations are shown in Figure 5.3. In the given examples, adjust-

ment of two rotations around and movement perpendicular to the interface are possible. In this case, the interface needs to be oriented as required by the adjustments. Additional designs of shimmed interfaces exist with different DOF for adjustment. Selection of the shim configuration depends on the system requirements.

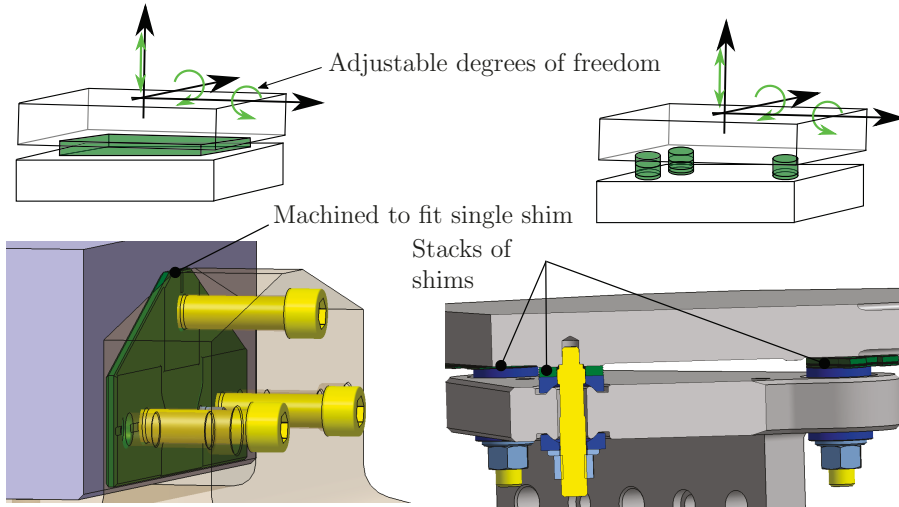


Figure 5.3: Designs for bolted, shimmed interfaces. Left: single, machined-to-fit shim. Right: three stacks of shims selected to compensate deviations (with angular compensation on bolts).

The main advantage of adapting the interface to dimensions compensating deviations in the context of a fusion reactor lies in the robustness of the adjustment. Besides settling in the interface, alignment cannot be lost. The required manufacturing, adjustment and complexity can be assessed early.

The adjustment principle does not automatically include any structure to compensate for differential expansion within the interface. Frictional movements between the contacting surfaces have to be taken into account. In addition, forces can be transmitted through the interface. In cases where critical loads internal to the interface are encountered, a compensating structure can be added in between the interface and the mirror to reduce the transmission of forces to the mirror substrate at the cost of an increased system complexity.

The main disadvantage results from the complexity of the adjustment. Depending on the actual design implementation, multiple steps are necessary to finalise the adjustment. In case of the machined-to-fit interface, the necessary compensation parameters have to be determined before finalising the interface, introducing significant machining operations late into the manufacturing process. With shims, each iteration of the adjustment necessitates a partial disassembly of the mirror.

Re-adjustment during maintenance for the machined-to-fit interface – e.g. after exchange of one mirror in the mirror chain – is limited to replacement of the adjusted mirror: Precision machining of activated parts is not seen as a realistic option. For

Table 5.2: Comparison of machining the interface and shimming the interface.

Option	Advantages	Disadvantages
Machine interface	Maximum stability, no additional elements	Limited re-adjustment capability
	Up to six DOF can be adjusted	Late machining operation necessary on critical component Accuracy limited to measurement + machining accuracy No adjustment of compensation
Shim interface	Late machining not necessary or less intrusive	Additional contacts, reducing interface contact conductance
	Higher accuracy with closely spaced shim stepping	Adjustable DOF determined by interface orientation
	Change of adjustment feasible	

the shimmed solution, the manipulation of the shims by remote handling needs to be taken into account during the design phase and the overall system layout is required to provide sufficient access to the shims.

### 5.2.2 Flexible hinges

Flexible hinges allow relative movement between parts, both for adjustment and other changes in dimension including differential thermal expansion. For adjustment, the design goal is to allow the adjustment motion but realise an overall stiff structure against the forces acting on the mirror by combining the stiff direction of the flexible hinges to lock against the forces.

A number of designs based on flexible hinges exist and Figure 5.4 gives a few examples for primarily rotational hinges. (a) is a sturdy realization for one rotational alignment with a flat spring as hinge. (b), pins with flex hinges (hinges need to be adapted to the bending direction), can realize two rotations within a relatively small space. (c) allows repeated flexing of one rotation and is stiff against lateral shift.

The biggest advantage of flexible hinges is the inherent absence of frictional motion between surfaces. In the absence of plastic deformation and creep, the mirror position is stable against permanent changes. Differential thermal expansion between parts can be compensated but has to be taken into account in dimensioning. The hinges are free of play without the need for a pre-load.

While the springs do not act as thermal isolators, they introduce a resistance. In case of a design as given in 5.4(b), volumetric gamma heating close to the plasma leads to elevated temperature of the springs from the heat generated in the central enlarged section, affecting mirror alignment. Thus, the dimensioning of the springs is a balancing of flexibility, force-bearing capability and thermal management.

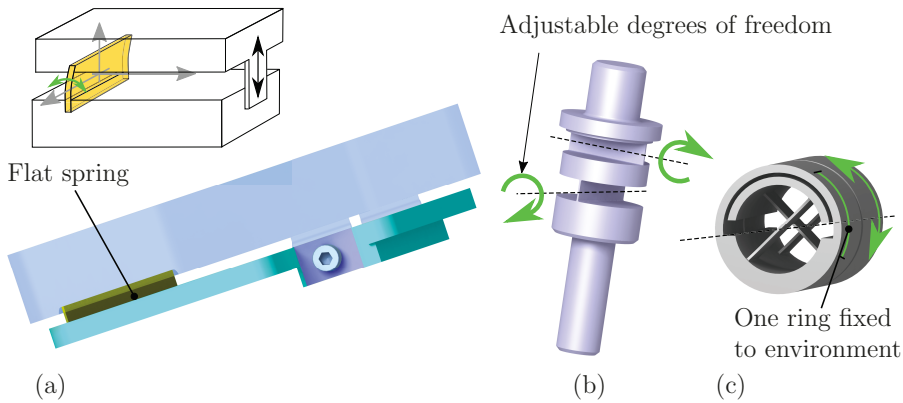


Figure 5.4: Assortment of spring elements: (a) Single rotation stage with flat spring. (b) Flexible post for two rotational degrees of freedom and limited lateral movement. (c) Flexure pivot by C-Flex Bearing Co., Inc. for one rotation.

Care has to be taken with dimensioning. With the pre-stress from adjustment, the load-bearing capability of the spring elements can be exceeded quickly. Forces during plasma disruptions, coupled with elevated temperature and differential thermal expansion in the interface, pose a complex problem for dimensioning. Higher spring stiffness required to bear elevated loads results in a reduced adjustment range.

The flexible hinges are most advantageous for smaller mirrors at moderate loads. The actual limits of application depend on the available design space and adjustment range. In case dimensioning of the flex hinges is possible, they provide a clean interface with long-term stability against loss of alignment. Flexible hinges are the first choice for repeated motion in vacuum.

### 5.2.3 Extended shaped contact

The ‘extended shaped contact’ group is characterised by movement between two rigid, matched surfaces realising the rotational or lateral adjustment. It is the principal generally found in, e.g. goniometer stages. Separation of the interface under off-normal forces is realised by a pre-load or positive locking mechanisms in the direction of the loads. The contact is only meant to see a limited number of movement cycles in the interface with the aim of no movement after alignment. It exhibits many of the same properties as the first group but allows direct alignment.

Designs for adjustment of one rotational axis are given in Figure 5.5. Linear alignments are possible but not discussed here since they are not as necessary for the in-vacuum fusion mirrors. Multiple axes can be realised by stacking multiple stages or with ball-in-sphere-type arrangements (see, e.g. Figure 5.7). Designs where the mirror is mounted on a tube with separate vacuum flange, allowing aligning from the air side of the system while the vacuum vessel is vented, as proposed for the core LIDAR diagnostic in ITER (see [67]), also fall within this group.

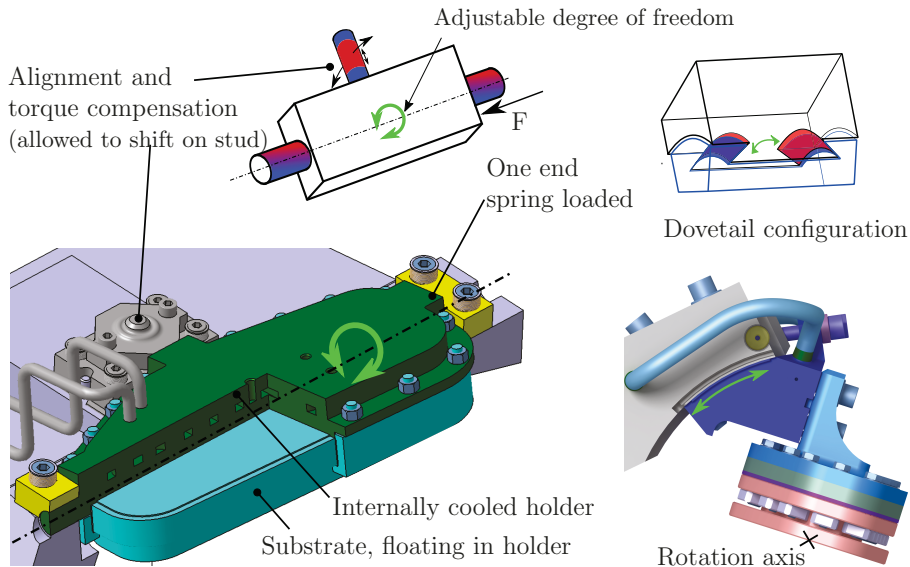


Figure 5.5: Extended shaped contacts as bearing: (a) Gliding axis in pre-loaded bushing. (b) Goniometer arrangement with, e.g. dovetail sliding contact.

The main advantage of extended shaped contacts is the ease of adjustment while stability under high loads is retained. With the large surfaces in contact, the thermal contact conductance helps reduce temperature differences in the interface. The interface design can and must be adapted to different construction spaces.

A critical point is the compensation of differential thermal expansion over the interface. Dissimilar materials and temperature differences can only be allowed as long as sliding in the interface is possible without ill effects. In Figure 5.5 (b), this is solved by active temperature control of both sides of the interface, avoiding thermal gradients. Cold-welding of the contact in case of local sliding inside the interface can prevent re-alignment and lead to permanent change in the alignment.

While designs for a single rotation axis can be simple and robust, this advantage is reduced when multiple axes need to be aligned. The group is best used for aligning a single rotation for mirrors under high forces, as encountered close to the plasma, e.g. metallic substrate first mirrors.

### 5.2.4 Pre-loaded small contacts

The third group includes designs based on the concept of small, pre-loaded contacts in the interface between the aligned and fixed parts of the mirror holder. The contacts are ideally arranged in a manner to constrain, but not over-constrain, the system and shield the mirror substrate from mounting induced forces except for the residual stress from friction. The common realizations are the kinematic and quasi-kinematic mounts in their numerous configurations, as often used in breadboard mounts. Figure

5.6 illustrates a concept for a highly loaded mirror close to the plasma. The design uses two V-grooves angled for adjustment with movable spheres (shown on the right side), restricting two and one DOF, as well as one cone restricting three DOF.

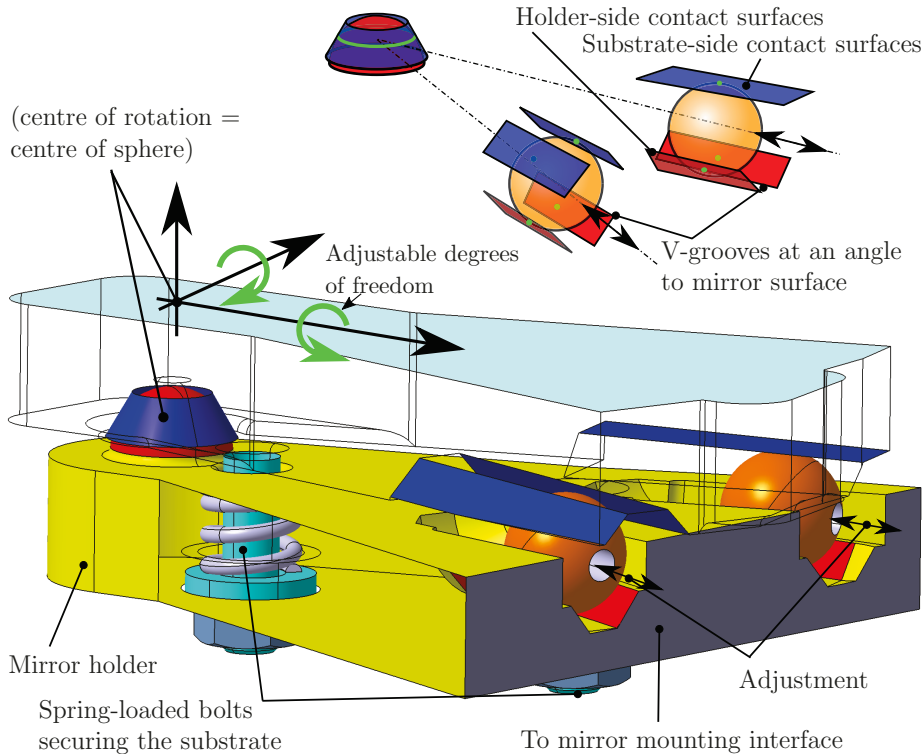


Figure 5.6: Kinematic mounting for two rotational adjustments with three point contacts and a line contact.

With a suitable configuration, movements from thermal expansion and alignment cannot create high stresses in the interface. A slight movement from differential thermal expansion between the support and mirror substrate is encountered in the point contacts.

The interface provides good thermal isolation in the interface if required by the application. It is necessary to prevent a current loop by eddy currents from disruptions through the contacts; otherwise, arcing at the contacts might damage the bearing surface or even lead to point welding. With the interface depending on the pre-load in the interface to work, springs are required. At the location of the mirrors in ITER and DEMO, loss of pre-load due to neutron-induced creep has to be checked for positions close to the plasma.

The main limitation of the concept lies in the load-bearing capacity of the point contacts. For external loads with no fixed direction, the spring pre-load in the contact has to at least match the external load in order to prevent opening of the contact.

One such example is the EM load of ITER, where the plasma current may be run in both directions, with the result of inverting the sign of the load. In the case of a forward-facing mirror of the core CXRS diagnostic system (200 mm\*150 mm, stainless steel), no solution could be found due to the resulting pressure in the contact.

The ability of the contacts to undergo motion is simultaneously the main advantage and a risk. Thermal cycling with each plasma shot, baking cycles, plasma disruptions and vibration of the machine during operation lead to high cycle counts of micrometre and larger movements. With the contact directly in the relevant path for alignment, the impact on contact wear has to be assessed carefully. With the limited load-bearing capacity of the contacts, the application is limited to smaller mirrors farther from the plasma.

### 5.2.5 Conclusions on adjustment mechanisms

Depending on mirror size as well as loads and requirements, different alignment mechanisms should be used. Pre-loaded small contacts are excellent from the optical point of view with high alignment range and decoupling of loads transferred through the interface, but the pre-loaded point contacts are easily overloaded or damaged in a fusion reactor. While flexible hinges offer many of the same benefits and limitations, they do not rely on small contact areas and avoid the need for a constant pre-load; hence, they are preferable for mirrors of limited size in protected positions inside or behind the neutron shielding where external loads are reduced.

For large mirrors and locations with higher loads, adapting the interface and extended shaped contacts can both work. For both designs, the temperature gradient over the interface should be controlled to minimise stress and motion in the contact. Machined-to-fit adjustment provides highest stability where the required late machining of the interface is feasible and the limited tolerance of the machine accuracy is sufficient. Where highest position stability is not required or the late machining is not feasible, shimming for adjustment is a viable alternative.

In addition to the four principles, combinations may be used. Figure 5.7 presents an example where a captured sphere (extended shaped contact) realizes the rotational degrees of freedoms, while a flexible post compensates the lateral shift. With the flexible post relieved from taking the majority of the adjustment motion, it can bear higher operational loads and may be used for the compensation of differences in thermal expansion of holder and substrate, both from  $\Delta\alpha$  and  $\Delta T$ .

Adjustable mirrors inside the vacuum vessel are always at least as vulnerable as the same mirror without adjustment could be. It is critical to assess which in-vacuum mirrors have to be adjusted and where alignment can be reached by other means. At least the possibilities to change the design towards minimizing the critical loads for the adjusted mirror should be considered. For two of the main loads in a fusion reactor, EM forces and volumetric heating, even small changes in the design can result in a considerable load reduction.

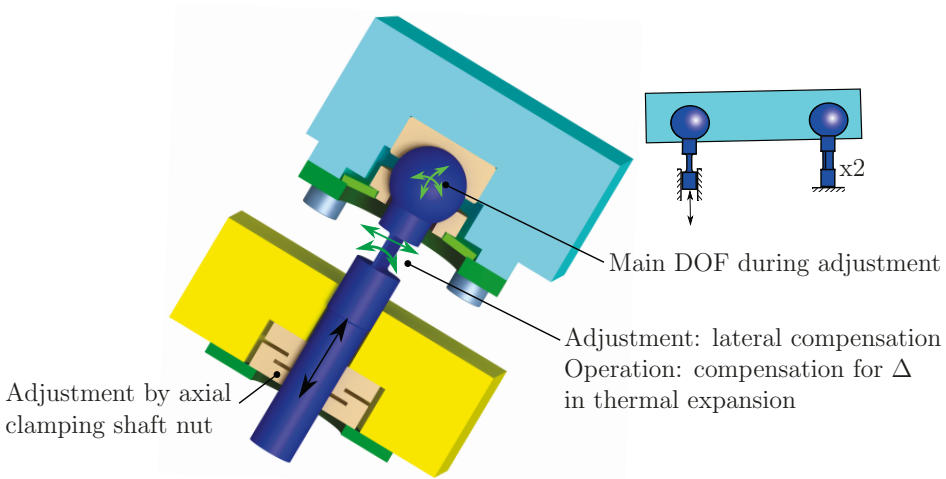


Figure 5.7: Combination of the large surface and flex element to minimise stress from adjustment in the flexible element.

### 5.3 Thermal design

In a fusion environment, a number of goals exist for the thermal design, requiring both cooling and heating of the mirror substrate, depending on the circumstances:

- Cooling during operation where heat loads cause too high of a temperature for the mirror materials or diagnostic operation
- Control of the mean temperature and temperature gradients to achieve the required imaging quality of the mirror train
- Heating to reduce condensation of contaminants on the mirror surface, especially during the early phases of vacuum bake-out

The toolset for thermal design includes both active measures (e.g. fluid circuits) and passive provisions (e.g. design for radiation cooling). In general, multiple methods are present in any design at the same time. Figure 5.8 provides an overview on the principles available inside the fusion environment.

In the following paragraphs, an evaluation of the thermal management options specific to the fusion environment and for in-vacuum diagnostic mirrors is given. Advantages and disadvantages are only discussed where they differ under vacuum conditions to the application in air. In the design step all properties must be taken into account.

**Fluid in direct contact:** The substrate may either act as a vacuum boundary or a separate vacuum boundary can be used with a bonded heat-transfer interlayer. With the substrate as a vacuum boundary, material selection is limited to vacuum-tight and weldable materials to allow for the pipe connections. For a separate vacuum

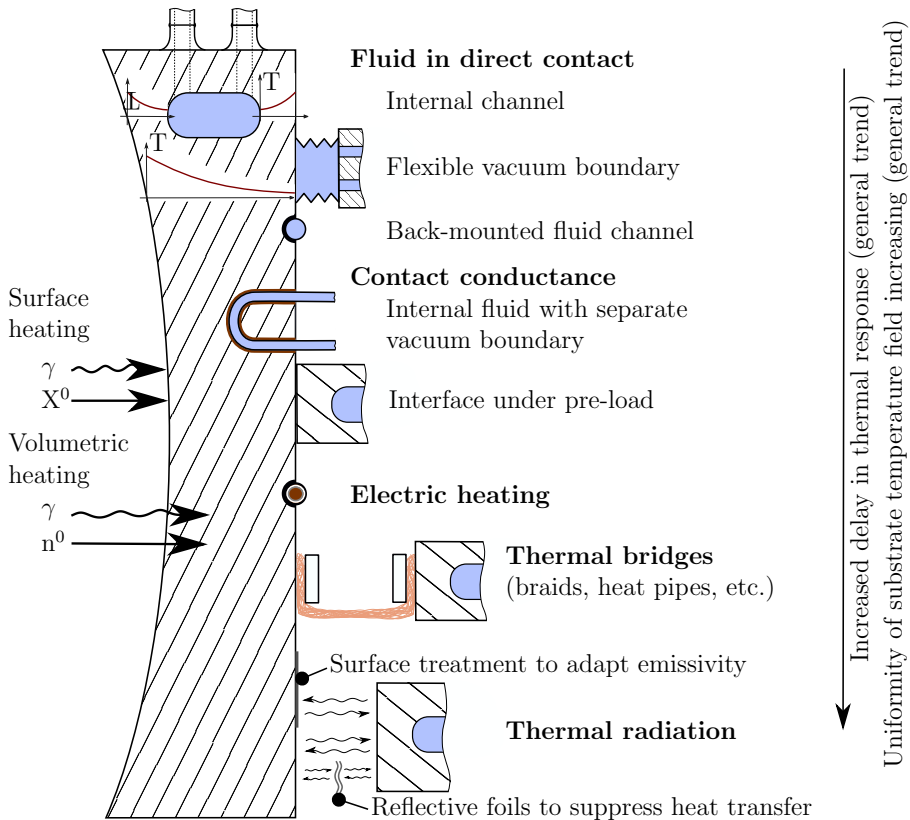


Figure 5.8: Design options for temperature contact.

boundary, forces by the bond and material pairing – e.g.  $\Delta\alpha$  – have to be taken into account.

With the ability to apply heating and cooling at specific locations through the component design and at specific times by steering the flow, control of the temperature is high. Bending of the substrate due to volumetric heating can be approximately compensated for by a channel located in the substrate centre, creating opposing thermal gradients across the substrate. To succeed in the compensation, the distribution of surface and volumetric heating have to be known and optimization can only be done for certain heating scenarios.

The general drawback of mirror surface ripples due to the localised heating and cooling is reinforced where the fluid feed temperature is not stable, as is likely the case for the main cooling fluid of any reactor. In addition, assembly and maintenance of the mirror is greatly complicated due to the cutting, welding and inspection required at the supply pipes with remote handling equipment. The space required for the remote handling equipment also has to be reserved.

The use of a flexible vacuum boundary – e.g. bellows – around a large portion of the substrate allows fluid direct contact on a larger surface. It also creates the

possibility of complex substrate-mounting mechanisms inside a fluid, avoiding the problems introduced by the vacuum environment for the encapsulated mechanisms. Due to the inherent vulnerability of the boundary, the problems with inspection and the resulting maintenance effort, the use of such an encompassing vacuum boundary is not seen as viable.

**Contact conductance:** Internal routing of pipes with a pre-loaded thermal contact to the surrounding substrate can be realised e.g. by the use of a permanently flexible mesh, but stability of the contact under repeated application of forces is seen as problematic. Contact conductance on a substrate surface is not seen as a standalone solution due to the forces transferred into the substrate, but rather as an effect that can be advantageous at the mounting location of the mirror substrate.

Other than the reduced contact conductance in the interface inside the vacuum, the function is no different than outside of fusion as long as the pre-load can be maintained.

**Electric heating:** The use of mineral-insulated resistance wires inside a fusion reactor requires isolated feed-troughs at the vacuum boundary. Close to the plasma, isolation enclosing the supply lead might be required to avoid shorts from electrically conducting deposits from the plasma at the wire stand-offs. Thermocouples are seen as necessary to allow monitoring of the temperature. Other aspects of electrical heating are not changed by the presence of a vacuum.

**Thermal bridges:** An element with good thermal conductance is introduced between substrate and a temperature-controlled body, thus avoiding the problem of transfer of forces and bridging gaps to the cooled structure. The main benefit is the avoidance of any vacuum-tight connections and easy handling for maintenance. The delayed reaction and the required temperature gradient prevent use of the machine thermal source for keeping the mirror surface above the general environment temperature.

Heat pipes, as a novel way of a high-capacity no-maintenance thermal link, are limited in operational temperature range, but fusion-relevant temperatures are available. The operational range for the high thermal transfer capacity link might be limited. Close to the plasma, additional fusion specific complications are:

- In case the pipe is damaged, a virtual leak is created. Detection in the closed reactor is problematic, as no external tracer gas can be introduced to pinpoint the leaking component
- The stability of the heat transfer fluid under the high flux neutron and gamma radiation conditions has to be shown. For fluids with covalent bonds, the amount of decomposition should not lead to excessive loss of heat transfer and no combustible mixtures may be created

**Thermal radiation** as the heat exchange path is not modified by the fusion environment. The heat transfer may be controlled using intermediate structures and

coatings with defined emissivity, but the materials must conform to the fusion environment requirements.

### 5.3.1 Conclusions thermal design

Wherever possible, thermal management should rely on thermal radiation and contact conductance in the substrate interface as all additional connections to the substrate increase complexity of the mirror. On the other end of the spectrum, internal fluid flows allow for the most direct influence of the substrate temperature with minimal induced forces at the cost of an increased risk of leaks and a higher complexity of mirror exchange during maintenance because of to the need for re-welding and inspecting the vacuum boundary.

With solutions relying on thermal contacts, care must be taken in ensuring that the thermal contact does not create unacceptable distortion by the induced forces and resulting thermal field. It is also important that the maintenance effort required disconnecting the thermal connection from the permanent, actively cooled or heated part is checked. For spring pre-loaded contacts, the long-term stability of the contact under thermal cycling must also be proven.

In all designs, especially those with more indirect thermal paths, early heat-up during bake-out ramp-up to prevent condensation can be achieved by a separate mirror fluid circuit with the ability to raise the temperature earlier than the environment, bypassing the time lag of the thermal contact. As the increase in system complexity for a solution with separate fluid circuit is significant, the benefits have to be evaluated critically, especially as a mirror with internal fluid flow already feature a fast thermal reaction and are likely to exceed the temperature of the environment during the heat-up phase of vacuum bake-out.

Electric heating can be used to keep mirrors permanently above environment temperature, preventing significant condensation of volatiles but the system-level design complexity, especially with the degradation of isolators, has to be checked in detail.

## 5.4 Conclusions on principal design considerations

Due to the differences in specific requirements of individual fusion diagnostic systems, no reasonable, single, standardised mirror design for general use can be proposed. Instead, common functions of mirror systems have been regarded with a focus on the specific requirements of the fusion environment.

For the substrate choice, adjustment mechanism and the substrate temperature control, solutions suitable to operate in the primary vacuum of a fusion reactor were described with their limitations. For all of these major functions, workable solutions were found. While it is possible to come up with impossible to fulfil requirements for the mirrors, the general possibility of realising optical mirrors inside the vacuum vessel of an extended pulse-time D-T fusion reactor can be answered in the affirmative.

To arrive at a well-rounded design of the mirror, the considerations discussed have to be brought together with the system-level layout and design of the complete diagnostic system in mind. A bottom-up approach looking only at the isolated mirror is not seen as promising.

# Chapter 6

## Concept design for ITER core CXRS secondary mirrors

The general design considerations of the last chapter are applied to a specific diagnostic system of ITER, the charge exchange recombination spectroscopy (CXRS) on the plasma core, and the beam emission spectroscopy (BES) system. These systems rely on UPP#3 to couple light from the interaction zone of the DNB and the plasma into optical fibres outside the vacuum boundary. The critical requirement for the optical system in the port plug is to transmit as much light as possible to allow evaluation of the signal against a strong background. The spatial resolution requirement, on the other hand, is limited. A maximum root mean square radius of the point spread function of  $150\ \mu\text{m}$  at the fibre coupler, with a magnification in the range of  $1/35$  to  $1/40$  is required from the port plug optical system [43].

First, the underlying physics and layout of core CXRS is introduced and the diagnostic specific design requirements are given. Afterwards, a design for the secondary mirrors in UPP#3 is proposed, based on the considerations of the previous chapter. The design addresses the general requirements as identified in chapter 3, and is aimed at the specific needs of core CXRS and BES of ITER. Thermo-mechanical simulations show the feasibility of the design under the complex loads in ITER both for the mechanical integrity and optical requirements.

### 6.1 ITER UPP#3 layout

Core CXRS and BES share one optical system inside UPP#3. Both systems together require light of wavelength  $460$  to  $663\ \text{nm}$  to be transferred out of the vacuum vessel. An étendue times transmission of  $1\ \text{mm}^2\ \text{sr}$  is set as the target for the in-port optical system and fibres to the spectrometer.

The optical system layout of UPP#3, which is used as a design basis in this work, is shown in Figure 6.1. The light enters from the plasma side on the left and is guided by seven mirrors to the mounting flange on the right, where the vacuum window is located. The grey structure represents the standardised UPP shell while the blue block is the diagnostic shielding module (DSM), which acts also as an optical bench for the system. Some subsystems of the core CXRS diagnostic inside the UPP, including the first mirror cleaning source and most piping, are hidden for clarity.

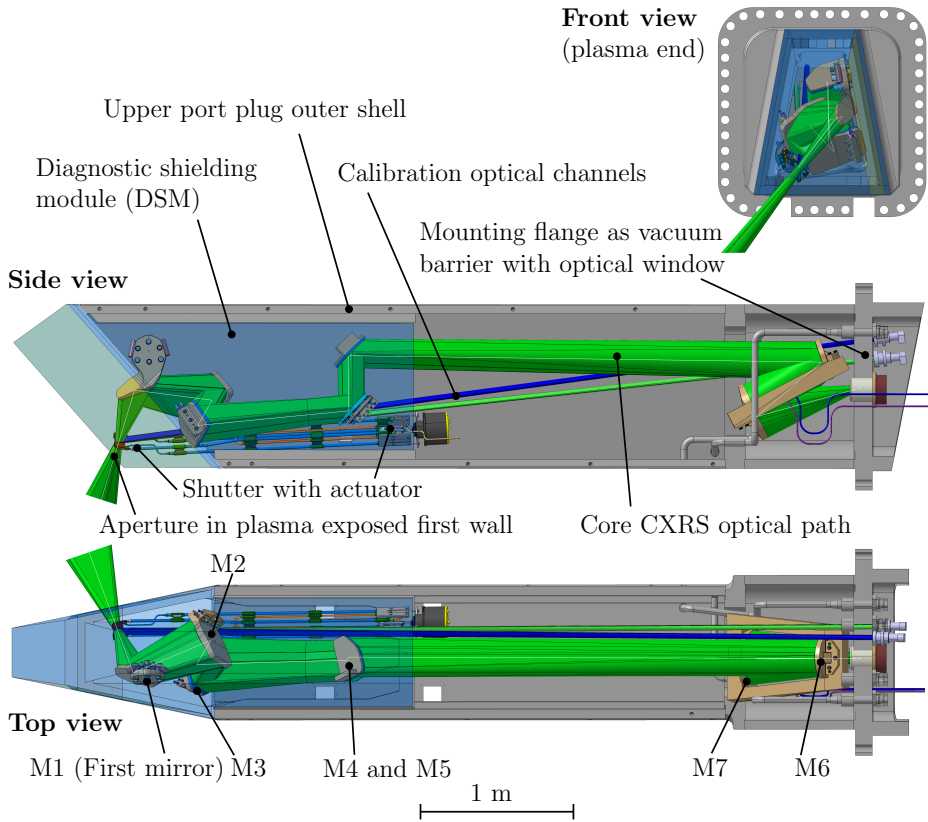


Figure 6.1: Overview of UPP#3 with the main optical path ('Large M1') in green and standardised UPP shell in grey.

The mirrors are separated in two groups: the mirrors in the first group, consisting of mirrors 1 to 5, are individually mounted to the DSM. Mirrors 6 and 7 located in the rear section near the vacuum window and mounted to a separate support structure. A more detailed discussion of the optical system and diagnostic subsystems inside the port is given in [43] and [66].

Over the course of this work, the optical layout in UPP#3 has been modified several times with involvement of the author, including one major redesign initiated by mirror lifetime considerations and to decrease the complexity of the optical system. A strong influence on the changes of the optical layout was the mirror design shown in this work as the layout and mirrors' mechanical realization were modified together, enabling the design as presented. A detailed description of the initial layout of the port, the core CXRS reference design, can be found in [49].

A modification to the system layout driven by the mirror design was shifting the location of the mirrors towards the outer walls of the DSM, thus allowing the maintenance strategy as proposed in the following section and accommodating changes

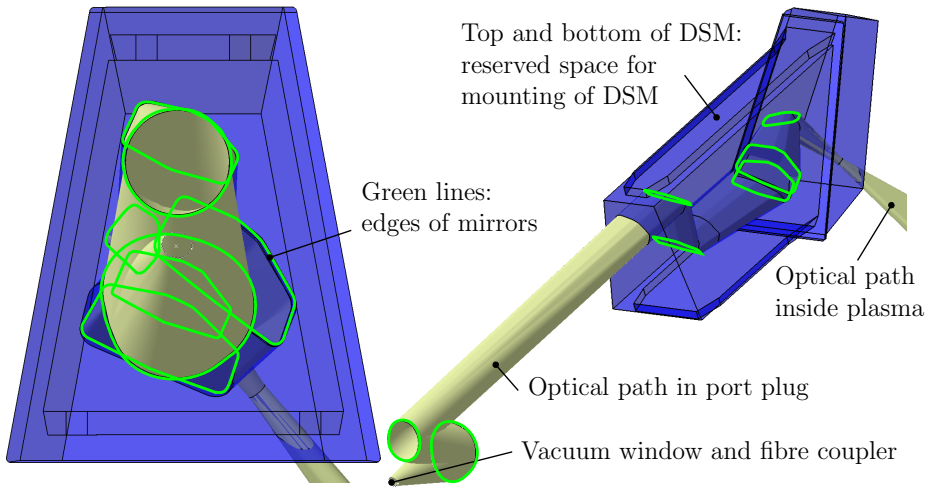


Figure 6.2: Available design space in UPP#3 (DSM) compared to the optical path size. Additional systems in UPP#3 and functions restricting the design space are hidden for clarity.

in the generic UPP design by the ITER Organization. In addition, the design space as anticipated for the mirror assemblies and all assembly and maintenance operations were reserved so that no other systems could block implementation of the mirror design.

The available design space for the core CXRS mirrors is restricted by the UPP shape (see Figure 6.2): The optical channel is coloured yellow while the green lines highlight the edge of the optical path at the mirrors. The mirrors may not stick out of the DSM + DFW (in blue). The two rear mirrors (6 and 7) are also bound to the trapezoid envelope of the port structure, as the whole system is inserted from the trapezoid plasma facing end. No access from the air side of the port is possible with the vacuum boundary and structural material of the port.

Additional restrictions arise from the diagnostic subsystems, such as a shutter and calibration components, but also external functions, such as the space reservation for the bolts in mounting the DSM and DFW to the upper port shell. Lastly, radiation shielding favours compact or at least high material fill rate mirror designs since the effectiveness of the radiation shielding present in the port in the DSM region should be maintained at the same level as the surrounding ITER first wall. The shielding is required to protect the superconducting magnets during operation as well as to minimize activation in the port interspace and port cell behind the UPP#3, in accordance with the ALARA (as low as reasonably achievable) principle since human access during maintenance is foreseen.

On the system level, the mirrors feature the general characteristics, as given in Table 6.1. The mirror surface materials were chosen based on preliminary knowledge of material reliability at the local conditions, light throughput requirements and mirror lifetime.

Table 6.1: Baseline mirror dimensions, shape and mirror surface materials for the large M1 option core CXRS in-port diagnostic mirrors.

Mirror	Shape	Approx. size [mm]	Mirror surface material baseline
M1	flat	270 x 120	Polished single crystal Mo; No coating
M2	toroidal	400 x 230	Rhodium coating
M3	flat	360 x 210	Rhodium coating
M4, M5	flat	280 x 200	High reflective multilayer dielectric coating (Target reflectivity >98%)
M6, M7	off-axis ellipsoid	∅250 and ∅370	High reflective multilayer dielectric coating (Target reflectivity >98%)

## 6.2 Baseline design fixed mirrors

The baseline design of Mirrors 2 to 7 is put together on the basis of the function-specific solutions discussed in Chapter 5, as applied to the core CXRS specific requirements. The first mirror of core CXRS is not covered by the baseline design proposal, as the system-level substrate choice of single crystal molybdenum necessitates a different approach. The implementation for the second mirror is shown in Figure 6.3. A list of design drivers for the base concept is given below. The individual design realizations are discussed in detail subsequently. The primary driver of the design is integrating the relatively large mirrors into the narrow UPP and enabling maintenance for the mirrors.

### Limited design space

Monolithic body, avoidance of extensive structures by integration of functionality – e.g. handling interface – and elimination of auxiliary functionality: No compensation of thermal expansion with only uniform temperature at interfaces and  $\Delta\alpha = 0$  within interfaces.

### Condensation on mirror may degrade performance

Substrate heating possibility with internal fluid flow  
 Substrate material choice for only same material coolant pipe welds (reliability of vacuum tightness)

### Fluctuating thermal loads

Design avoiding thermal gradients at critical locations affecting mirror surface deviations

### Optical system desired in-focus from 20 °C to 240 °C

Athermalization with  $\Delta\alpha = 0$  between mirror substrate of and inter-mirror structure:

**Temperature of DSM neither uniform nor constant**

Localised mount: Connection to the DSM at one location only

Decoupling of substrate with optical surface and mounting interface (to a limited extent)

**Maintenance in the hot cells**

Orientation of interface and direction of assembly motion towards the lateral side of the DSM where sufficient access is available

Self-guided positioning of the substrate during insertion

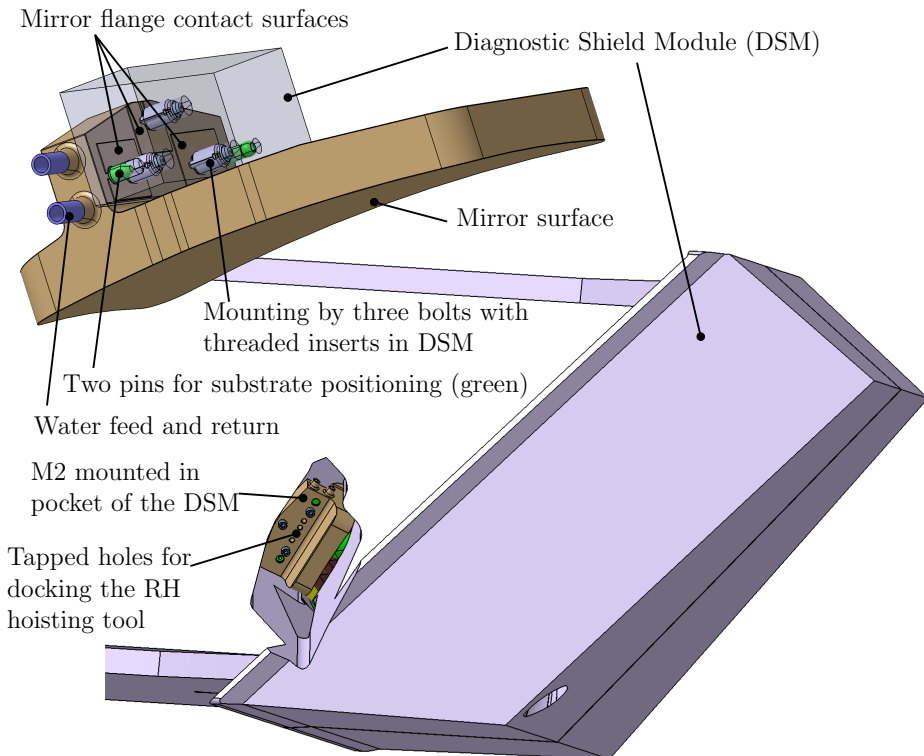


Figure 6.3: Baseline design for the core CXRS second mirror.

The proposed mirror design consists of the mirror substrate directly bolted to the DSM. The DSM acts as an optical bench for the mirror train. All functionality is either integrated into the mirror substrate – e.g. the docking interface for the remote handling transport frame – or avoided altogether – e.g. providing compliance for differential expansion by either temperature gradients or  $\Delta\alpha$  between bodies.

The mirror body is made from stainless steel 316L(N)-IG with coating applied to the mirror surface. The mounting interface is located on the rear of the mirror, angled  $90^\circ$  to the mirror surface, thereby decoupling the mechanical deformation from mounting on the mirror surface. It is oriented and shifted differently for each mirror to

be best reachable from the side of the DSM, enabling assembly and disassembly. The mirror is in contact with the DSM only at the main interface to avoid any influences on the mirror from possible temperature gradients and deformations within the extended structure of the DSM. The mirror is positioned by two pins and held by three bolts. The middle bolt creates a triangle and helps prevent tilting around the interface under external loads. In case it is deemed necessary, the mirror design includes internal fluid channels, uniformly distributed within the whole substrate and including the mounting interface. The water connection is provided at the mounting flange to minimize the influence of welding close to the mirror surface.

### 6.2.1 Stainless steel substrate

The choice of the substrate material is central to the mirror design as it influences all aspects of the concept. Based on the discussion in 5.1, the stainless steel 316L(N)-IG (ITER grade) is chosen for the following benefits, which, in sum, enable the compact design:

- The quantity of stainless steel of this type is not limited inside ITER
- Ductile material allowing direct bolting and no risk of shattering from external or internal loads – e.g. due to thermal gradients from an ingestion event
- Identical  $\alpha$  avoiding the need for structures compensating differential thermal expansion, saving design space
- Identical  $\alpha$  with the inter-mirror mechanical structure allows for stable passive athermal behaviour of the optical system in the absence of thermal gradients
- Similar material as the cooling system pipes allowing direct connection to the cooling system
- Limited EM forces during magnetic transients due to high electric resistivity of  $80 \mu\Omega \text{ cm}$  at  $100^\circ\text{C}$ , compared to, e.g. Al at  $\leq 10 \mu\Omega \text{ cm}$  resulting in more than eight times the force of the stainless steel.
- Availability of a wide range of manufacturing methods and experience in manufacturing for vacuum compatibility

As alternative material, the bronze CuAl10Ni5Fe4 is included in the investigation for its thermal expansion within  $1 \times 10^{-6} \text{ K}^{-1}$  of 316L(N)-IG and the threefold higher thermal conductance.

The main drawbacks of the material are addressed by simulation and testing. In detail, the drawbacks are:

- High instantaneous thermal expansion of  $16.5 \times 10^{-6} \text{ K}^{-1}$ , coupled with low thermal conductivity of  $15.48 \text{ W m}^{-1} \text{ K}^{-1}$  at  $100^\circ\text{C}$ , promotes a reduction of imaging stability and quality due to mirror surface shifts and deviations in the presence of thermal gradients

Table 6.2: Optical layout suggested tolerances for assembly position accuracy and stability during the nominal 20 years of operation.

	Mirror	Translation			Rotational			Shape	
		[mm]			[mrad]			[Fringes]*	
	time	T <sub>x</sub>	T <sub>y</sub>	T <sub>z</sub>	R <sub>x</sub>	R <sub>y</sub>	R <sub>z</sub>	Curv.	Irr.†
	M2 assembly	±0.5	±0.5	±0.1	±3.5	±3.5	±3.5	±5	±5
	M4 assembly	-	-	±0.1	±0.873	±0.873	-	±5	±5
	M6 assembly	±0.1	±0.1	±0.1	±0.873	±0.873	±0.873	±5	±5
	M2 operation	±1	±1	±2	±3.5	±3.5	±30	±100	±100
	M4 operation	-	-	±2	±0.873	±0.873	-	±50	±50
	M6 operation	±0.5	±0.5	±1	±0.873	±0.873	±30	±1	±1

- The presence of residual hard nitrates and carbides in the material limits the achievable surface roughness by polishing. The reported achieved quality of R<sub>a</sub> slightly below 5 nm is just sufficient for the core CXRS diagnostic system.

### 6.2.2 Interface for mirror positioning and mounting

The interface of the mirrors to the optical bench is critical for the position accuracy of the mirror surface. For the DSM mounted mirrors 2 to 5, the tolerance on the DSM side of the interface is limited by the DSM manufacturing accuracy, which is restricted for the DSM as it is a multi-tonne structure with a size of about 2 m x 1 m x 0.6 m. When designing the mirrors, the manufacturing accuracy of the DSM could not reliably be determined, but was estimated to be no better than ±0.1 mm and ±3 mrad for the mirror mounting surfaces and pin holes located in a shallow pocket of the DSM (Figure 6.3). As this is outside the required mounting accuracy of the mirrors (Table 6.2), direct manufacturing of the mirror components to nominal geometry is not possible; instead, an accurate measurement of the as-manufactured DSM geometry and customization of the interface on the mirror side is required. The measurement accuracy of the DSM side mirror interface geometry is estimated to be within 10 μm, as can be reached with portal coordinate measuring machines – e.g. Zeiss ACCURA [18].

The method proposed for the accurate mounting is positioning by two pins (limiting two shifts and one rotation) and the three pads where the mirror contacts the DSM (restricting one shift and two rotations; see Figure 6.4). The use of pins and pads allows finalization of the mirror positioning elements late in the manufacturing route by adapting the pin and pad locations on the mirror substrate interface side in accordance with the as-manufactured geometry of the DSM. It also limits the required number of accurate geometries for the interface in the DSM to a flat surface and two

\*Curvature and irregularity calculated for one fringe as 0.5\*0.6328 μm (wavelength of HeNe laser)

†Irregularity as 50% spherical aberration and 50% astigmatism (ZEMAX TIRR).

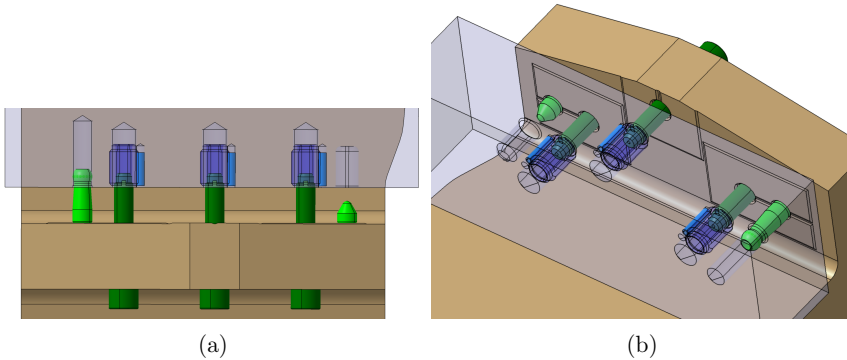


Figure 6.4: Mirror positioning interface for the secondary mirrors. a) Top view and b) isometric view. The mirror substrate is shown in brown, bolts and pins in green, and DSM with threaded inserts in blue.

holes at  $90^\circ$ , simplifying the machining of this large part with limited accessibility at the location of the mirror interface. The interface avoids trapped volumes through the tapping of all blind holes and the inclusion of evacuation channels for all internal volumes.

The aluminium bronze  $\text{CuAl10Ni5Fe4}$  is chosen as pin material based on the close match of the thermal expansion coefficient to stainless steel 316L(N)-IG (20 to  $100^\circ\text{C}$ ):  $\alpha_{m,316L(N)-IG} = 15.9 \times 10^{-6} \text{K}^{-1}$  versus  $\alpha_{m,\text{CuAl10Ni5Fe4}} = 16.2 \times 10^{-6} \text{K}^{-1}$ ) and the self-lubricating properties of the material pairing in vacuum. The softness of the  $\text{CuAl10Ni5Fe4}$  also enables recovery by drilling out the pins without damage to the positioning holes in the DSM in case the mirror should get stuck. For the same reason, threaded inserts for the three mounting bolts made from the same aluminium bronze  $\text{CuAl10Ni5Fe4}$  are included in the design.

The pins are shaped based on the standard remote handling positioning pins of ITER systems' RH code of practice [93], but with stricter final-position tolerances based on the needs of the mirror surface (see Table 6.2). A section view of the pins is given in Figure 6.5. The pins are secured to the mirror substrate by an r6/H7 interference fit, avoiding any play. The interference is sufficiently small not to significantly deform the mirror surface and allows the pin to be removed from the substrate in case it gets damaged. The longer pin with spherical cap is inserted into a cylindrical hole in the DSM, restricting two DOF while the shorter, conical pin is inserted in a slotted hole, restricting the rotation around the interface normal direction. The pins are placed as far from each other as possible within the design space of the interface to reduce the tolerance requirement on the pin location.

While moving the substrate into its final position, the pins restrict one DOF after the other, guiding the mirror into place and preventing the system from getting stuck. During insertion the mirror is actuated by the bolt closest to the longer pin, minimising the moment acting on the longer pin. During disassembly, a threaded rod inside the longer pin is used for pushing the mirror interface apart without jamming. The full RH assembly and disassembly sequence, from docking the mirror to the DSM

Table 6.3: Tolerances on the pins in the DSM and resulting position accuracy of the mirror substrate for a pin distance of 160 mm and pin diameter of 12 mm.

Tolerance $R_x$	M2: $\pm 1.75$ ; M6: $\pm 0.87$	[mrad]
Tolerances on pin and hole in DSM	$\varnothing 12$ h5; $\varnothing 12$ H6	[mm]
Play on pins in DSM	0 to 19	[ $\mu\text{m}$ ]
DSM measurement accuracy	$\pm 10$	[ $\mu\text{m}$ ]
Mirror substrate manufacturing tolerance	$\pm 30$	[ $\mu\text{m}$ ]
Maximum pin axis position deviation	59	[ $\mu\text{m}$ ]
Maximum resulting angular deviation	$\pm 0.74$	[mrad]

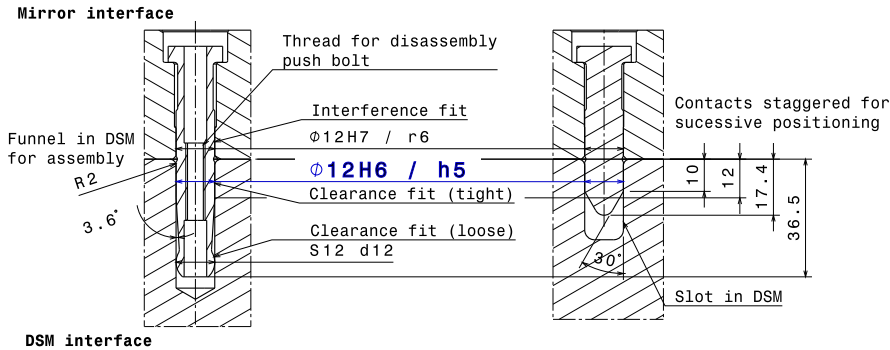


Figure 6.5: Features, dimensions and tolerances of the brass positioning pins in the substrate and DSM.

to complete removal is discussed in Section 6.2.4.

The base design of the mirror does not include the use of a shim between mirror substrate and DSM for the most direct thermal contact at the interface and to keep the number of contacts minimal for highest stability. This approach requires early knowledge of the as-manufactured geometry of the DSM side mirror interface position measurement, since final machining of the mirror interface ranges from problematic to impossible after coating of the mirror due to cleanliness requirements and the risk of damaging the coating. Accordingly, if the DSM cannot be measured before the mirror final machining is required, balancing of the DSM manufacturing tolerances is not possible by the mirror substrate dimensions. In this case, a shim in between the mirror and the interface can provide the capability of aligning two mirror rotations,  $R_y$  and  $R_z$ , as well as movement perpendicular to the mirror interface (Z-direction). The other degrees of freedom are governed by the pins' locations and cannot be influenced, which has to be taken into account in the optical tolerances. Figure 6.6

shows a possible design with shim.

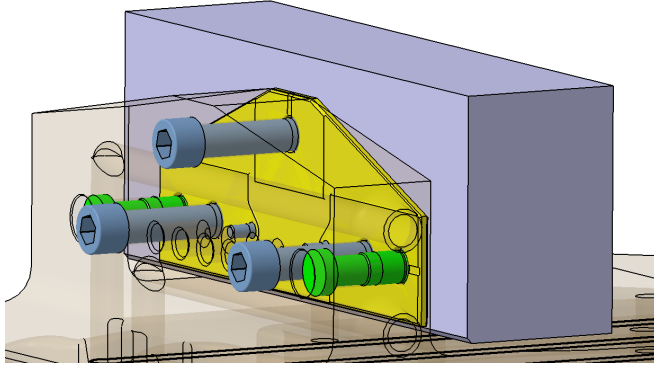


Figure 6.6: Mirror interface with shim (yellow). The shim is bolted to the mirror, and the mounting pads with vacuum venting are moved to the shim as structure with the best manufacturing possibilities.

### 6.2.3 Mirror thermal control

The base mirror design includes the possibility of active heating and cooling by an internal fluid flow. For the secondary mirrors, active cooling is not required to prevent overheating by radiation during operation. Heating of the mirror –  $0.015 \text{ W cm}^{-3}$  in the case of the second and third mirror, and even lower for the mirrors further from the plasma – is not significant enough to exceed any critical temperatures within the plasma operation times of ITER. For mirror locations closer to the plasma, e.g. in case of changes in the system layout, the heating can still get significant for the mirrors with up to about  $1 \text{ W cm}^{-3}$  at the diagnostic first wall.

Instead, the fluid channel was included to address two other concerns: The original specification of the ITER tokamak cooling water system (TCWS) specified a temperature switch between  $70^\circ$  during plasma operation and  $100^\circ \text{C}$  in between shots to combat tritium accumulation in the machine [26]. With the active possibility to control the temperature of the substrate, thermal instabilities from the mounting are controlled. This thermal instability of the in-vessel components' cooling water system was later removed, leaving the water at a relatively constant  $70 \pm 5^\circ \text{C}$  during and in between plasma operation [27].

The second reason for including the fluid channel lies in active heating during vacuum bake-out to combat degradation from condensation, as discussed in Section 3.6. In case it can be shown that the permanent degradation by condensation is not a significant danger, the mirror fluid channel should not be included as it represents a considerable increase in complexity for manufacturing and maintenance operations. It also decreases overall reliability of the system with the possibility of vacuum leaks at the supply pipes.

The design of the fluid channel foresees a constant wall thickness on the front and rear of the mirror to minimize bending of the substrate from temperature gradients

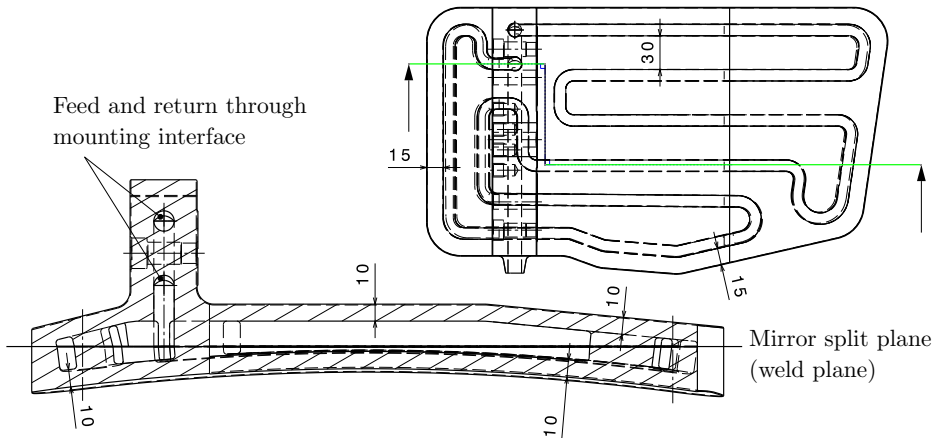


Figure 6.7: Routing of the cooling channel inside the mirror substrate. All dimensions in mm.

in the material. A cut through the channel is shown in Figure 6.7. The channel is routed around the mirror substrate with approximately equal material distribution over the irregularly shaped extent of the mirror. Feed and return are located in the mounting interface and the supply pipes are connected at the edge of the interface, where design space in the UPP is available to connect them. The channel is created by welding together two mirror halves with the channels already milled in a previous step. A weld on the whole split surface is required to prevent warping of the mirror surface from the fluid pressure.

As fluid, the design foresees using the water as provided by the TCWS but with the mirrors connected to a separate circuit parallel to the main cooling circuit in order to achieve the desired temperature control by a valve, able to stop the water flow when necessary to keep the mirror temperature constant. The elevated temperature during vacuum bake-out, especially during the heat-up, is achieved with the shorter heat conduction distance from the cooling channel to the mirror surface, in contrast to the thicker-walled DSM surrounding the mirror, allowing a faster temperature reaction of the mirrors than the surroundings, without the need for an additional heating system.

## 6.2.4 Remote handling mirror exchange

Due to the weight of the mirror assembly of 29 kg, it is not possible to place the mirror with only the remote manipulator as present in the ITER hot cells (capacity of manipulator approx. 15 kg). Mounting of the mirror by RH is split into three phases of manipulating the mirror assembly. In the first step, a hoisting tool with the mirror inside is positioned to the DSM by crane and manipulator arm (see Figure 6.8). The mirror with a temporary support frame is transported towards the mirror mountain interface by the hoisting tool on rails built into the DSM. A full description of this procedure from start to finish, including a digital mock-up and time estimates, can be found in [14].

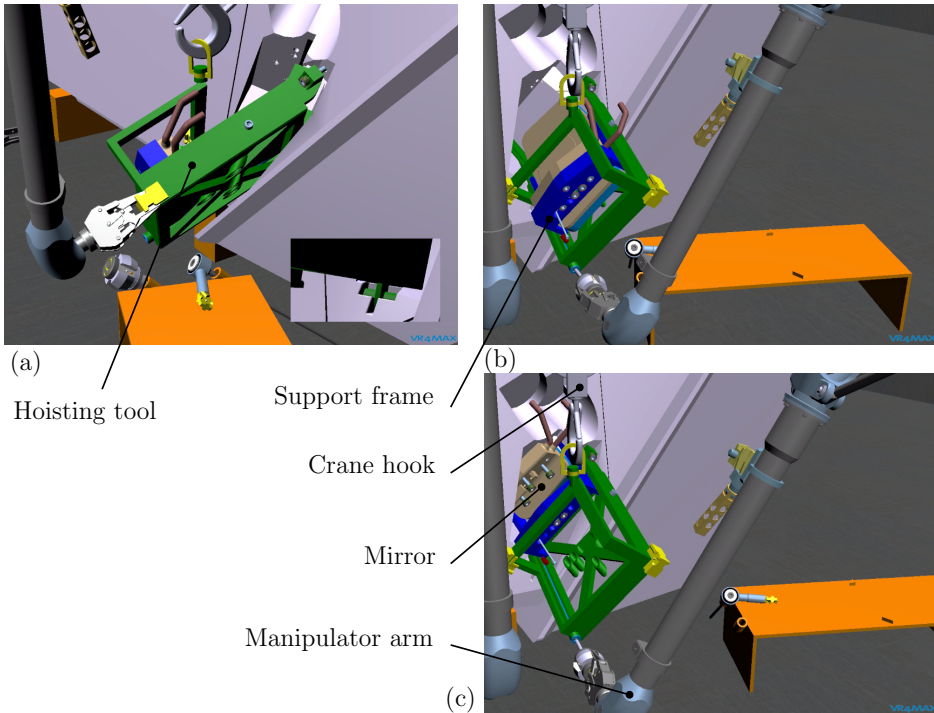


Figure 6.8: Digital mock-up of RH mounting of the mirror. (a) Positioning the mirror inside the hoisting tool to the DSM. (b) Moving the mirror into the DSM on rails. (c) Retracting of the frame after engaging the mirror mounting bolts. [14].

In the second phase, the mirror is handed from the hoisting tool to the DSM by partially engaging the three bolts of the mirror interface. The mirror is now in rough positioning and alignment, suspended on the bolts shafts and the loose fitting sphere of the longer pin is engaged.

In the third phase, the mirror is moved into its final position by engaging only the bolt closest to the longer pin with the cylindrical fit in the DSM. This fit is the first of the final positioning contacts to engage. The close vicinity of the bolt engaging the contact to the tight fit prevents canting and jamming. When the second pin gets to the point of the tight fit, the mirror is already aligned to the interface. Once the first bolt is fully engaged, the additional bolts are tightened to nominal torque.

For dis-assembly of the mirror, the hoisting tool is attached to the mounted mirror first. After disengaging the main bolts, a thread inside the longer pin allows pushing the mirror out of the DSM from the tight fit of the interface. The pin itself is secured against pushing out of the mirror substrate by a short threaded insert on top of the bolt. The remaining steps are the same as for the assembly. The procedures of final positioning and ejection are shown in Figure 6.9.

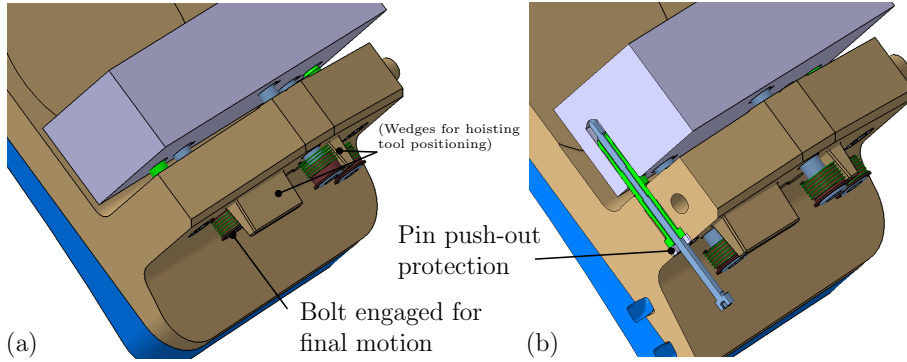


Figure 6.9: (a) Moving the mirror into final position by the bolt at the longer pin. (b) Disassembly by push rod.

### 6.3 Design of two-axis adjustable mirror

The fourth mirror of core CXRS is chosen as an adjustable mirror for assembly-time internal alignment of the mirror chain. It is the preferable mirror for adjustment on several accounts: First and foremost, as a flat mirror close to an intermediate image, the negative impact on the optical imaging quality is limited and the mirror is relatively small. In addition, it is far enough from the plasma not to receive significant heating by radiation ( $<1 \times 10^{-3} \text{ W cm}^{-3}$ ) and EM forces are reduced with the smaller magnetic transients further from the plasma. Additional details on Mirror 4 are given in Table 6.4.

Table 6.4: Details of Mirror 4 for the ITER core CXRS ‘large M1’ optical layout.

Size	280 mm*200 mm
Adjustment DOF	$R_x$ ; $R_y$ (tip, tilt)
Alignment step width	0.15 mrad
Alignment range	$R_x$ : $\pm 10$ mrad, $R_y$ : $\pm 10$ mrad
EM forces <sup>‡</sup>	$M_x=1.3$ kN m, $M_y=8.5$ kN m, $M_z=0.7$ kN m [76]
Radiation heating (mean)	$4.2 \times 10^{-4} \text{ W cm}^{-3}$ [83]

In accordance with the discussion in Chapter 5, only assembly and maintenance time alignment is foreseen. For alignment, the fourth mirror tip and tilt are adjusted with the goal of internal alignment of the mirror train in the UPP.

As alignment mechanism, a layout based on shims is proposed for adjustment of the two rotations (see Figure 6.10). The required shim thickness stepping for the shims is  $19 \mu\text{m}$ , with the distance between pins of 127 mm as realised.

A design with flexures was also created, but the loads on the flexures were calculated as borderline feasible despite the limited loads from thermal and mechanical

<sup>‡</sup>For 316L(N)-IG substrate material and upwards VDE 36 ms

effects on M4 and while limiting the adjustment range to the exact range required. Compared to a design with flexures, the rigidity and small footprint achieved with the shimmed solution are seen as preferable for M4. In addition, with alignment by shims, the remote handling equipment is not required to provide exact movements beyond positioning of the shims – e.g. turning of a bolt by precisely  $5^\circ$ .

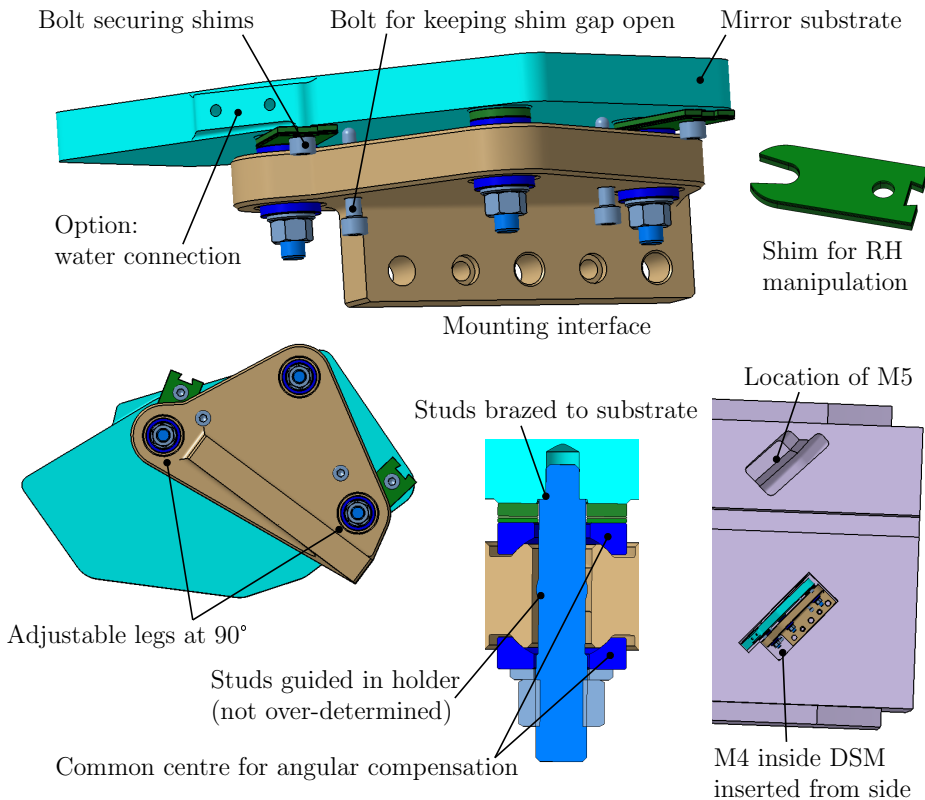


Figure 6.10: M4 design allowing adjustment with shims.

The proposed design of M4 is kept close to the fixed mirror design, allowing the use of the same procedures for maintenance and mounting. The three mounting pins are welded to the mirror substrate. To avoid the weld distortion on the mirror surface and remove weld stresses, heat treatment of the mirror after welding and before grinding the optical surface is required. The mounting pins are secured to the holding bracket in a quasi-kinematic set-up to prevent alignment from inducing strong forces into the substrate. No differential thermal expansion compensation is foreseen in the alignment interface.

Exchanging of the two shim stacks for angular alignment is possible with the mirror mounted in the DSM. Especially for adjustment by remote handling, the design includes two small bolts to push the shim gap open for insertion of the shims. Once the shims are inserted, the three main bolts are tightened slightly to check alignment

of the optical system. Changes in adjustment while tightening the bolts to nominal force are expected only significantly below the shim step width of  $19\ \mu\text{m}$ . For each stack of shims, a bolt is included for securing the shims against loss after alignment.

## 6.4 Thermo-mechanical simulation of Mirror 2

With the choice of a metallic substrate material, and especially when looking at the poor thermo-mechanical properties of 316L(N) stainless steel, an investigation of the optical position and shape requirements is critical. Thermo-mechanical FEM simulations were created in ANSYS [4] to check the impact of forces and thermal influences with an emphasis on the mirror surface deformation and shifts. The simulation is done for M2 as the larger non-flat mirror among the secondary mirrors close to the plasma. The simulation includes the mirror substrate, the interface elements and a small part of the DSM (see Figure 6.11). The thermal and mechanical influences are simulated in series. All directions in this chapter are given in the mirror's local coordinate system with Z perpendicular on the mirror surface at the central ray intersection and Y aligned along the projected DNB aiming line.

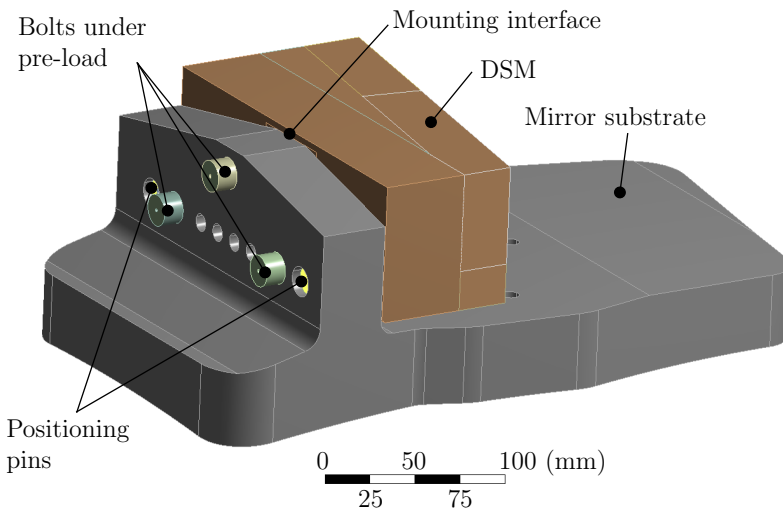


Figure 6.11: Extent of the model used in the simulation of the second mirror. The mirror is mounted to the DSM via contacts and bolt pretension.

The plasma scenario used in the simulation is the inductive scenario DINA-2010-01 with 15 MA plasma current and 500 MW fusion power over a 410 s flat-top phase [33]. This plasma scenario has been found to exhibit all thermal and mechanical effects visible in the other ITER scenarios.

For the ITER UPP thermal environment, the following thermal environments are looked at:

1. Heat-up to vacuum bake-out temperature of  $240\ ^\circ\text{C}$  and cool-down to operational temperature of  $70\ ^\circ\text{C}$

2. Operation with a feed water temperature switch from 100 °C to 70 °C during the plasma shot and back during dwell time, as specified by the ITER documentation initially [26], the specification the design was created for. The change in temperature is modelled as a ramp during the 160 s before and after the plasma shot
3. Stable TCWS (Tokamak Cooling Water System) water temperature, as defined in a newer release of the ITER cooling water documentation [27]:  $70 \pm 5$  °C. The temperature was assumed to undergo one to four fluctuation cycles of  $\pm 5$  ° per 400 s shot

Two cases for the mirror substrate are included: a substrate with internal water flow and a thermally inertial substrate with no internal fluid flow. The inertial substrate is representative also for a substrate with temporarily halted water flow. As substrate materials, 316L(N)-IG stainless steel and CuAl10Ni5Fe4 are simulated.

### 6.4.1 FEM model and boundary conditions

The FEM model consists of 130k elements (243k nodes) with a predominantly quadratic tetra mesh with hexagons where the geometry allowed for it while avoiding pyramids (see Figure 6.12). The mesh of the mirror substrate and especially the mirror surface is of higher density than necessary for the thermal and general mechanical results to allow determination of the mirror surface shape deviations. An overview on the boundary conditions is given in Table 6.5. Figure 6.13 depicts the position where the boundary conditions are applied.

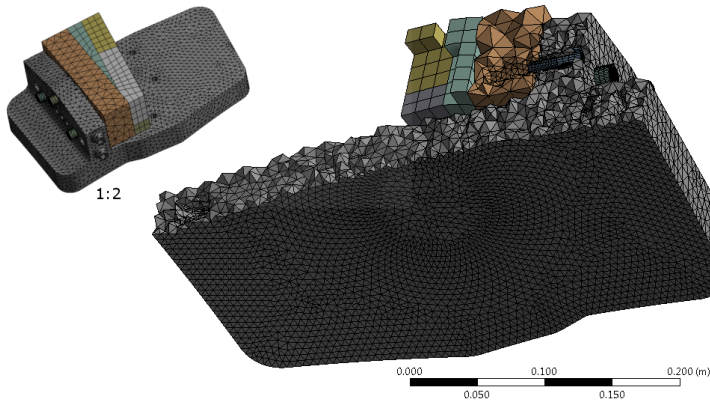


Figure 6.12: Mesh of the M2 FEM model with internal cooling channel.

In the thermal simulation, a slice of the DSM is included with a convective heat load applied, representing the water cooling in the DSM (see boundary condition "E" of Figure 6.13 (a)). The location of this load is sufficiently far from the interface to allow for the placement of bolts and pins, but also close enough to represent a worst-case situation for cooling water temperature-induced instabilities of the DSM.

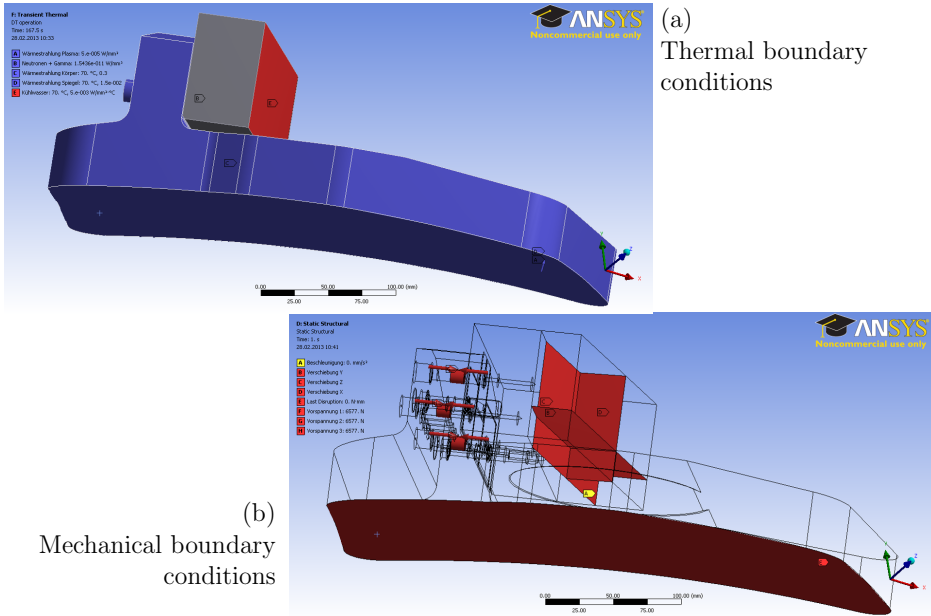


Figure 6.13: Placement of the thermal and mechanical boundary conditions (without fluid channels).

During mechanical simulation, the DSM is set to a constant 70 °C (respectively, 85 °C for the 30 °C instability case). The fixed DSM temperature removes the influence of the DSM temperature distribution, which is only sufficiently accurate to simulate the thermal contact behaviour, on the mirror tolerance simulation. In the mechanical simulation, the temperature distribution would result in non-physical deformations in conjunction with the mechanical constraints present at the mirror interface.

A coarse CFD analysis of the water flow in the channel has been created to check for extended areas of stagnant or circulating flow. The channel layout was found not to exhibit such areas. In the further simulations, a convection coefficient of 5 kW m<sup>-2</sup> K<sup>-1</sup> was applied as the boundary for the 0.34 kg s<sup>-1</sup> water flow assumed in the mirror. At 5 kW m<sup>-2</sup> K<sup>-1</sup>, the temperature distribution is not limited by the heat transfer to the water or temperature change of the water, but by the heat conduction in the material outside of the several seconds after sudden changes in feed-water temperature.

The small heat flux from the plasma to the mirror surface of 50 W m<sup>-2</sup> absorbed energy is a result of the already well-protected location of the second mirror: ITER specifies the heat load from the plasma as  $\dot{q}_{CX}=0.25$  MW m<sup>-2</sup> for the charge exchange (CX) atoms and  $\dot{q}_r=0.11$  MW m<sup>-2</sup> for the maximum average heat radiation [89]. For the CX atoms, the heat load deposited on M2 is only 20 W m<sup>-2</sup> [46]. The upper bound for the mirror-radiative heat load from the plasma is estimate as follows:

$$\frac{\dot{q}_r A_{\text{aperture}} \Omega_{\text{plasma to M2}}}{2\pi A_{M2}} R_{M1} (1 - R_{M2}) = 10.3 \text{ W m}^{-2} \quad (6.4.1)$$

with  $A_{\text{component}}$  as the area of the respective components (aperture: 0.005 876 m<sup>2</sup>, M2:

Table 6.5: Overview on loads and boundary conditions for the M2 thermomechanical simulation. The letters in italics refer to the locations marked in Figure 6.13

Thermal boundary conditions	
Convection (mirror & DSM)	$5 \text{ kW m}^{-2} \text{ K}^{-1}$ ( <i>E</i> )
Thermal radiation	$\epsilon=0.3$ for 316L(N)-IG to self and stainless steel environment at water temperature ( <i>C, D</i> )
Surface heating from plasma	$50 \text{ W m}^{-2}$ ( <i>A</i> )
Neutron and gamma heating	Uniform heating of $1.54 \times 10^{-2} \text{ W cm}^{-3}$ ( <i>B</i> )
Contact conductance	$3.5 \text{ kW m}^{-2} \text{ K}^{-1}$ to $60 \text{ kW m}^{-2} \text{ K}^{-1}$ depending on interface pre-load and material combination.
Mechanical boundary conditions	
Bolt pre-load	$12.7 \text{ kN}$ (M12 bolts) ( <i>F, G, H</i> )
Interference fit at pins	$19.5 \mu\text{m}$ at $\mu=0.2$
EM force (VDE)	$108.6 \text{ N m}$ for 316L(N)-IG), scaled by el. conductivity for CuAl ( <i>E</i> ) (Simulation A. Panin)
Water pressure	$4.4 \text{ MPa}$
Earth quake	$\pm 2.6 \text{ g}$ (as combination of 3 vectors) ( <i>A</i> )
Other	Gravity ( <i>A</i> ), DSM position ( <i>B, C, D</i> )

$0.077422 \text{ m}^2$ ),  $\Omega_{plasma\ to\ M2}=0.0486 \text{ sr}$  as the solid angle of the plasma to the second mirror and reflectivity  $R_M=80\%$  of the mirrors (rhodium is assumed for both). The indirect radiation via reflection from the anti-reflection-coated duct walls is assessed as twice the direct heat load. The estimate represents a worst case with the maximum mean last plasma surface heat load applied at the 100 mm recessed duct aperture, with the shutter of the diagnostic system always open. In addition, it assumes that the radiation has a uniform angular distribution, even though, in reality, the maximum originates from the divertor and cannot directly shine into the optical duct.

The mean volumetric heating by radiation of  $0.0154 \text{ W cm}^{-3}$  is taken from an MCNP calculation with a simplified mirror body [83]. Application of the spatially resolved volumetric heating from an MCNP brick mesh of 20 mm resolution was realised (see Figure 6.14(a)). This interpolation of the heat only included bricks with a centroid inside the MCNP mirror body to avoid the application misleading heat values. These are present in the brick mesh tally as the heating was calculated by MCNP with 100% substrate material fill rate based on the actual, local radiation flux which has significantly increased values in the vacuum next to the mirror body from streaming effects. Interpolation of the brick mesh to the MCNP body gave a mean heating 12% higher than the MCNP-calculated mirror substrate volume integrated value as a result of incomplete filtering.

From the filtered results, extrapolation of up to 80 mm was required where the MCNP body did not overlap with the actual mirror geometry, a distance where the assumption of an unchanged radiation field needs to be questioned. Figure 6.14(b) shows the result of the interpolation. With the low absolute value of heating and

the limited gradient over the mirror, no significant impact of the spatially resolved heating on the optical surface was found as compared to the application of a mean heating value. All results given in this work are calculated with the MCNP-calculated mean heating for the simplified mirror body.

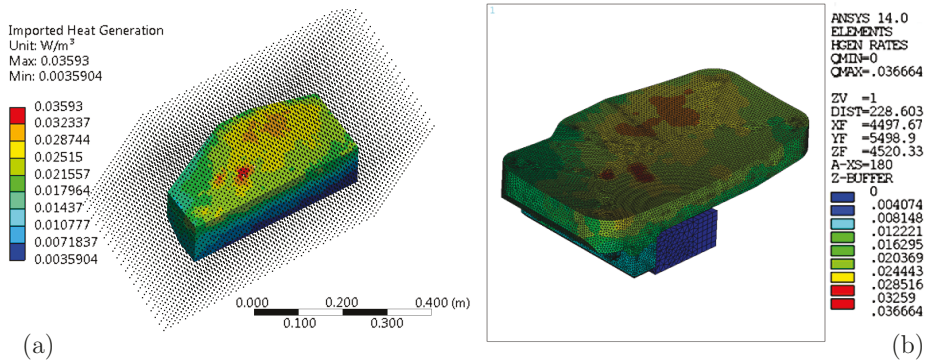


Figure 6.14: Application of MCNP brick mesh locally resolved volumetric heating. (a) Unfiltered MCNP brick mesh and MCNP mirror body. (b) Inter- and extrapolated heating as applied to mirror body.

The heat contact conductance in vacuum is based on interface pre-load and material combination. The heat transfer is included as mean value with no spatial distribution. The values are taken from [90][15] and [45]. The main interface in the 316L(N) mirror substrate material case is calculated as  $3.5 \text{ kW m}^{-2}$ , and  $4 \text{ kW m}^{-2}$  for the CuAl10Ni5Fe4 substrate.

The DSM is held in place by three support constraints on orthogonal surfaces: *B*, *C* and *D* in Figure 6.13(b). The constraints allow node rotation and in-plane movement but no out-of plane node shifts, achieving free expansion of the DSM with uniform temperature distribution while avoiding creation of non-physical forces and deformations. The constraints represent a stiff DSM as present in the diagnostic system. The location of no DSM movement where the three constraint planes meet is placed behind the mirror centre to suppress shifting of the substrate by thermal expansion of the DSM in the mirror's X and Y directions. This approach is preferable as the optical fixed reference for the tolerances of the mirror is not the mounting interface but the mirror optical centre. The remaining shift in Z-direction by the thermal expansion is not significant to the  $\pm 2 \text{ mm}$  tolerance of the mirror, governed by motion of the DSM, which is not covered by this simulation.

The bolt pre-load is calculated based on the Structural Design Criteria for ITER In-vessel Components [6]. The bolts are dimensioned for a maximum temperature of  $250^\circ\text{C}$  with the limiting criteria being the yield strength  $S_y$  with  $2/3 * S_{y,min}(250^\circ\text{C}) = 90 \text{ N mm}^{-2}$ . The bolt is pre-loaded to 90% the allowable stress at the  $250^\circ\text{C}$ , and within the  $60 \text{ Nm}$  allowed torque for the ITER RH equipment of M12 bolts [93]. The resulting pre-load of the bolts is  $6577 \text{ N}$ .

### 6.4.2 Temperature progression and distribution

The temperature during operation does not reach material limits in any of the feasible operational scenarios (Substrate with or without internal channel, TCWS feed temperature constant or changing). For the (impossible) worst case assumption of steady-state full-power plasma operation with a 316L(N)-IG substrate cooled by conduction to the DSM and thermal radiation, the peak temperature is limited to 112 °C.

Figure 6.15 shows the temperature distribution 336 s into the flat-top phase of a simulated D-T burn cycle (fourth cycle is a row, exhibiting near quasi steady-state behaviour) for substrates with and without internal channels and water feed temperature at  $70\pm 5$  °C. The 336 s coincide with a 75 °C maximum of the assumed feed-water temperature instability. With a CuAl10Ni5Fe4 substrate, similar gradients with smaller amplitudes are found.

The temperature gradient in the DSM is approximately uniform in perpendicular direction to the mounting interface, owing to the way the convection is applied to the lower surface in the DSM. A statement on the impact of a temperature gradient in the DSM along the interface and its impact on the mirror tolerances is not possible with the model. The maximum temperature spread at the interface was found to be  $\Delta T=5$  °C.

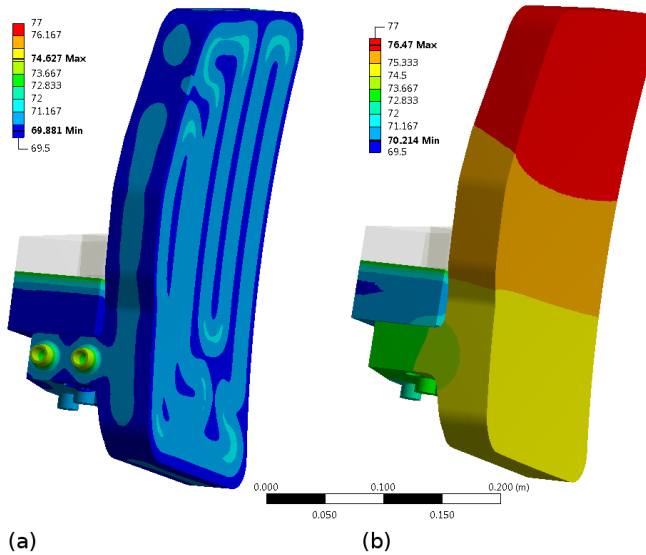


Figure 6.15: Temperature distribution for the  $70\pm 5$  °C feed-water temperature thermal transient simulation 336 s into the flat-top phase. (a) Internally cooled mirror. (b) Bulk substrate. Both substrates from 316L(N)-IG.

In the internally water-cooled case 6.15(a), the mirror surface temperature is dominated by the temperature gradients from to the water temperature instability in the fluid channel. The DSM has no significant thermal impact on the mirror substrate.

The temperature gradients in the substrate are oriented towards the cooling channels with similar magnitude on the front and rear side as desired.

In the inertial temperature case 6.15(b), the substrate exhibits a large temperature gradient towards the cooled mounting interface. At the interface itself, the temperature gradient slightly deviates from perpendicular to the interface and is anticipated to cause tilting of the mirror substrate. Based on the one-sided cooling by the DSM, the gradient has been anticipated but could not be avoided. While  $\Delta T_{max}$  is higher than for the internally cooled case, the thermal gradients are not as steep and might allow higher overall optical stability.

The suitability of the thermal situation is thus given with respect for the materials as chosen. The suitability for the optical system cannot be decided based on the temperature result alone.

### 6.4.3 Mechanical stresses

The first, non-damped eigenmode of the mirror system with the pre-loaded bolted interface is calculated at 87 Hz (tilt around the interface) and deemed sufficiently high above the main frequencies of the ITER design earthquake with up to 25 Hz, allowing the use of the simplified linear static calculation of the earthquake-related acceleration without dampening.

To avoid convergence problems from plastic deformation at the interference fit of the pins in combination with the multiple frictional contacts in the assembly, a fully elastic material behaviour was assumed for the main simulations and the interference was set to 19.5  $\mu\text{m}$ . Outside the immediate influence zone of the interference fit with non-physical stresses beyond the tensile strength of 316L(N)-IG at 525 MPa, this assumption was found to produce reasonable results with a slight increase of the deviations on the mirror surface. Figure 6.16 shows the resulting distribution of stresses in the mounting bracket and the substrate volume with mirror surface.

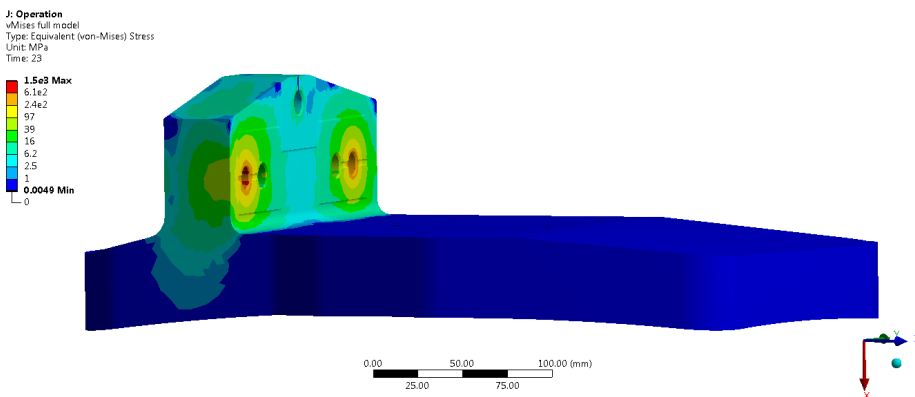


Figure 6.16: Von Mises operational stress for the mirror substrate with mounting bracket during operation with elastic material model. Note: Scale is shifted and logarithmic above 1 MPa.

Table 6.6: Tolerances taken into account in the preliminary design of core CXRS second, toroidally shaped mirror. The distance  $l$  of the location to the mirror optical centre is normalised to one for the furthest point from the optical centre.

Rigid body shift	X / Y (decenter) and Z (piston)
Rigid body rotation	X / Y (tilt) and Z (spin)
Surface deformations	Focus (as the paraboloid $Z_2^0 = 2l^2 - 1$ ), $0 \leq l \leq 1$

Operational and off normal stresses, including the earth-quake and EM-loads, do not result in critical stresses for any of the components. Within the portion of the substrate bearing the mirror surface, the highest load is found at the edges of the internal cooling channel, where up to 20 MPa are predicted, arising from the internal pressure and temperature gradients due to the feed-water thermal ripple. The higher stresses in the mounting bracket from bolt pre-load and the interference fit of the positioning pins do reach into the volume bearing the mirror surface but are stable over time during operation.

With only materials of similar thermal expansion, the bolt pre-load is constant from room temperature to maximum bake-out temperature. The 316L(N)-IG substrate with internal cooling exhibits constant maximum principal stress in the bolt shaft within  $\pm 4\%$  of the initial pre-load for the operational thermal field, electromagnetic forces and design earthquake. A shock load of 25 g (vertically downwards for a port plug in horizontal orientation) leads to a maximum principal stress in the bolt shaft of 107.5 MPa, below the allowable material limit of 146 MPa at 20 °C.

Shifting of the mirror within the play of the pins is possible if the friction in mounting interface is overcome. This shifting of the mirror has to be avoided after alignment of the mirror chain. The FEM model shows stable pre-load in the interface, sufficient to counteract external loads during all times with a friction coefficient of 0.2. The unavoidable local shifts due to the temperature gradients over the interface were estimated by hand to be compatible with the mirror tolerances and are not expected to result in a gradual change in alignment with repeated thermal cycling of the mirror.

As conclusion of the mechanical simulation, the stresses encountered in the mirror during operation and vacuum bake-out are within limits of the materials used in the design. Loss of the mirror position and damage to components over time was not found. The suitability for the optical system is discussed in the next section.

#### 6.4.4 Mirror surface shape

The impact of a deformation on the optical imaging quality does not scale linearly with the value of the FEM-calculated node shift on the substrate surface. To judge the suitability of the mirror design, the displaced nodes of the mirror surface nodes are fitted against the movements and deformations given in table 6.6. The fitting is achieved as least-squares fitting in two steps: Rigid body motion and surface aberrations. The detailed approach of calculating the optical shape deviations for the tolerancing used in this work is discussed in Appendix A.

In the following, ‘irregularity’ is taken as the remainder of the surface deviations after subtraction of all shifts and deviations, as given in Table 6.6. For CXRS-core,

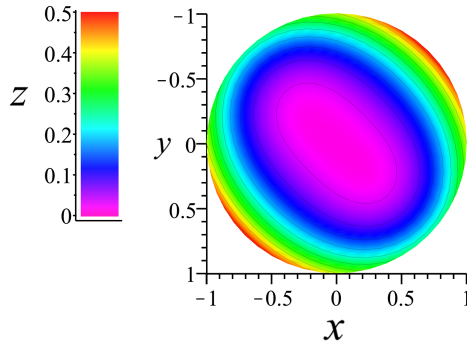


Figure 6.17: Shape of the ‘TIRR’ aberration as used in ZEMAX with the astigmatism shown at  $45^\circ$  for a normalised, circular mirror.

where the required imaging quality is limited, low-frequency residual deviations can be compared directly with the TIRR tolerance of ZEMAX (half-spherical aberration defocus, half astigmatism) [98], as used in the tolerance calculation with one peak and valley on the surface (See Figure 6.17). For situations with multiple ripples on the surface – e.g. as caused by cooling channels – comparing only the peak-to-valley value of the irregularity to TIRR does not allow a definite answer on the suitability of the mirror surface but a full ray-trace with the deformed surface is required.

The tolerances on movement in X, Y, Z and rotation around Z are not included in this discussion. For rotation around Z, the tolerance is not at all critical and can be fulfilled in any case. For movement in X, Y, Z, the thermal expansion of the DSM is the main cause, but not included in the simulation envelope. Because the tolerance values given as input to the optical design were based on the well-known shift by the DSM from thermal expansion, and the additional shifts calculated in the model are three orders of magnitude below the tolerance value, the mirror tolerances on shift are known to be satisfied.

In the results plots, jumps are visible at 1640 s and between points at 0 s and 1800 s. These differences are at times where the thermal cycle in the simulation would have repeated but the model did not reach full thermal quasi-steady state (the thermal result of the second, respectively fourth for the inertial geometry, plasma shot was used to calculate the mechanical result). Partial checks on the aberrations of earlier and later cycles approaching quasi-steady state show no difference in the conclusions as given.

For the mechanical simulations, the time resolution between 0 s and 700 s is chosen to be higher, as the plasma discharge with the measurements is located within this period. The progression of deviations during the dwell time is only indicative and may not include all peaks.

Figure 6.18 shows the deviations for rotation around X and Y during a plasma cycle. The rotation around X undergoes higher deviations, caused by the rigid mounting interface being oriented along Y within  $9^\circ$ : The mounting interface acts as a hinge around Y. The constant positive rotation around X for all calculated cases is caused by the interference fit of the positioning pins: The interference area on pin is not

centred in the interface but closer to the DSM side. The rotation is larger for the CuAl10Ni5Fe4 substrate than the 316L(N)-IG substrate, in line with the reduced Young's modulus. Because it is a stable influence over time and temperature, it can be counteracted by the assembly-time internal alignment of the optical system.

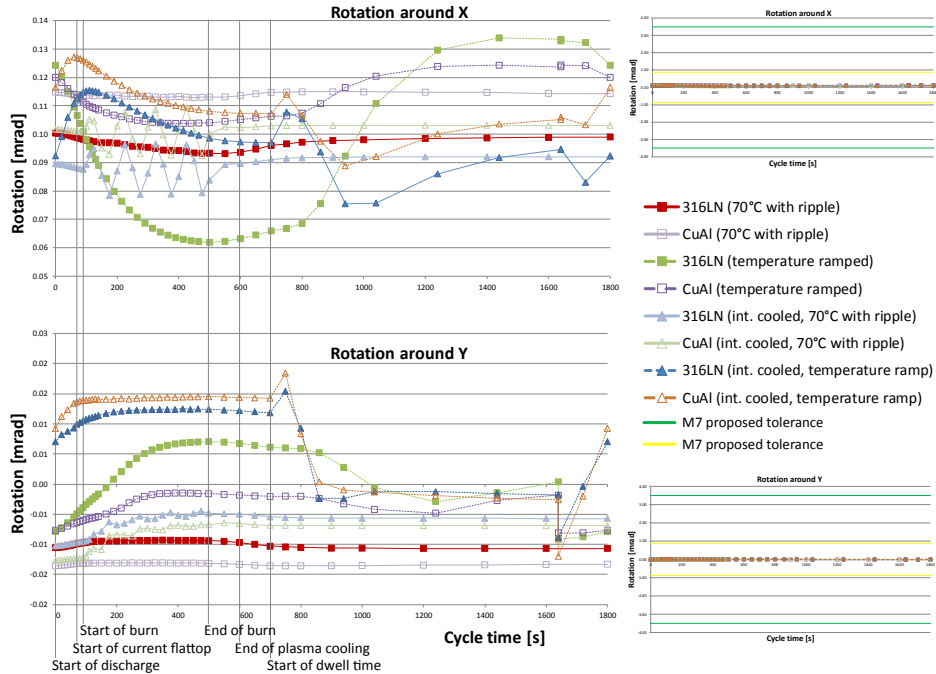


Figure 6.18: Tip/Tilt deviations as calculated for the mirror. The deviations are well within limits in all cases. Green/yellow lines: Tolerances of M2 and M7.

For all simulated cases, deviations on rotation around X and Y are within tolerance for M2 by a factor of at least 10. Even for the tighter tolerances of M7, the design stays within a factor of three of the requirement with the higher loads of M2. Avoidance of an externally imposed 30°C temperature ramp is clearly beneficial in all cases. With the 30°C temperature instability, avoiding water flow in the mirror leads to a slower but longer-lasting gradual change in angular orientation, which is beneficial for tracking the DNB image location shift. The temperature instability in the cooled DSM only has a minor influence.

While gradual differences are predicted between the 316L(N)-IG stainless steel and CuAl10Ni5Fe4 as substrate material, both react in the same way for rotation around X and Y. As expected with the material values, the CuAl10Ni5Fe4 material reacts faster to temperature changes and exhibits slightly less deviations in all thermal cases.

The current ITER TCWS base case of 70°C with temperature instability up to  $\pm 5^\circ$  thermal case shows higher stability with no internal cooling. With internal cooling, any instability in the feed water temperature leads to rotation of the mirror. In contrast, with temperature instability of 30°C, the angular stability, though not nec-

essarily absolute deviation, is better for the internally cooled mirror. Here, the shot time is sufficiently long to create significant thermal gradients in the mirror mount.

Spherical aberration (see Figure 6.19 on top) increases in radius with higher temperature, caused by the thermal expansion. As the distance between optical elements is also increased with the thermal expansion of the connecting structure, a certain increase in focal length is desired (passive athermalization). In the plot, the nominal change in spherical aberration desired at 70 °C (0.0148 mm peak-to-valley for the M2 mirror size) is already subtracted from the calculated aberration. For the thermal cases with the 30 °C thermal instability, taking a constant value does not fully compensate for the desired spherical aberration. A temperature-correlated correction was not applied as the full temperature behaviour of the DSM was not known and no measurements are planned during dwell time where the largest discrepancy is encountered.

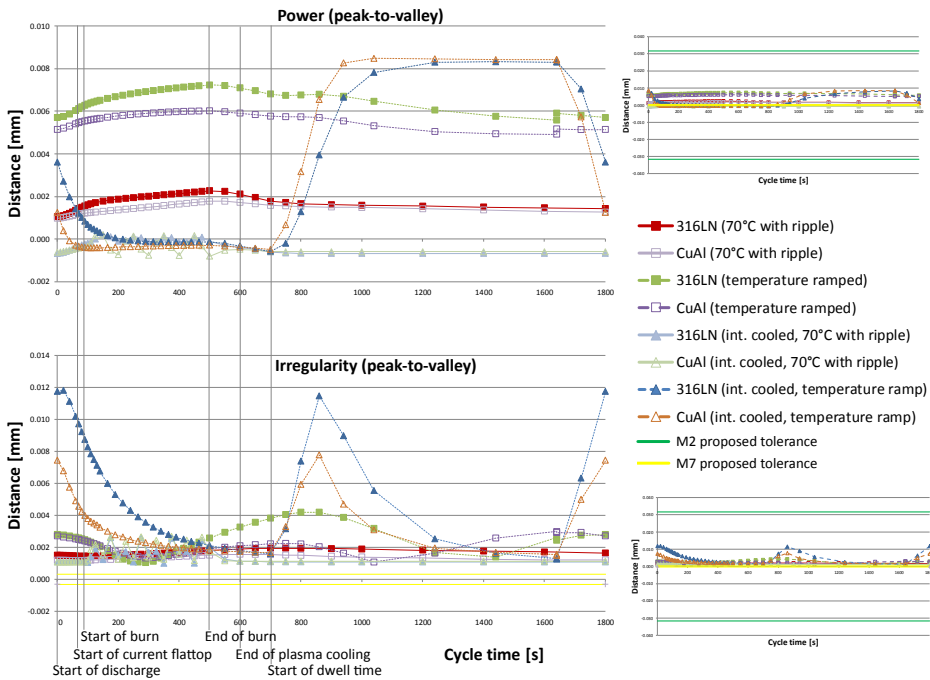


Figure 6.19: Change in power (spherical aberration) and remaining surface irregularity after subtraction of the movements, rotations and change in power as peak-to-valley value. Green/yellow lines: Tolerances of M2 and M7.

All calculated deformations are within the tolerance for M2, but under the worst case assumption of identical thermal loads, the tolerance for M7 would not be met. Again, the difference between materials is visible, but the reaction is similar as with the rotations. For the  $70 \pm 5$  °C feed-water temperature, the ripple on curvature is visible for the substrates with internal water flow, but well within the tolerance range. In case of a 30 °C switch-over in feed water temperature, the more stable behaviour is

exhibited for the inertial mirror. While the focal length does not reach the nominal value and shows a gradient over the whole shot, the instability is reduced, especially for short pulses as anticipated at the start of ITER.

As shown in Figure 6.19 (bottom), the tolerance on M2 irregularity is met in all simulations for the peak-to-valley distance with a significant advantage for the uniform nominal 70 °C feed-water temperature. With internal cooling, the shape differs significantly from the ‘TIRR’ shape (see Figure 6.20(a, b)). The plots are given at 325 s in a plasma burn cycle at a peak of the 70 °C±5 °C feed-water temperature instability. The materials in the simulation are (a): 316L(N)-IG and (b): CuAl10Ni5Fe4. (c): Substrate of 316L(N) with no internal cooling. Scales are not unified to emphasize differences in shape. The cooling channels are clearly visible, leading to deviations of a higher frequency than assumed in the tolerance calculation. At the shown frequency and amplitude, the mirror is estimated to be within the given tolerance.

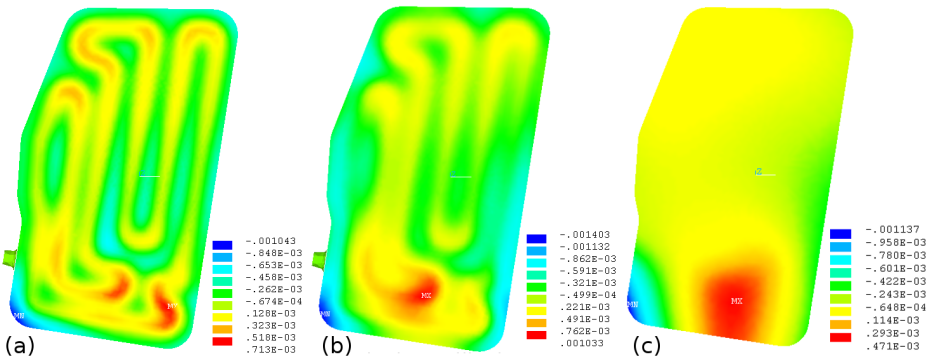


Figure 6.20: Shape of the residual deviations after fitting of movements, rotations and spherical aberration. Scale in [mm].

For the mirror without water flow, irregularity is governed by the temperature change of the mounting interface, deforming the mirror surface. With the shape as given in 6.20(c), the mirror is within the tolerances of M2. The shape of the internally cooled substrate is not changed by the material selection, but CuAl10Ni5Fe4 exhibits a reduced amplitude of the deviations.

### 6.4.5 Conclusion from FEM modelling

Operational loads on the mirrors are well within the thermal and mechanical limits of the materials used in the design. Other events including earth quake and plasma disruptions do not lead to damage of the system or loss of pre-load with the associated possible permanent change in mirror position and orientation.

The preliminary optical tolerances of core CXRS are fulfilled with the proposed design for the mirrors two to five. The mirror position stability and surface shape is improved with no water flow in the substrate during operation in all cases, the temperature increase is not critical. Where a cooling channel is present the water flow should be stopped during operation. The mirror should then be cooled down during dwell time to stabilise its' temperature before each plasma operation cycle,

minimising angular deviations. The decrease in optical quality from the unfavourable material properties of 316L(N)-IG with high thermal expansion coefficient of  $16.5 \text{ K}^{-1}$  and low heat conduction with  $15.48 \text{ W m}^{-1} \text{ K}^{-1}$  at  $100^\circ\text{C}$  is found to be tolerable for core CXRS Mirrors 2 to 5 with to the limited imaging quality requirement of core CXRS.

The shape tolerances for Mirrors 6 and 7 given are critical, even with additional changes in the geometry to decouple the substrate from the supporting structure as proposed in [13]. For these mirrors, the tolerances can be relaxed while limiting the tolerances found to be generous for the front mirrors.

# Chapter 7

## Prototypes and testing

To test the feasibility of central aspects of the proposed design and identify critical issues, three prototypes were created:

- Interface prototype: Testing of the assembly and disassembly procedure taking remote handling restrictions into account
- Mirror substrate prototype: Checking the manufacturing route for the mirror-cooling channel compliant with ITER requirements on welding and leak rate
- Dielectric mirror coating on stainless steel substrate: investigation of the immediate and long-term behaviour of the coating on the non-traditional substrate under ITER conditions

The prototypes are produced from European grade steel of composition and condition close to the special steel used in ITER, the 316 L(N)-ITER Grade (IG). The steel used for the prototypes were bought based on a material certificate to ensure a close fit with the ITER steel, minimising the differences in machining and welding behaviour. Table 7.1 gives the composition of the materials used. 316L(N)-IG could not be obtained.

Steel No.	C	Mn	Si	P	S	Cr	Ni	Mo	N
316 L(N)-IG* [7]	0.03	1.6-2	0.5	0.025	0.01	17-18	12-12.5	2.3-2.7	0.06-0.08
1.4429 (measured)	0.013	1.86	0.28	0.019	0.002	17.18	13.3	2.5	0.158
1.4435 (measured)	0.22	1.9	0.39	0.022	0.018	17.11	13.23	2.54	0.098

Table 7.1: Composition of 316 L(N)-IG and the materials used in testing. All values are given in mass-%.

### 7.1 Interface prototype

The purpose of the interface prototype is to test the high-accuracy final positioning step of the mirror substrate (for a description of the full sequence, see Section 6.2.2).

---

\*Additional limits: Cu 0.3; Co 0.05; Nb 0.01; Ta 0.01; Ti 0.1, single values represent maximum allowable content

At this step, an elevated risk of jamming in a position with complicated recovery exists.

The prototype consists of two blocks of 1.4429 stainless steel representing the DSM and the mirror, two pins for positioning made of the bronze CuAl10Ni5Fe4 and stainless steel M12x70 A4-70 bolts. The bulk of the mirror substrate is represented by a 25 kg lead weight attached to the mirror side of the interface. The initial configuration and set-up at the start of testing with the first threads of the bolts engaged and the spherical pin in contact is shown in Figure 7.1.

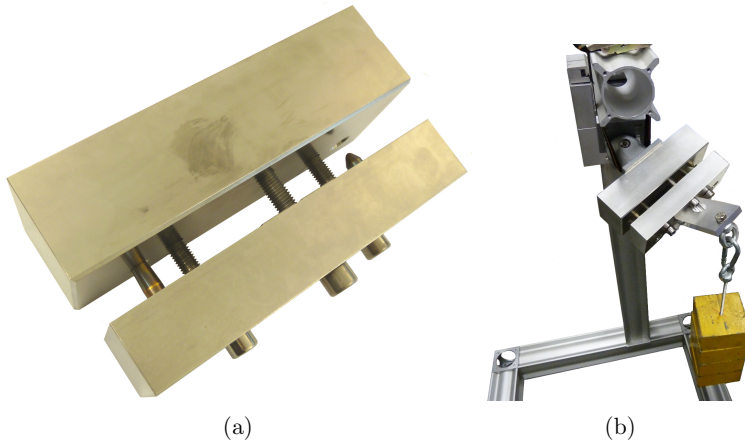


Figure 7.1: Interface prototype. (a) Interface configuration at the start of testing. (b) Experimental set-up with lead weight and orientation of M2 of core CXRS.

The testing procedure includes moving the mirror into its final, precise position and the disassembly sequence up to the moment before the mirror would again be supported by the rails in the shield block.

Testing was performed hands-on but interaction with the test set-up was limited to the interactions and tools available with RH. The interface is engaged only by actuating the bolt close to the longer pin. Once the gap in the interface was closed, all bolts were engaged. Full nominal bolt pre-load was not applied as the rigidity of the test set-up was insufficient. Pushing the mirror out of its tight fit with the DSM is achieved by engaging the threaded rod inside the longer pin. A range of configurations was tested, including lubricated and alkaline pickled pins and bolt shafts as well as different orientations of the interface.

The dimension of the holes and pins were measured before testing and after the first assembly with full weight and orientation of the core CXRS second mirror. The as-measured geometry at the start of testing includes a play of  $7\ \mu\text{m}$  between the nominal diameters for the longer pin. With the roundness deviation of pin and hole in the DSM of  $8\ \mu\text{m}$ , local slight interference is expected for the longer pin. On the shorter pin, the station is comparable, but due to the line contact only a slight initial play is expected. The pins were checked for signs of wear after each disassembly.

### 7.1.1 Testing and results

For the first assembly with the full mirror weight and orientation, the pins were treated with a thin layer of a molybdenum-carbon dry-film lubricant (Molycote®R321). No problems were encountered during assembly. The pins gradually guided the assembly into its final position as planned. The interface did not come apart on its own once the bolts were disengaged. With help of the threaded rod, parting the interface was accomplished without a problem. A small amount of thin shavings was found on the edge of the cylindrical hole (see Figure 7.2 (b)). Scratches on the pin show that the shavings were removed from the conical section of the pin where the sharp edge of the chamfered hole in the DSM contacted the pin during assembly.

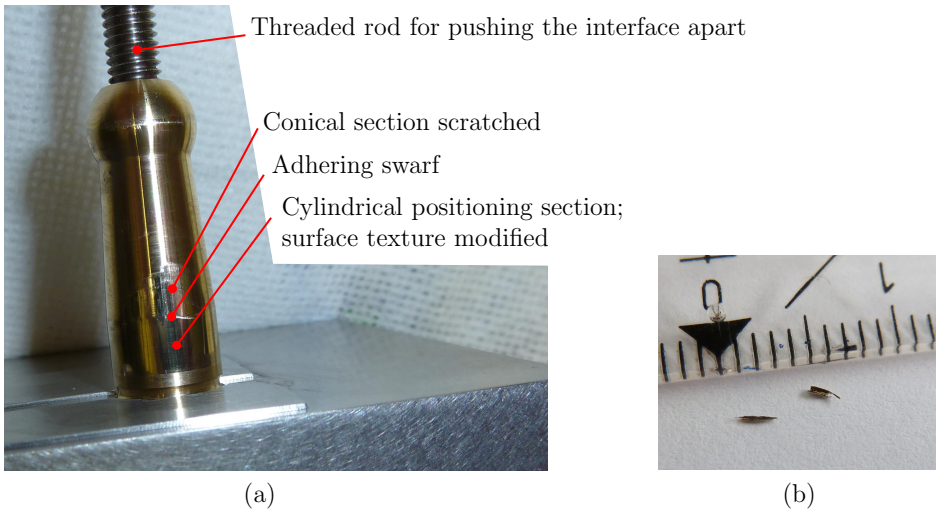


Figure 7.2: (a) Condition of the longer positioning pin after the first assembly at full weight. (b) Shavings from the conical section of the pin.

On the pins' cylindrical section responsible for final positioning, modification of the surface structure was visible. With the marks distributed around the spherical pin circumference on about 30–40% of the surface after the first assembly, it can be concluded that the pin was tight inside the hole. The second pin showed surface marks on two sides, proving the pin came into contact at the upper and lower walls of the long hole. After assembly, a change in diameter of  $1\ \mu\text{m}$  and  $2\ \mu\text{m}$  was respectively measured on the cylindrical section of the pins. These changes are within the measuring tolerance. The roundness of the pins was found to be improved to  $6\ \mu\text{m}$ , respectively  $2\ \mu\text{m}$ , underlining the good positioning and absence of material removal on the critical surfaces.

Subsequent assembly trials were conducted with alkaline-pickled surfaces on all parts involved in mirror positioning. Assembly was tested in different orientations, including horizontal, straight upwards and downwards mirror assembly directions. In all tests, neither jamming nor excessive stick-slip effect was found. Based on the absence of further shavings or deep scratches on the pins' cylindrical sections, it can

be concluded that the positioning of the mirror succeeded in all trials.

### 7.1.2 Conclusions on interface prototype

With none of the orientations showing signs of canting during assembly both with and without lubrication, the assembly and positioning with pins for the tight mirror tolerance is deemed possible with the tested material combination. Positioning to the mirror tolerances is considered successful based on the hole and pin dimensions after assembly and the marks on the pins reaching around the pins. Disassembly succeeded reliably with the threaded helper bolt inside the longer pin, pushing the 30 kg mirror model out of its tight fit.

To prevent the creation of shavings, as happened in the first assembly trial, the design of the DSM was modified with a fillet instead of the chamfer present in the prototype. In addition, the gap in the bolt shafts could be reduced to minimise the angular deviation of the mirror, thereby resulting in a shallower contact angle of the pins and reducing the chance of scratching the pin. The ability for this reduction depends on the play required for engaging the bolts with the DSM after moving the mirror into position on the rails, which was not tested in the set-up.

## 7.2 Mirror substrate prototype

The substrate prototype is designed to test the feasibility of manufacturing the mirror body with an internal cooling channel. As a first step, the weld method and suitable weld parameters are determined. For the prototype itself, the cooling channel halves are manufactured and the welding is carried out. Machining of the mirror's outside shape as well as grinding, polishing and coating of the optical surface were not performed. The manufacturing drawings for the weld body are given in Appendix B.

### 7.2.1 Determination of weld method and parameters

Figure 7.3 shows the geometry of the mirror halves for welding. The main weld is required to be vacuum-tight to the outside. In addition, the plates also require a bond on the inside to prevent deformation of the mirror surface from the internal pressure. To achieve the weld in the whole weld plane, diffusion welding was chosen since it can provide the weld on the whole split surface in one step. Brazing was excluded based on the ban in ITER for wet vacuum brazes. A combined process of brazing for the internal connection and welding on the circumference was considered to be too complex.

Test samples with three geometries ranging in size from 80 mm x 80 mm x 5 mm to 100 mm x 100 mm x 90 mm were used. All samples featured internal channels; see Figure 7.4 for the largest test geometry, closest to the actual prototype.

Two methods of diffusion bonding are included in the testing:

- Uniaxial diffusion welding (UDW), where the work-piece is heated in a press under vacuum or protective gas. The weld pressure is applied perpendicular to the weld surface.

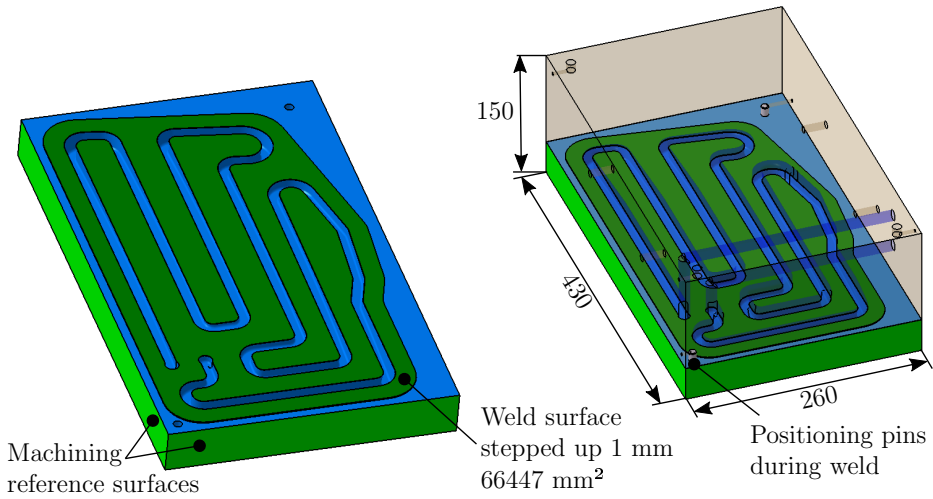


Figure 7.3: M2 prototype structures for welding of the cooling channel.

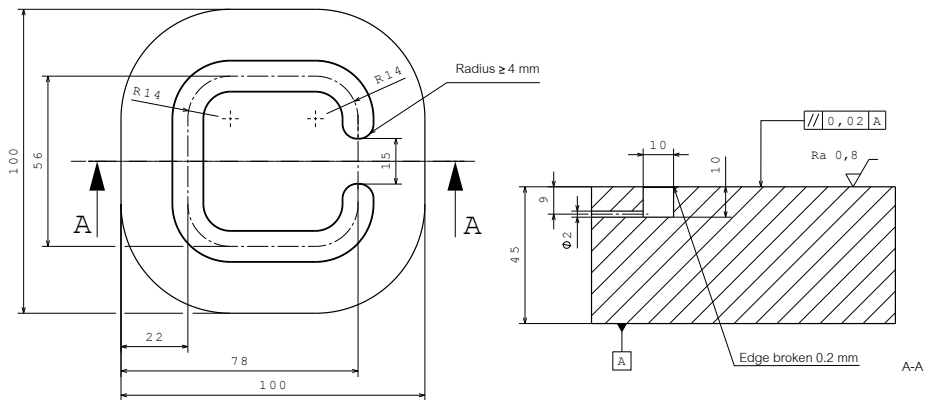


Figure 7.4: Test block geometry No. 3. Two blocks realise a weld test with internal channel. The sideways drill hole improves evacuation during welding, allowing easy vacuum leak testing after welding.

- Hot isostatic pressing (HIP) where the work-piece is placed in a welded container and a vacuum is drawn. The container is then placed in a pressurised gas chamber and everything is heated to weld temperature.

### Unsuccessful weld attempts

Due to limitations in available press dimensions for the actual prototype, first tests of UDW were conducted with a temperature limit of 1050 °C on samples of 1.4429 and 1.4435. Before heating the samples, a vacuum of  $10 \times 10^{-5}$  mbar was created. For the limited temperature and pressure, a number of test welds were created but no

sufficient weld could be achieved. The following parameters were tested:

- Weld pressures ranging from 10 MPa to 50 MPa
- Weld times from 1 h to 6 h
- Additional treatments of the weld surface: alkaline pickling, grinding, high-precision stress-free grinding for minimal plate thickness deviations

Metallographic specimens of these tests show that the 1.4429 and 1.4435 material did not undergo sufficient plastic deformation at the temperature, and shape deviations could not be compensated for by plastic deformation. Where the samples did come in contact, welding and grain growth is visible with numerous weld defects remaining (see Figure 7.5 (a) and (b) for examples). Within the parameter range, no trend in weld quality could be determined for the parameters.

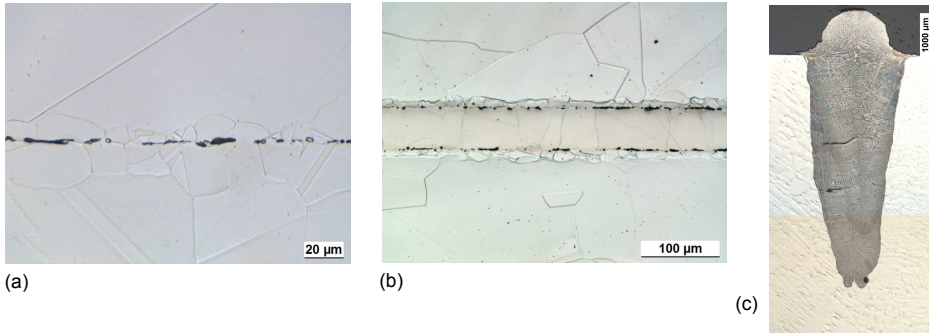


Figure 7.5: Welds with defects. (a), (b): UDW welds with remaining porosity where (b) includes a Ni-foil between the stainless steel blocks. (c) UDW weld with e-beam re-welding from the outside.

With only the outside of the weld required to be vacuum tight, re-welding of the outer seam by e-beam welding was tested. For these welds, crack formation was found inside the weld (see Figure 7.5 (c)). Weld settings avoiding crack formation in the 1.4435 material outside standard weld parameters for the material was not tested as the licensing for ITER with the limited weld depth is unlikely as full penetration welds are required by the code.

HIP welding of a sample at 1150 °C, 100 MPa and 4 h crushed the internal channel completely, as expected with the parameters, but resulted in a perfect weld with no defects, thus proving the feasibility of diffusion welding of the material. Further HIP-welding trials with reduced temperature and pressure were not successful with the appearance of an oxide layer in the weld interface and too unpredictable plastic deformation. With the lack in weld progress monitoring for HIP, the number of necessary weld trials with the same geometry and possibly even material heat number was not seen as feasible for the prototype.

### UDW machine parameters

Successful welding by UDW was achieved at 1050 °C and 20 MPa over the time of 12 h with a plastic deformation of 2.2%. With the welding press at Forschungszentrum Jülich (FZJ) not capable of welding the prototype due to size limitations, a machine at the Institute for Micro Process Engineering (IMVT) [38] of the Karlsruhe Institute for Technology (KIT) was used for the full scale prototype.

To reduce the required weld time, the temperature at IMVT was increased to 1075 °C and a tight weld at 4.4% plastic deformation was achieved within 4 h for the test geometry in Figure 7.4. Figure 7.6 shows representative cuts of the successful welds at KIT and FZJ.

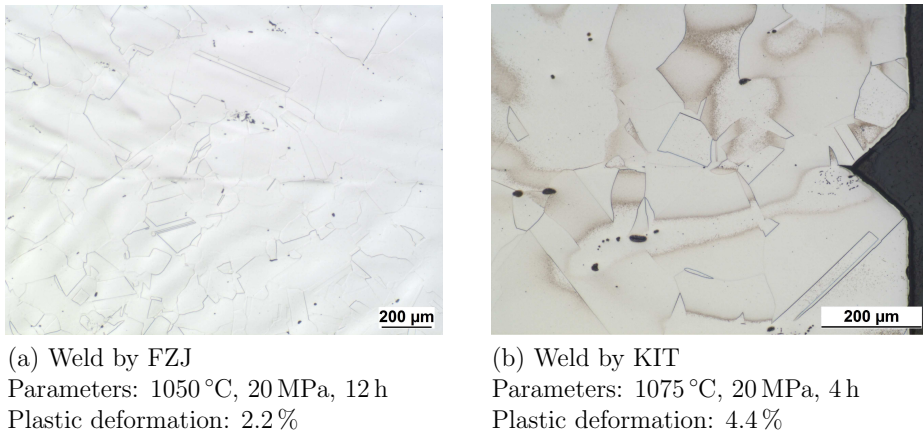


Figure 7.6: Metallographic sections of successful UDW welds and the machine parameters.

### 7.2.2 Mirror substrate diffusion bonding

Two pairs of mirror halves for the test were manufactured. Machining of the weld surface and cooling channels was carried out on a MDU 80 monoBLOCK five-axis CNC machining centre by Deckel Maho. The roughness achieved for the weld surface was measured as  $R_{a,max} = 0.68 \mu\text{m}$  ( $R_{a,mean} = 0.42 \mu\text{m}$ ,  $R_{z,max} = 3.44 \mu\text{m}$ ).

The maximum planarity deviation measured is 0.059  $\mu\text{m}$ , where about a quarter is due to a single measurement point sticking above the surface. Three of the four weld surfaces show a slight curvature with a raise in the middle of the part. The highest parallelism deviation of the four blocks was measured as 0.055  $\mu\text{m}$ . With the step-up of 1 mm from the block to the nominal weld surface, the combined local shape deviations of <0.1 mm are expected to be flattened out during the weld. The last locations expected to come into contact during the welds based on the measured shape are on the outside of the mirror and were looked at with metallography sections.

Diffusion bonding of the first prototype at IMVT was done at a nominal 25 MPa and 1075 °C. Pressing the specimen led to a deformation of 4.2% ( $\Delta z$  of 6.3 mm for

the 150-mm-thick combined block). The large deformation was likely caused by problems with the temperature measurement due to a faulty thermocouple. The second specimen was welded with repeated manual adjustment of the weld parameters, reacting to the weld progress (see Figure 7.7). The second weld shows a bulk deformation of 1.8 %.

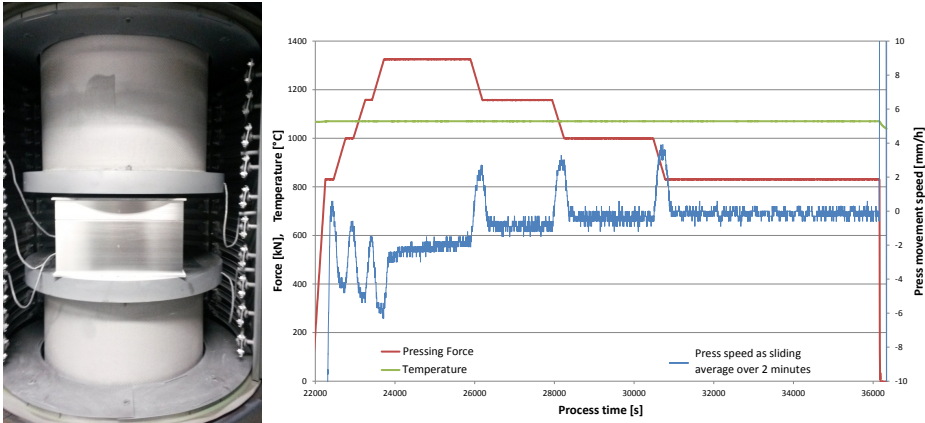


Figure 7.7: Vacuum press at KIT used in welding the prototypes, and plot of weld parameters and deformation progress for the second block. Image on left: IMVT [38]

For both blocks, a 2D resolved ultrasonic examination was carried out to detect potential areas of incomplete bonding. Figure 7.8 shows the time of flight measurement of the front side of block 2. Both prototypes did not show an echo at the nominal weld surface around the cooling channel, proving the absence of extended gaps in the diffusion bond. The shape deviation of the internal cooling water channel after diffusion welding could not accurately be determined by the time of flight measurement. Limiting were both the high thickness of the material exceeding 100 mm on the back side and the spherical shape of the cooling channel on the front side, leading to the uneven depth measurement as visible for the channel in Figure 7.8.

Metallographic sections show complete fusing of the diffusion bond surface, see Figure 7.9. Crystal growth though the dividing surface is visible and no cavities remain. No cohesive layer of oxides or other impurities is visible. Figure 7.9 (a) shows the weld at the nominal 1 mm step where the nominal diffusion bond area starts. The gap between plates is closed starting immediately where the material comes in contact. (b) shows the weld some mm from the start of the contact.

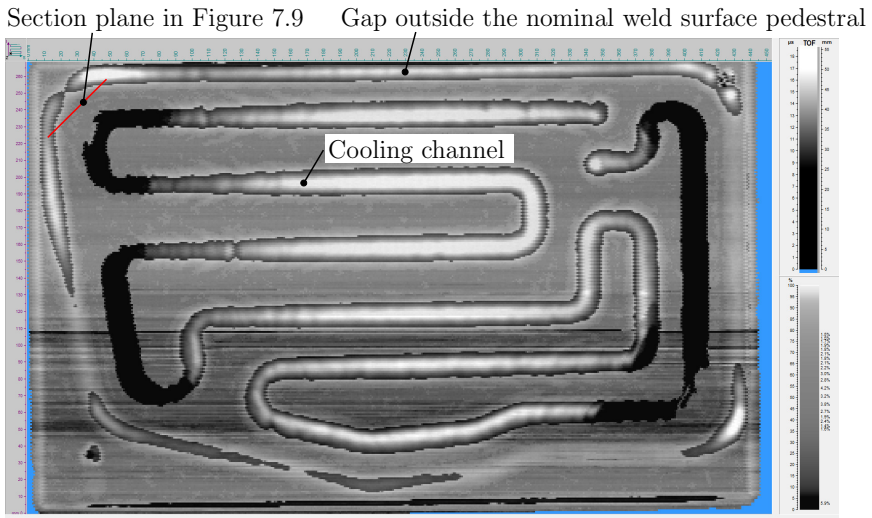


Figure 7.8: 2D resolved time of flight ultrasonic examination of the front of test block 2. The weld surface does not give a signal, the depth plotted (around 40 mm) is due to machine settings.

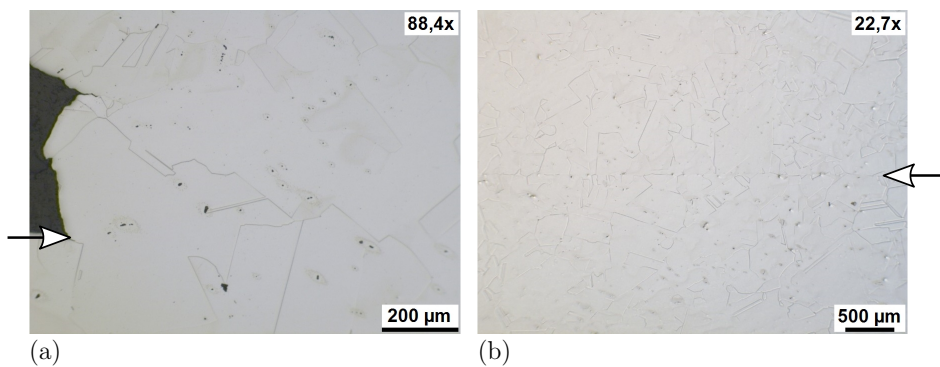


Figure 7.9: Metallographic section of the full size prototype uniaxial pressure diffusion bond. The arrows show the location of the weld layer.

### 7.2.3 Conclusions substrate prototype

Creation of the internal cooling channel by diffusion bonding was achieved with the 1.4435 stainless steel material. The weld was found to be vacuum tight, free of extended cracks and with a near perfect bond of the plates with little inclusions. As the geometry of the mirror does not allow radiography, production proof samples of the full size geometry would be required for the actual mirrors as no destructive testing can be used. The use of a scaled geometry is not seen as feasible for the weld sample as the weld parameters were found to differ significantly for different geometries.

The detailed deformed geometry of the cooling channel after diffusion bonding was not determined. Based on the ultrasonic examination, the geometry is deemed to be suitable.

## 7.3 Dielectric mirror coating on stainless steel substrate

The option of using multilayer dielectric coatings inside the diagnostic port of ITER is critical with regards to the coating stability as discussed in Chapter 4. It is considered for core CXRS to maximise light throughput for Mirrors 4 to 7, but significant testing is required to demonstrate feasibility before the coating can be used on any substrate. Going beyond the state of the art, the candidate coating for core CXRS is made from  $\text{SiO}_2/\text{TiO}_2$  on a stainless steel substrate and optimised for stability of the interference rather than minimise the number of layers. The goal of the test is to show short-term behaviour of the coating on the steel substrate and investigate its stability under long-term ITER thermal conditions. Coating of the stainless steel with Rh is not included in the tests, as ongoing efforts to establish Rh as coating for the first mirror were already under way [41].

The dielectric coating was designed for the following requirements:

- Specular reflectivity exceeding 98% at the core CXRS diagnostic wavelengths in the range of 450 nm to 670 nm
- Flat reflectivity curve around the diagnostic wavelength bands to minimize the impact of the reflectivity dependence on incidence angle and polarisation angle
- Coating on 1.4429 stainless steel substrate
- Long-term thermal stability up to 250 °C
- Coating stability when exposed to air, dry nitrogen (standard conditions) and  $\text{H}_2\text{O}_{(gas)}$  (100 °C)

### 7.3.1 Manufacturing and initial characterisation of the mirrors

Based on the requirements, sample mirrors of diameter 17.5, 50 and 100 mm were manufactured by S1Optics [84] with a coating of  $\text{SiO}_2/\text{TiO}_2$  (Figure 7.10). The coating

was selected based on existing knowledge of the material for use at elevated temperature by SIOptics and due to its favourable optical properties.  $\text{TiO}_2$  was chosen despite the reported possibility of crystallization to the anatase crystalline form of  $\text{TiO}_2$  from the amorphous state, as deposited during manufacturing above  $200^\circ\text{C}$  [104][73].

The European-grade stainless steel 1.4429 is used as substrate and is close in composition to the 316L(N)-ITER grade. One BK7 glass substrate was coated in the same batch. The coating consists of 32  $\lambda/4$  double layers, deposited by reactive electron beam evaporation of  $\text{SiO}_2$  and  $\text{Ti}_3\text{O}_5$  under reactive conditions, with  $\text{O}_2$  as the process gas onto the substrate at  $150^\circ\text{C}$ . The prototype coating is designed for target reflectance at a  $25^\circ$  incidence angle and room temperature. The double-layers of the coating are arranged in three groups of constant thickness, minimising jumps in layer thickness for a reduction of internal stresses for the price of a higher layer count (substrate|(HL)<sup>12</sup>(HL)<sup>8</sup>(HL)<sup>12</sup>|air). The overall coating thickness reached  $5.26\ \mu\text{m}$  and the first layer on the substrate is  $\text{TiO}_2$ .

The 1.4429 substrate material used for substrate manufacturing was not of electro slag remelted quality. Polishing succeeded and visual inspection revealed differences after polishing with the three  $\varnothing 100$  and one of the 50 mm mirrors looking the best. Surface roughness measurements showed values of  $R_a = 2.6$  to  $4.5\ \text{nm}$  (see Table 7.2 for more detailed roughness numbers on representative substrates).

Table 7.2: Condition of representative mirrors. Standard deviation is given in parentheses ( $1\cdot\sigma$ , abs.). Specular reflectance (R) is given as mean in the full range of 460 to 663 nm under an angle of incidence of  $25^\circ$ .

Sample	$\varnothing$ [mm]	$R_a$ [nm]	$R_z$ [nm]	R [%]
1	100	2.6 (0.5)	27.2 (9.1)	97.34
6	50	3.6 (0.2)	32.7 (2.6)	95.41
7	50	2.6 (0.7)	35.3 (13.9)	94.9
11	50	4.5 (0.2)	39.4 (4.0)	97.94

With no experience in the coating of  $\text{TiO}_2$  on stainless steel, preliminary adhesion tests were conducted with coatings consisting of only the lower 20 layers of the full coating. The intermediate layers on 1.4429 included in the testing are  $\text{SiO}_2$  (50 nm and 80 nm), Cr (30 nm), a 80-20 amorphous mixture of  $\text{SiO}_2$  and Cr, and the 73-nm  $\text{TiO}_2$ -layer of the real coating. The samples were tested for adhesion in accordance with DIN ISO 9211-4 [1]:

- Rubber abrasion test with 20, 40 and 60 strokes at  $10 \pm 1\ \text{N}$  contact pressure (indirect test also of adhesion via surface fatigue)
- Adhesive tape (adhesive power  $>9.8\ \text{N}$  per 25 mm width) rip-off test at a speed of  $\ll 1\ \text{s}$  per 25 mm (jerky)

All samples survived the tests without visible damage. At the time of mirror manufacturing, long-term elevated temperature testing could not be conducted under vacuum as the test chamber was not yet available. It was decided to coat the prototype mirrors without interlayer, as adhesion was deemed sufficient.

Table 7.3: Overview on samples used during testing.

Materials and dimension	Count
Full coating on $\varnothing$ 17.5 mm 1.4429 substrate	4
Full coating on $\varnothing$ 50 mm 1.4429 substrate	6
Full coating on $\varnothing$ 100 mm 1.4429 substrate	3
Full coating on 25 x 65 mm BK7 glass substrate	1
Partial coating with different interlayer on $\varnothing$ 50 mm 1.4429 substrate	1 per combination

Figure 7.10: 17.5 mm, 50 mm and 100 mm  $\text{SiO}_2/\text{TiO}_2$  dielectric coated mirrors on 1.4429 stainless steel substrate used in the testing.

Measurement of the total and diffuse reflectance were conducted with a PerkinElmer Lambda 950 spectrophotometer at a  $8^\circ$  incidence angle. The coating on BK7 glass substrate achieved a specular reflectance exceeding 98% for most wavelengths within 450 to 670 nm (see Figure 7.11).

On the stainless steel substrate, the reflectance is reduced at shorter wavelength because of shortcomings in the polishing. With the polishing as manufactured, texture variations in the optical properties depending on location and rotational orientation are present. The mirrors show variations in total reflectance up to 10% at reflectance peaks and shifts of the peaks up to 5 nm depending on orientation and location. The differences coincide with the relative direction and visibility of the polishing marks of the metallic substrate. Because of these variations, direct comparisons between mirrors were not performed and plots only show measurements at the mirror centre with stable rotation and no averaging over multiple locations. The repeatability of the optical measurements with removal and re-positioning of the mirrors based on marks engraved on the mirror was tested to be within 1% for the total reflectance.

### 7.3.2 Long-term thermal testing

The set-up for thermal testing consists of a vacuum chamber with three independent units (Figure 7.13), each able to hold two mirrors. The units are electrically heated to a maximum of  $420^\circ\text{C}$  and cooled by an internal gas flow. Vacuum levels of better than  $1 \times 10^{-3}$  Pa were attained before heating of mirrors was started, and pressures below  $1 \times 10^{-5}$  Pa were present after the first thermal excursion of each test run. The

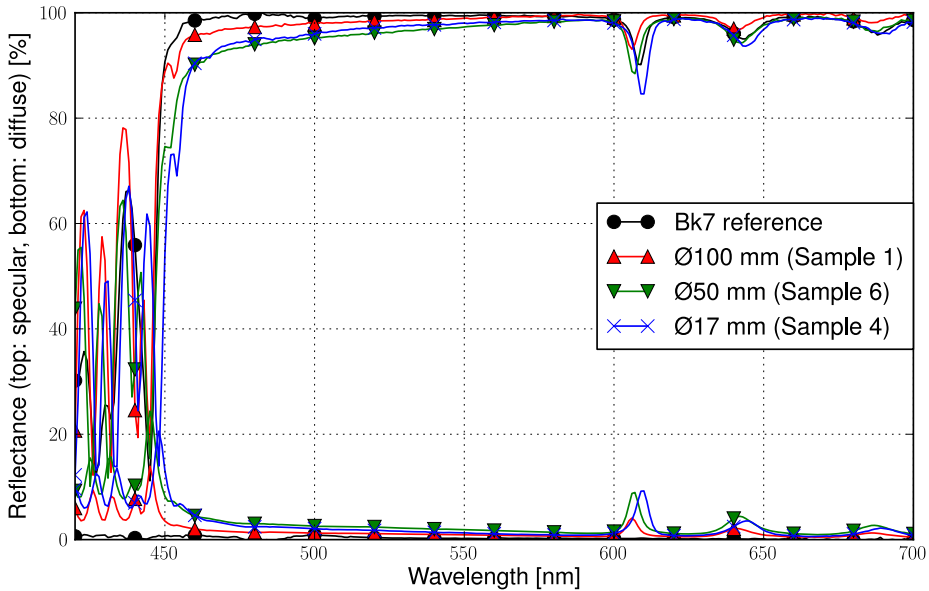


Figure 7.11: Initial reflectance of representative mirror samples. Markers are shown every 20 data points.

Table 7.4: Main nominal thermal conditions of the samples.

Sample	Main test condition
1, 12	steady-state at 200 °C
4, 11	steady-state at 260 °C
2, 6	thermal cycles to 260 °C
BK7	steady-state at 260 °C
8, 9	Reference in vacuum and air at room temperature

thermal contact of the mirror samples with the support is provided by a 2 mm layer of PAPHYEX®<sup>®</sup>, a ductile sheet of pressed graphite flakes. The temperature of the metallic substrates was measured inside the material at the bottom of 20-mm-deep holes at the substrate mid-plane. The coating temperature could not be measured but is expected to be close to the core temperature based on simulation and the measured thermal gradient to the heating plate centre, which did not differ by more than 5 °C from the mirror core temperature under steady-state conditions.

The nominal thermal test conditions are summarised in Table 7.4. Heating was started at a residual gas pressure  $<1 \times 10^{-3}$  Pa. The thermal heat-up and cool-down rates were limited to  $\pm 20$  K h<sup>-1</sup>. Figure 7.14 shows typical temperature profiles of a shorter test with three temperature zones and five samples. The steady-state thermal loads were applied in excess of 1000 h and a thermal cycle count of 55 was reached.

In contrast to the expected behaviour of the coating, based on literature, no significant change in reflectance was found after exposure to ITER thermal loads. Figure 7.15 shows the result for the representative sample No. 11, exposed to temperatures of

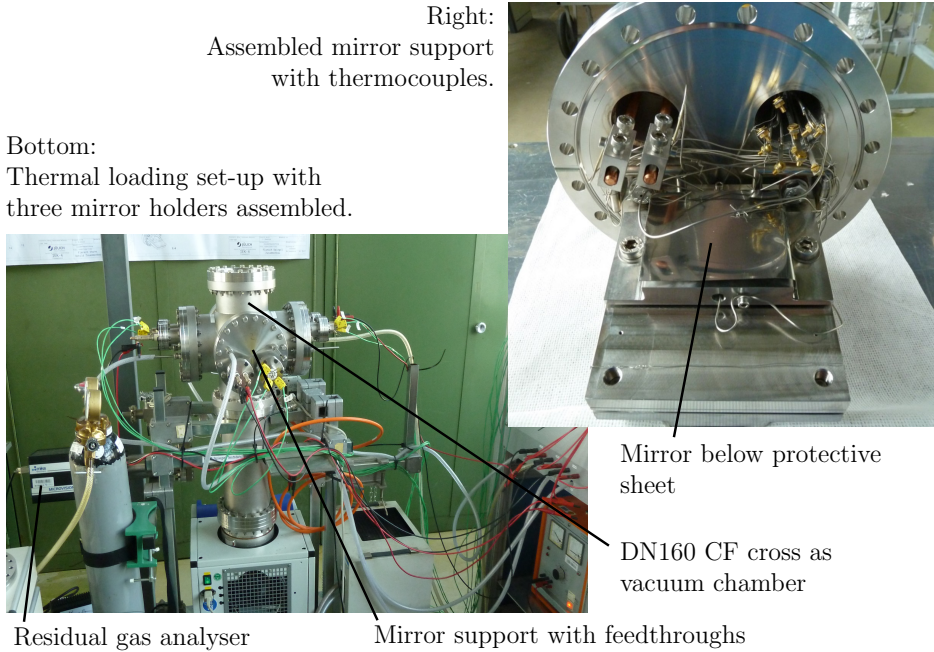


Figure 7.12: Vacuum chamber test set-up for thermal stressing of the coating.

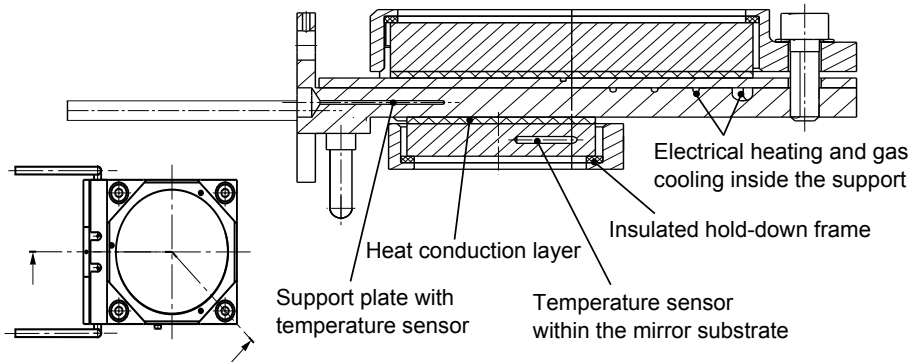


Figure 7.13: Mirror support structure for long-term and repeated cycles thermal testing.

250 °C and higher. While changes in specular reflectance of up to 5% at the reflectance dips were measured, no trend over time emerged. Heating of the coating on BK7 to 260 °C did not change the optical properties of the coating either, but doubt remains whether the glass sample did reach nominal temperature, as no internal sensor could be added and the hold-down pressure on the glass was limited.

Exceeding ITER environmental conditions, the application of single thermal gradients of  $+200\text{ °C h}^{-1}$  and  $-100\text{ °C h}^{-1}$  did not lead to immediate damage of the coating

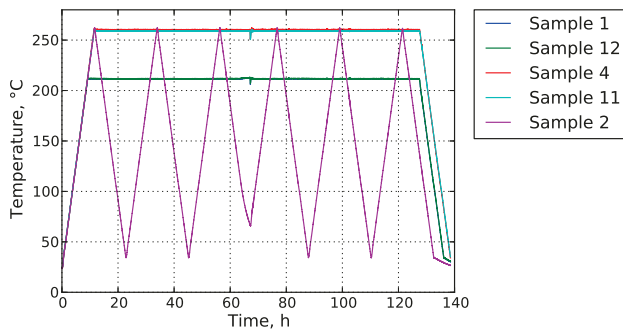


Figure 7.14: Temperatures as measured in the centre of the mirror samples during a short test. At 68 h, the heating was interrupted shortly due to controller problems and restarted.

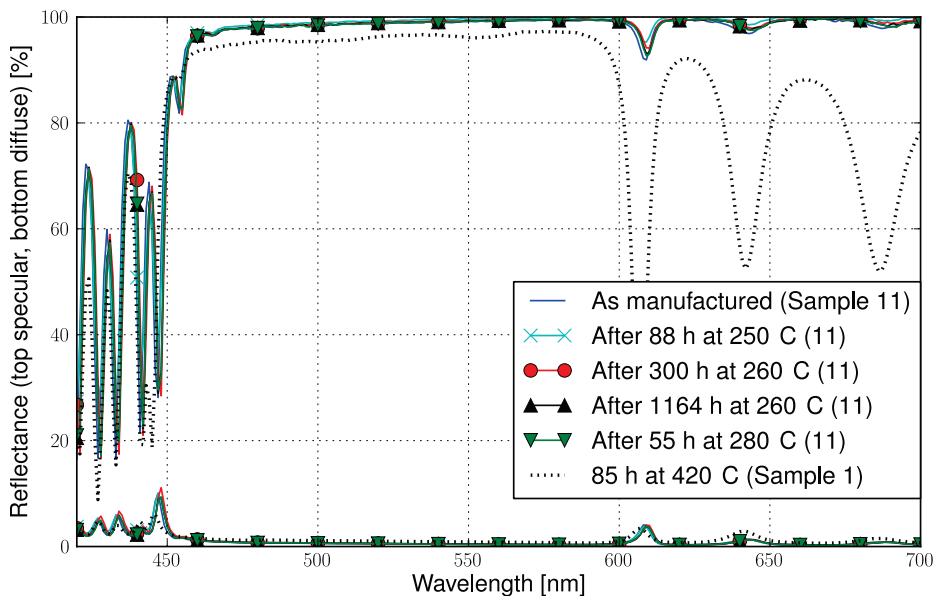


Figure 7.15: Reflectance of Mirror samples 1 and 11 after different thermal loads.

or higher susceptibility to subsequent damage. Heating to 350 °C over 1 h was tested with no significant change in reflectance. Exposure of the coating to 420 °C finally led to significant changes in the reflectance of the coating (see Figure 7.15).

The remaining gasses in the chamber were monitored by a residual gas analyser (MicroVision Plus) during the first runs. Apart from the anticipated outgassing and leaking of the vessel ( $\text{H}_2\text{O}$ ,  $\text{N}_2$ ,  $\text{O}_2$ ), CO and  $\text{CO}_2$ , two gasses with an atomic weight of 48 and 64 (up to  $1 \times 10^{-8}$  mbar partial gas pressure) were detected at elevated

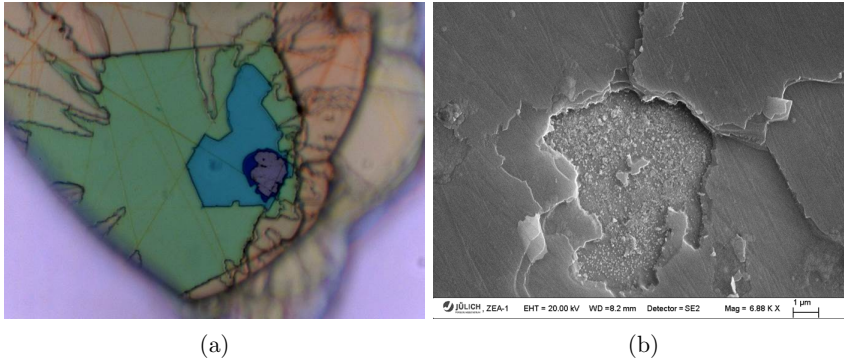


Figure 7.16: Details of flaked-off defects reaching all the way to the substrate with delamination visible on multiple depths. a) White light microscope at 100x. b) SEM image (surface coated with a thin Rh layer).

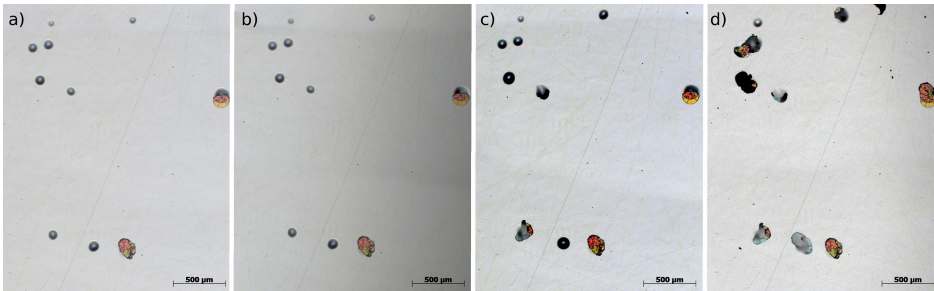


Figure 7.17: Advance of bubbles and flaking in the coating for a larger group on Sample 11.

temperatures. It is probable that the two unidentified gases were SO and SO<sub>2</sub> from the graphite thermal contact interlayer. The peaks in release rate coincided with the times of highest temperature and higher peaks are present at times where a new pad was used.

### 7.3.3 Blister formation and flaking

After 17 days at temperatures exceeding the manufacturing temperature of 150 °C, the formation of blisters and first flakes was noticed. The time of first occurrence could not be reliably identified. With temperatures up to 350 °C, the flakes reached a size up to 100 µm. The number of defects, ranging from one to about 50 on a Ø50 mm mirror, as well as their distribution, single defects or local groups with up to 20 defects, varied greatly between samples. The number of defects was not high enough to show in the reflectance measurements where a spot size of 3 mm times 5 mm was used. The coating on BK7 glass did not show any defects after heating to 260 °C for 121 h.

The coating damage progressed over several days (see Figure 7.17). The images

Table 7.5: Defects on  $\varnothing 50$  mm samples with reduced coating and different first layer on the stainless steel found with microscope inspection after 28 days at 260 °C.

Interlayer	Defects
30 nm Cr	No blisters or flakes
50 nm SiO <sub>2</sub>	5 half-detached blisters
50 nm SiO <sub>2</sub> -Cr 80-20 mixture	1 blister, 4 flakes
No interlayer (85.13 nm TiO <sub>2</sub> )	>50 half-detached blisters
80 nm SiO <sub>2</sub>	1 flake

correspond to: a) After 35 days at 260 °C; b) After exposure to H<sub>2</sub>O(g)-atmosphere over 2 h; c) +10 days at 260 °C; d) +7 days at 260 to 280 °C. The colour of the flaked-off defects is a result of the varying relative reflectance of the three colour bands in the coating, depending on the local number of coating layers present.

Defect growth seemed to stop towards the end of testing at 260 °C and no new blisters were found to be developing. Heating to 420 °C led to about triple the number of defects and larger defect size. Scanning electron microscope images show that the defects reach the metallic substrate at single points and the coating to be ablated around the deepest point at multiple depths. The shape of the defects indicates damage as described in [52] (different environment, coating and cause of damage).

The five partially coated mirrors with different interlayers, originally manufactured for adhesion tests at room temperature, were also exposed to 260 °C over 28 days. Details on the coating and resulting damage are given in Table 7.5. Taking into account the observed diverse behaviour of the full coating, only one sample per interlayer type and the possibility of pre-existing damage by the initial adhesion testing (tape rip-off test and 60 cycles chafing test at 10 N load), the test can only give a tendency. In the test, a Cr interlayer proved most beneficial, but all samples with an interlayer showed fewer defects than the mirror with the same history having TiO<sub>2</sub> directly on the 1.4429 substrate.

### 7.3.4 Exposure to water vapour

Testing for the impact of a water ingress event was restricted to testing the survivability of the mirror coating when exposed to a water vapour atmosphere while heated to 120 °C. Ingression events with fluid water on the mirror surface are assumed to degrade reflectance to a level where replacement of the mirror is necessary and were not tested. Indirect ways of liquid water reaching the mirror as, e.g. condensation on the surrounding wall dripping onto the mirror, are expected to be prevented by the system design.

The set-up for testing consists of a heated chamber where the mirrors are located (see Figure 7.18). The mirrors are heated in a nitrogen atmosphere at ambient pressure to 120 °C at 40 K h<sup>-1</sup>. Temperature during the test was monitored for the gas and inside the mirror substrate. With the mirror at 120 °C, water vapour is added to the chamber and the nitrogen flow stopped, keeping air from entering the chamber with the constant gas flow. The mirror was left in this condition for 2 h. For cool-down, the nitrogen flow is re-established and the water vapour flow stopped. The mirrors

were cooled down to 50 °C over 3 h before being removed from the chamber. No condensation marks were apparent on the mirror after removal.

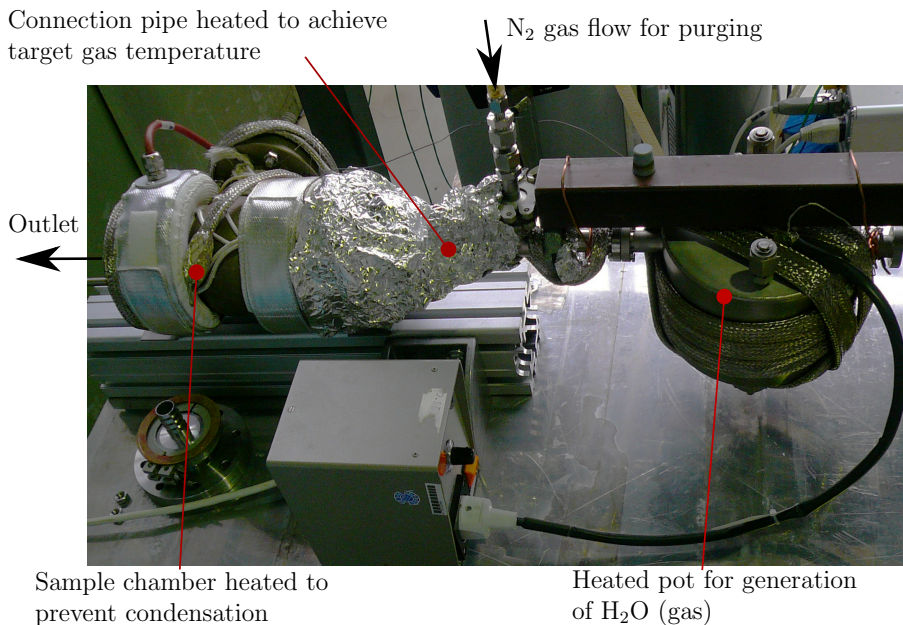


Figure 7.18: Set-up for testing of coating stability under water vapour atmosphere at 120 °C with most of the Al foil used for thermal insulation removed.

Two mirrors, 11 and 12, were exposed to the water vapour. They were chosen because they showed two distinctive states in their defect progression: Mirror 11 already had places where flaking occurred as well as some remaining closed blisters, while Mirror 12 only suffered small and medium-sized blisters with no flaking. The state of damage for a small area on Mirror 11 is shown in Figure 7.17 b) in the previous section.

After exposure, no immediate changes in the coating damage and optical properties could be observed. The mirrors were stored in air for five days before further thermal testing was conducted. The mirrors did not react noticeably differently to subsequent testing than the other samples.

### 7.3.5 Reflectivity measurements at elevated temperature

Two mirrors were heated in vacuum to 300 °C and their specular reflectance measured at elevated temperature. These were Sample 6, which was previously heated to 350 °C, and Sample 8, which was not heated beyond 40 °C since manufacturing.

The measurements were carried out by I. Orlovskiy and E. Andreenko of the National Research Center ‘Kurchatov Institute’, Moscow. The set-up uses a stabilised tungsten lamp for illumination and a Monochromator LOMO MDR-204 plus photomultiplier for direct measurement of the specular reflectance through a vacuum

window. All measurements were taken at an  $8^\circ$  incidence angle as governed by the test set-up. Calibration of the set-up is achieved by in-air reflectance measurements of the sample with the PerkinElmer Lambda 850 spectrophotometer at room temperature and an in-air reference mirror in front of the vacuum window during the testing. Even with careful calibration, the measurements at elevated temperature are seen as relative measurements.

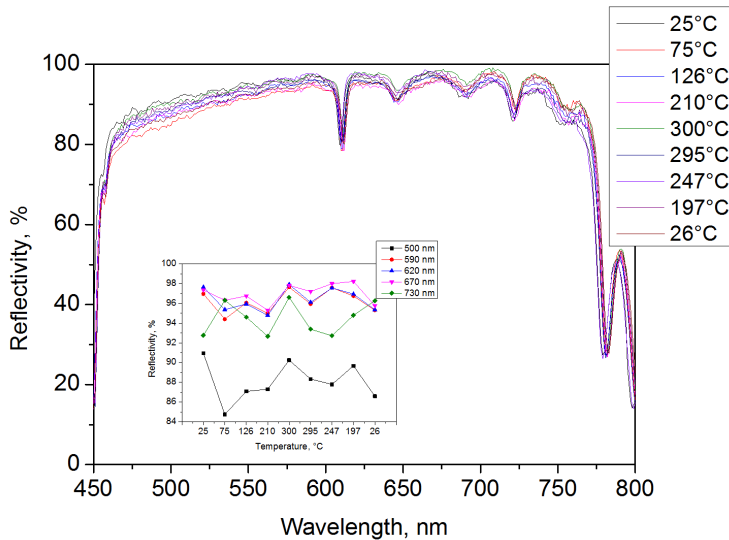


Figure 7.19: Relative specular reflectivity of Mirror 8 during a temperature cycle. The embedded diagram shows the reflectivity evolution at different wavelength over the cycle.

The temperature did not lead to damage of the coating or significant change in optical properties for either mirror. Figure 7.19 shows the specular reflectivity of Mirror 8 during the temperature excursion. The reflectivity variation at elevated temperatures of 4% is within the measurement accuracy of the set-up.

### 7.3.6 Composition of the coating

The presence of titanium- and silicon-oxide as coating material with no significant presence of other materials was shown by energy-dispersive X-ray spectroscopy (EDS). X-ray diffraction (XRD) measurements of the coating were conducted in  $\theta/\theta$ -mode in wide-angle arrangement and grazing incidence. Measurements of the coating as manufactured and after exposure to  $350^\circ\text{C}$  showed no crystalline phases of any stoichiometric composition of Si- or Ti-oxide ( $<1\%$  detection limit). Measurement of the sample heated to  $420^\circ\text{C}$ , which exhibited the change in optical properties, revealed the presence of well-crystallised  $\text{TiO}_2$  in the anatase phase and broader reflections of a rutile  $\text{TiO}_2$  phase, likely caused by smaller crystal size or lattice defects. No other  $\text{TiO}_x$ -phases were found. The  $\text{SiO}_x$  layers remained amorphous in all measurements.

Full identification of the stoichiometric composition of the titanium oxide could not be achieved as no method was found to determine the composition of the  $\text{TiO}_x$ -layer inside the coating. Based on the high optical quality of the coating and the presence of well-formed  $\text{TiO}_2$  crystals after heating, it is assumed that the stoichiometry of the titanium oxide coating layer is close to the target of  $\text{TiO}_2$ . The reason for the delayed crystallization of the titanium oxide compared to literature could not be determined.

### 7.3.7 Conclusions on dielectric mirror coating

The  $\text{TiO}_2/\text{SiO}_2$  by SIOptics reached the desired mean specular reflectance in excess of 98% within the range of 460 to 663 nm. The reduced reflectance of the coating on the stainless steel substrate was found to be linked to the increased roughness and polishing texture of the non-electro-slag remelted substrate material. Apart from the polishing marks, the stainless steel substrate was not found to exhibit a direct impact on the optical properties of the coating.

The formation of bubbles and subsequent flaking of the coating seems to be linked to local insufficient adhesion of the coating to the stainless steel substrate. With the mirror samples featuring a reduced number of coating layers, the presence of a Cr or  $\text{SiO}_2$  interlayer on the stainless steel reduced blister formation and flaking. The time progression for the blister formation over several days underlines the need to conduct testing beyond one or two cycles to show suitability of coatings for the nominal 20-year lifetime of ITER.

The  $\text{TiO}_2/\text{SiO}_2$  coating was found to exhibit stable reflectance to 350 °C. Longer-term coating stability at 260 °C was shown in tests with 55 thermal cycles and times exceeding 1000 h. It was not affected by exposure to water vapour at 120 °C over 2 h. The reason for the high thermal stability of the coating should be examined further based on the preferable optical properties of  $\text{SiO}_2/\text{TiO}_2$  material.

The high thermal stability of the coating described here compared to similar published investigations is also seen as caution sign. The large range of reported coating behaviour accentuates the difficulty with getting the coating right. The decision to use a dielectric coating of this type should include long-term testing under realistic conditions of the exact coating, manufacturer, machine and procedure, which is destined for in-vacuum use in a fusion diagnostic system where a damaged coating cannot be easily retrieved. Otherwise, protected aluminium, and depending on activation limits: silver, are other options with slightly reduced reflectance.

# Chapter 8

## Summary and discussion

Diagnostic systems are required in nuclear fusion for machine control, machine protection and to improve the understanding of plasma physics. Photons are one of the main carriers of information from the plasma region, being created by, or having interacted with the plasma, in a number of ways. To enable the use of photons in the wavelength range from ultraviolet to infrared, optical mirrors are required inside the vacuum vessel to guide the light through the internal components of the reactor towards protected optical windows at the boundary to air. In this work, general considerations on mirror design for fusion reactors are given and a solution specific to the core CXRS diagnostic system of ITER is worked out.

The loads and environmental conditions as found close to the fusion plasma inside the vacuum vessel are identified and discussed. These include high vacuum, neutron and gamma radiation as well as particle, heat, general mechanical and electro-mechanical loads. It is shown that especially the interaction of the different environmental conditions limit the design space beyond what is found for other mirrors. One example of a limitation arising from a combination of environmental conditions is the restricted use of materials which exhibit radiation induced out-gassing, relevant in fusion as both high energetic radiation and a man-made vacuum are present.

Existing mirror designs employed in fusion experiments and outside the fusion field are analysed. It is found that no readily available design fulfils the combined environment of a fusion reactor with extended DT operation. Especially the presence of tritium and the increased activation by neutron irradiation is found to require adapted solutions. Available mirror designs which satisfy or exceed a subset of the fusion reactor conditions are discussed.

Generic design solutions of central functional aspects of mirrors in fusion are explored. The realizations are analysed and evaluated against the fusion environment. Their scope of application is discussed together with their individual limitations and advantages. An emphasis is put on robustness and long-term stability of the design as maintenance possibilities are limited and require downtimes of months for even small repairs. The general considerations are worked out on the topics of substrate material selection, adjustment during assembly, maintenance and temperature control of the system.

A comprehensive design for the second to seventh mirror of the ITER core CXRS diagnostic is presented. The solution takes into account the specific requirements of

the system: Limited space, high transmission in the visible light spectrum and a resolution of several mm through the 10 m long optical path, allowing for mirror surface irregularities of 10 to 100 fringes. An emphasis is put on the maintainability and decoupling of the mirrors from the diagnostic shielding module which acts as optical bench but exhibits temperature instability. The proposed layout is an all-metallic design with materials of similar thermal expansion. The mirror substrate is bolted to the radiation shield from the side and can slide out with limited disassembly of the whole system. Thermal-mechanical simulation is performed to study the feasibility of the design. The design is found to be suitable for core CXRS.

Critical aspects of the proposed mirror design were identified and addressed with prototypes. A prototype of the critical part in exchanging a mirror by remote handling with positioning of the substrate within the tight optical tolerance with pins showed no jamming during assembly and disassembly. The design of the positioning structure was improved based on the prototype.

Manufacturability of an shaped internal cooling channel inside a stainless steel substrate is shown by diffusion bonding and in accordance with the quality requirements of ITER. The full scale prototype exhibits perfect bonding at the extended weld surface. Substrate deformation was found to be significant but workable with the weld parameters producing a full bond.

The behaviour of a  $\text{SiO}_2 / \text{TiO}_2$  dielectric multilayer coating on stainless steel substrate was tested for a subset of ITER conditions, particularly exposure to elevated temperature. The coating, optimised for a robust reflectance and minimised internal stress, showed unexpected stability at ITER temperature conditions and up to 350 °C. Blisters formation occurred, but did not impact the overall reflectance significantly. The coating was found to be stable under water vapour atmosphere at 120 °C.

Overall, the design proposal for core CXRS is found to be suitable. The use of an internal cooling channel as initially proposed is deemed disadvantageous with the updated, stable feed water temperature at  $70 \pm 5$  °C and the modified core CXRS optical layout, featuring mirrors further from the plasma with reduced heating by radiation. The internal fluid flow is not necessary to stabilise mirror temperature during operation but increases manufacturing and maintenance complexity as well as creates a risk of vacuum leaks.

The suitability of a multilayer dielectric coating under ITER conditions requires further investigation. While the results for the  $\text{SiO}_2/\text{TiO}_2$  coating on stainless steel substrate were positive, the question of why exactly the thermal stability of this batch exceeds literature values with no crystallization of the  $\text{TiO}_2$  until heated above 350 °C could not be answered. In case a dielectric coating is chosen, additional testing is deemed necessary, including a full-scale prototype, preferably produced by the same manufacturer as the final system.

The mirror concept proposed for core CXRS is not feasible as general design for all ITER diagnostic systems. Adapting the solution to other diagnostic systems is deemed possible within limits, especially where a similar, limited optical resolution is required. Additional concepts for other ITER diagnostic systems and for a fusion reactor can be generated based on the generic design considerations.

# Bibliography

- [1] DIN ISO 9211-4:2006. Optics and optical instruments – Optical coatings – Part 4: Specific test methods, June 2008.
- [2] A. Ahmad. Low distortion mounting techniques for metal mirrors. In *SPIE conference on current developments in optical design and engineering VII*, 1998.
- [3] P. Allan, A.B. Loving, H. Omran, S. Collins, J. Thomas, A. Parsloe, I. Merrigan, and I. Hassall. Remote handling installation of diagnostics in the JET tokamak. *Fusion Engineering and Design*, 86(9–11):1821–1824, 2011. Proceedings of the 26th Symposium of Fusion Technology (SOFT-26).
- [4] ANSYS, Inc. ANSYS home page. <http://www.ansys.com/>. Online; accessed 15 Jan 2014.
- [5] Frank M. Anthony. High heat load optics: an historical overview. *Optical Engineering*, 34(2):313–320, 1995.
- [6] V. Barabash. In-vessel Components Structural Design Criteria (SDC-IC). ITER Organisation technical document. v3.0. 16-Nov-2012.
- [7] V. Barabash. ITER Material Properties Handbook (mph). ITER Organisation technical document.
- [8] H.-W. Bartels, E. Cheng, M. Gaeta, B. Merrill, and D. Petti. Decay heat removal in the ITER outline design. *Fusion Engineering and Design*, 31(3):203–219, 1996.
- [9] P. Batistoni, J. Likonen, N. Bekris, S. Brezinsek, P. Coad, L. Horton, G. Matthews, M. Rubel, G. Sips, B. Syme, and A. Widdowson. The JET technology program in support of ITER. *Fusion Engineering and Design*, 89(7–8):896–900, 2014. Proceedings of the 11th International Symposium on Fusion Nuclear Technology-11 (ISFNT-11) Barcelona, Spain, 15–20 September, 2013.
- [10] M. Benchikhoun, A. Dammann, A. Gray, V. Ivanov, R. O’Connor, N. Smith, and D. van Houtte. Operability of the ITER Hot Cell Facility. *Fusion Engineering and Design*, 86(9–11):1894–1897, 2011. Proceedings of the 26th Symposium of Fusion Technology (SOFT-26).
- [11] W. Biel, T. Baross, P. Bourauel, D. Dunai, M. Durkut, G. Erdei, N. Hawkes, M.v. Hellermann, A. Hogenbirk, R. Jaspers, G. Kiss, F. Klinkhamer, J.F. Konig, V. Kotov, Y. Krasikov, A. Krimmer, O. Lischtschenko, A. Litnovsky,

- O. Marchuk, O. Neubauer, G. Offermanns, A. Panin, K. Patel, G. Pokol, M. Schrader, B. Snijders, V. Szabo, N. van der Valk, R. Voinchet, J. Wolters, and S. Zoletnik. Overview on R&D and design activities for the ITER core charge exchange spectroscopy diagnostic system. *Fusion Engineering and Design*, 86:548–551, 2011. Proceedings of the 26th Symposium of Fusion Technology (SOFT-26).
- [12] Wolfgang Biel, Marco de Baar, Andreas Dinklage, Federico Felici, Ralf König, Hans Meister, Wolfgang Treutterer, and Ronald Wenninger. DEMO diagnostics and burn control. *Fusion Engineering and Design*, 2015, In Press.
- [13] C. Bläsius. FEM simulation and design optimization of mirrors for ITER core CXRS diagnostics system with regards to geometrical stability under operational loads. Master’s thesis, Rheinisch-Westfälische Technische Hochschule Aachen, Sep 2013.
- [14] C. Bläsius. Remote handling concept for the secondary mirrors two and three of ITER cCXRS. Technical report, FZJ, 2013.
- [15] M. F. Bloom. Thermal contact conductance in a vacuum environment. Technical report, Douglas Aircraft Company, Inc. Missile & Space systems Division, 1964.
- [16] Peter Bourauel. *Neutronic Analysis for ITER CXRS Diagnostic Upper Port-Plug*. PhD thesis, Università di Bologna, 2010.
- [17] D. L. Brower, B. H. Deng, and W. X. Ding. Divertor interferometer diagnostic for ITER. *Review of scientific instruments*, 77:10E911, 2006.
- [18] Carl Zeiss AG. ZEISS ACCURA product page. [http://www.zeiss.co.uk/industrial-metrology/en\\_gb/products/systems/bridge-type-cmms/accura.html](http://www.zeiss.co.uk/industrial-metrology/en_gb/products/systems/bridge-type-cmms/accura.html). Online; accessed 20 Jan 2015.
- [19] S. Chiochio. Project Requirements v4.6. Internal requirements document ITER Organization, May 2010.
- [20] M. Clever, G. Arnoux, N. Balshaw, P. Garcia-Sanchez, K. Patel, G. Sergienko, D. Soler, M. F. Stamp, J. Williams, K-D Zastrow, and JET-EFDA Contributors. A wide angle view imaging diagnostic with all reflective, in-vessel optics at JET. *Fusion Engineering and Design*, 88(6–8):1342–1346, Oct. 2013. 27th Symposium on Fusion Technology (SOFT), Liege, Belgium, Sep 24–28, 2012.
- [21] A. Costley. SRD-55 (diagnostics). ITER Organisation technical document. v3.1. 16 Nov 2009.
- [22] A.E Costley, D.J Campbell, S Kasai, K.E Young, and V Zaveriaev. ITER R&D: Auxiliary systems: Plasma diagnostics. *Fusion Engineering and Design*, 55(2–3):331–346, 2001.
- [23] Alan E. Costley. Towards diagnostics for a fusion reactor. *IEEE Transactions on Plasma Science*, 38:2934–2943, 2010.

- [24] Horst Czichos and Karl-Heinz Habig. *Tribologie-Handbuch Kapitel 16: Vakuumtribologie*. Vieweg+Teubner; Springer, 2010.
- [25] O. David, A.B. Loving, J.D. Palmer, S. Ciattaglia, and J.P. Friconneau. Operational experience feedback in JET Remote Handling. *Fusion Engineering and Design*, 75–79(0):519–523, 2005. Proceedings of the 23rd Symposium of Fusion Technology SOFT 23.
- [26] O. G. Dell. SRD-26-PH and -CV and -DR and -DY (TCWS). ITER Organisation technical document. v4.0. 14 Mar 2012.
- [27] O. G. Dell. SRD-26-PH and -CV and -DR and -DY (TCWS). ITER Organisation technical document. v5.1. 23 Dec 2013.
- [28] N. R. Draper and H. Smith. *Applied regression analysis (Wiley series in probability and statistics)*. Wiley-Interscience, 1998.
- [29] D. Edinger, P. Mammini, and A. Rao. Cryogenic mirror mounts for use on JWST’s NIRCам instrument. *Proc. SPIE 5904, Cryogenic Optical Systems and Instruments XI*, 2005.
- [30] G. Federici, R. Kemp, D. Ward, C. Bachmann, T. Franke, S. Gonzalez, C. Lowry, M. Gadowska, J. Harman, B. Meszaros, C. Morlock, F. Romanelli, and R. Wenninger. Overview of EU DEMO design and r&d activities. *Fusion Engineering and Design*, 89(7–8):882–889, 2014. Proceedings of the 11th International Symposium on Fusion Nuclear Technology-11 (ISFNT-11) Barcelona, Spain, 15–20 September, 2013.
- [31] P. Gohil, K.H. Burrell, R.J. Groebner, J. Kim, W. C. Martin, E. L. McKee, and R.P. Seraydarian. The charge exchange recombination diagnostic system on the DIII-D tokamak. In *Fusion Engineering, 1991. Proceedings., 14th IEEE/NPSS Symposium on*, pages 1199–1204 vol. 2, 1991.
- [32] Granta Design Ltd. CES EduPack product page. <http://www.grantadesign.com/education/edupack/>. Online; accessed 13 Feb 2015.
- [33] Yuri Gribiv. DINA simulation of 15MA DT scenario. ITER Organisation technical document. Jan. 2010.
- [34] D. Guilhem, J.L. Bondil, B. Bertrand, C. Desgranges, M. Lipa, P. Messina, M. Missirlian, C. Portafaix, R. Reichle, H. Roche, and A. Saille. Tore-supra infrared thermography system and a real steady-state diagnostic. *Fusion Engineering and Design*, 74:879–883, 2005. Proceedings of the 23rd Symposium of Fusion Technology SOFT 23.
- [35] J. How and R. Reichle. Plant Description (PD). ITER Organisation technical document. v1.1. 09 Oct 2009.

- [36] A. Huber, S. Brezinsek, Ph. Mertens, B. Schweer, G. Sergienko and A. Terra, G. Arnoux, N. Balshaw, M. Clever, T. Edlingdon, S. Egner, J. Farthing, M. Hartl, L. Horton, D. Kampf, J. Klammer, H. T. Lambertz and G. F. Matthews, C. Morlock, A. Murari, M. Reindl, V. Riccardo, U. Samm, S. Sanders, M. Stamp, J. Williams, K. D. Zastrow, C. Zauner, and JET-EFDA Contributors. Development of a mirror-based endoscope for divertor spectroscopy on JET with the new ITER-like wall. *Review of Scientific Instruments*, 83, 2012.
- [37] A. Huber, S. Brezinsek, Ph. Mertens, B. Schweer, G. Sergienko, A. Terra, G. Arnoux, N. Balshaw, M. Clever, T. Edlingdon, S. Egner, J. Farthing, M. Hartl, L. Horton, D. Kampf, J. Klammer, H.T. Lambertz, G.F. Matthews, C. Morlock, A. Murari, M. Reindl, V. Riccardo, U. Samm, S. Sanders, M. Stamp, J. Williams, K.D. Zastrow, and C. Zauner. A new radiation-hard endoscope for divertor spectroscopy on JET. *Fusion Engineering and Design*, 88(6–8):1361–1365, 2013. Proceedings of the 27th Symposium On Fusion Technology (SOFT-27); Liège, Belgium, Sep 24–28, 2012.
- [38] Institute for Micro Process Engineering (IMVT) at the Karlsruhe Institute for Technology (KIT). KIT - IMVT home page. <http://www.imvt.kit.edu/>. Online; accessed 14 Feb 2015.
- [39] ITER Organization. 2014. ITER project website. <https://www.iter.org/>. Online; accessed 26 Oct 2014.
- [40] J. Jacquinet, M. Keilhacker, and P.-H. Rebut. Mission and highlights of the JET joint undertaking: 1978–1999. *Fusion Science and Technology*, 53(4):866–890, May 2008.
- [41] Joanny, M., Travere, J. M., Salasca, S., Marot, L., Meyer, E., Thellier, C., Cammarata, C., Gally, G., Ferme, and J.-J. Achievements on engineering and manufacturing of ITER first-mirror mock-ups. *Plasma Science and IEEE Transactions on*, 40:692–696, 2012.
- [42] P.K. Kaw and I. Bandyopadhyay. *Fusion Physics, Chapter 1: The case for fusion*. International Atomic Energy Agency (IAEA), 2012.
- [43] F. Klinkhamer and K. Moddemeijer. Optical configurations for the core CXRS diagnostics for ITER. *Fusion Engineering and Design*, 86:1178–1181, 2011. Proceedings of the 26th Symposium of Fusion Technology (SOFT-26).
- [44] J.F. Koning, M.R. de Baar, B.S.Q. Elzendoorn, C.J.M. Heemskerck, D.M.S. Ronden, and W.J. Schuth. Analysis of ITER upper port plug remote handling maintenance scenarios. *Fusion Engineering and Design*, 87(5–6):515–519, 2012. Tenth International Symposium on Fusion Nuclear Technology (ISFNT-10).
- [45] I. G. Korshunov, V. I. Cheranov, and B. N. Tarasov. Influence of media interface on thermophysical properties of bimetallic structures. *Butlerovskie Soobshcheniya*, 10:275–276, 2002.

- [46] V. Kotov. Calculation of the core cxrs mirror heat loads with the software b2-eirene. private communication., 2013.
- [47] V. Kotov, D. Reiter, A. S. Kukushkin, A. Krimmer, A. Kirschner, S. Wiesen, and P. Börner. Final report on the ITER service contract C4T/09/71/OLT/CHD/DIAGNOSTIC: Study on effective fluxes to the first mirror which face the plasma directly. Technical report, ITER Organization, 2011.
- [48] V. Kotov, D. Reiter, A.S. Kukushkin, and H.D. Pacher. Numerical estimates of the ITER first mirrors degradation due to atomic fluxes. *Fusion Engineering and Design*, 86:1583–1586, 2011. Proceedings of the 26th Symposium of Fusion Technology (SOFT-26).
- [49] Yu. Krasikov, T. Baross, W. Biel, A. Litnovsky, N. Hawkes, G. Kiss, J.F.F. Klinkhamer, J.F. Koning, A. Krimmer, O. Neubauer, and A. Panin. Development of design options for the port plug components of the ITER core CXRS diagnostic. *Fusion Engineering and Design*, 86:2055–2059, 2011. Proceedings of the 26th Symposium of Fusion Technology (SOFT-26).
- [50] A. Kumar, R.K. Soni, P. Ganesh, R. Kaul, V.K. Bhatnagar, J. Dwivedi, and L.M. Kukreja. A study on low magnetic permeability gas tungsten arc weldment of AISI 316LN stainless steel for application in electron accelerator. *Materials & Design*, 53(0):86 – 92, 2014.
- [51] K. J. Leonard, G. E. Jellison, N.A.P. K. Kumar, and L. L. Snead. The role of microstructure on the optical performance of neutron irradiated dielectric mirrors. *Journal of Nuclear Materials*, 445(1–3):281–290, 2014.
- [52] H.P.H. Liddell, K. Mehrotra, J. C. Lambropoulos, and S. D. Jacobs. Fracture mechanics of delamination defects in multilayer dielectric coatings. *Appl. Opt.*, 52(32):7689–7698, Nov 2013.
- [53] A. Litnovsky, M. Matveeva, A. Herrmann, V. Rohde, M. Mayer, K. Sugiyama, K. Krieger, V. Voitsenya, G. Vayakis, A.E. Costley, R. Reichle, G. De Temmerman, S. Richter, U. Breuer, L. Buzi, S. Möller, V. Philipps, U. Samm, P. Wienhold, and the ASDEX Upgrade Team. First studies of ITER-diagnostic mirrors in a tokamak with an all-metal interior: results of the first mirror test in ASDEX Upgrade. *Nuclear Fusion*, 53(7):073033, 2013.
- [54] A. Litnovsky, G. De Temmerman, K. Vukolov, P. Wienhold, V. Philipps, O. Schmitz, U. Samm, G. Sergienko, P. Oelhafen, M. Büttner, I. Orlovskiy, A. Yastrebkov, U. Breuer, and A. Scholl. Investigations of single crystal and polycrystalline metal mirrors under erosion conditions in TEXTOR. *Fusion Engineering and Design*, 82(2):123–132, 2007.
- [55] A. Litnovsky, V. Voitsenya, T. Sugie, G. De Temmerman, A.E. Costley, A.J.H. Donné, K.Yu. Vukolov, I. Orlovskiy, J.N. Brooks, J.P. Allain, V. Kotov, A. Semerok, P.-Y. Thro, T. Akiyama, N. Yoshida, T. Tokunaga, and K. Kawahata.

- Progress in research and development of mirrors for ITER diagnostics. *Nuclear Fusion*, 49(7):075014, 2009.
- [56] Los Alamos National Laboratory. Monte carlo code group. <https://mcnp.lanl.gov/>. Online; accessed 03 Mar 2014.
- [57] A. Loving, O. Crofts, N. Sykes, D. Iglesias, M. Coleman, J. Thomas, J. Harman, U. Fischer, J. Sanz, M. Siuko, and M. Mittwollen. Pre-conceptual design assessment of DEMO remote maintenance. *Fusion Engineering and Design*, 89(9–10):2246–2250, 2014. Proceedings of the 11th International Symposium on Fusion Nuclear Technology-11 (ISFNT-11) Barcelona, Spain, 15–20 September, 2013.
- [58] C.V. Madhusudana. Gas gap conductance. In *Thermal Contact Conductance*, Mechanical Engineering Series, pages 45–63. Springer New York, 1996.
- [59] W. Mandl, R. C. Wolf, M. G. von Hellermann, and H. P. Summers. Beam emission spectroscopy as a comprehensive plasma diagnostic tool. *Plasma Physics and Controlled Fusion*, 35(10):1373–1394, 1993.
- [60] P. Marmy, D. Ringer, and U. Stiefel. Friction and wear in the hostile environment of a tokamak. *Fusion Engineering and Design*, 13:307–311, 1990.
- [61] L. Marot, G. Covarel, M.-H. Tuilier, R. Steiner, and P. Oelhafen. Adhesion of rhodium films on metallic substrates. *Thin Solid Films*, 516(21):7604–7608, 2008.
- [62] G.F. Matthews, M. Beurskens, S. Brezinsek, M. Groth, E. Joffrin, A. Loving, M. Kear, M.-L. Mayoral, R. Neu, P. Prior, V. Riccardo, F. Rimini, M. Rubel, G. Sips, E. Villedieu, P. de Vries, M.L. Watkins, and EFDA-JET contributors. JET ITER-like wall—overview and experimental programme. *Physica Scripta*, 2011(T145):014001, 2011.
- [63] Max-Planck-Institut für Plasmaphysik. <http://www.ipp.mpg.de>. Online; Internal section; accessed 11 Feb 2014.
- [64] F. Meo, H. Bindslev, S. B. Korsholm, E. L. Tsakadze, C. I. Walker, P. Woskov, and G. Vayakis. Design of the collective thomson scattering diagnostic for international thermonuclear experimental reactor at the 60 GHz frequency range. *Review of Scientific Instruments*, 75(10):3585–3588, 2004.
- [65] A. Merstallinger, E. Semerad, and B. D. Dunn. Cold welding due to impact and fretting under high vacuum. In K. Fletcher, editor, *Materials in a Space Environment*, volume 540 of *ESA Special Publication*, pages 343–350, Sep 2003.
- [66] Ph. Mertens, D. Castaño-Bardawil, W. Biel, S. Friese, N. Hawkes, R. Jaspers, V. Kotov, Y. Krasikov, A. Krimmer, A. Litnovsky, O. Marchuk, O. Neubauer, G. Offermanns, A. Panin, G. Pokol, M. Schrader, and U. Samm. Status of the R&D activities to the design of an ITER core CXRS diagnostic system. *Fusion Engineering and Design*, 2015, In Press.

- [67] B. Meszaros, G. Porempovics, and M.J. Walsh. Preliminary investigation of optical-path-related elements in the port plug of ITER core LIDAR diagnostics. *Plasma Science, IEEE Transactions on*, vol. 38(no.3):306–310, 2010.
- [68] Simon Mills, Bernhard Haist, and David Hamilton. A perspective on equipment design for fusion remote handling. *Fusion Engineering and Design*, 82(15–24):1983–1988, 2007. Proceedings of the 24th Symposium on Fusion Technology SOFT-24.
- [69] A. Moroño and E.R. Hodgson. Radioluminescence problems for diagnostic windows. *Journal of Nuclear Materials*, 224(3):216–221, 1995.
- [70] E.E. Mukhin, V.V. Semenov, A.G. Razdobarin, S. Yu. Tolstyakov, M.M. Kochergin, G.S. Kurskiev, K.A. Podushnikova, S.V. Masyukevich, D.A. Kirilenko, A.A. Sitnikova, P.V. Chernakov, A.E. Gorodetsky, V.L. Bukhovets, R. Kh. Zalavutdinov, A.P. Zakharov, I.I. Arkhipov, Yu.P. Khimich, D.B. Nikitin, V.N. Gorshkov, A.S. Smirnov, T.V. Chernozumskaja, E.M. Khilkevitch, S.V. Bulovich, V.S. Voitsenya, V.N. Bondarenko, V.G. Konovalov, I.V. Ryzhkov, O.M. Nekhaieva, O.A. Skorik, K. Yu. Vukolov, V.I. Khripunov, and P. Andrew. First mirrors in ITER: material choice and deposition prevention/cleaning techniques. *Nuclear Fusion*, 52(1):013017, 2012.
- [71] A. Nemov, V. Modestov, I. Buslakov, I.N. Loginov, I.V. Ivashov, A. Lukin, A.I. Borovkov, M.M. Kochergin, E.E. Mukhin, A.E. Litvinov, A.N. Koval, S.Yu. Tolstyakov, and P. Andrew. Development of ITER divertor Thomson scattering support structure design on the basis of engineering analyses. *Fusion Engineering and Design*, 89(7-8):1241–1245, 2014. Proceedings of the 11th International Symposium on Fusion Nuclear Technology-11 (ISFNT-11) Barcelona, Spain, 15–20 September, 2013.
- [72] I. Orlovskiy, E. Andreenko, K. Vukolov, T. Mukhammedzyanov, and A. Tobengauz. Broadband dielectric mirrors for optical diagnostics in ITER. *Fusion Engineering and Design*, 88(6–8):1284–1287, 2013. Proceedings of the 27th Symposium On Fusion Technology (SOFT-27); Liège and Belgium, Sep 24–28 and 2012.
- [73] I. Orlovskiy, K. Vukolov, E. Andreenko, T. Mukhammedzyanov, and A. Taranchenko. Thermal tests of broadband dielectric mirrors. *Fusion Engineering and Design*, 86:1290–1293, 2011.
- [74] I.I. Orlovskiy and K.Yu. Vukolov. Thermal and neutron tests of multilayered dielectric mirrors. *Fusion Engineering and Design*, 74:865–869, 2005.
- [75] P. R. Yoder and Jr. *Mounting optics in optical instruments*. SPIE Publications, 2nd edition edition, 2008.
- [76] A. Panin. Electromagnetic calculations of the CXRS-core ITER port plug and diagnostic components. Forschungszentrum Jülich IEK-4 internal technical report, 2011–12.

- [77] A.R. Raffray, B. Calcagno, P. Chappuis, Fu. Zhang, A. Furmanek, C. Jiming, D.H. Kim, S. Khomiakov, A. Labusov, A. Martin, et al. The ITER blanket system design challenge. *Nuclear Fusion*, 54:033004, 2014.
- [78] A.G. Razdobarin, P. Andrew, V.L. Bukhovets, I.M. Bukreev, P.V. Chernakov, A.E. Gorodetsky, M.M. Kochergin, A.N. Koval, G.S. Kurskiev, F. Leipold, A.E. Litvinov, A.V. Markin, S.V. Masyukevich, I.V. Miroshnikov, E.E. Mukhin, R. Reichle, D.S. Samsonov, V.V. Semenov, S. Yu. Tolstyakov, M.J. Walsh, R. Kh. Zalavutdinov, and A.P. Zakharov. RF discharge for in-situ mirror surface recovery in ITER. In *Poster at 25th IAEA Fusion Energy Conference - IAEA CN-221*, 2014.
- [79] A.G. Razdobarin, E.E. Mukhin, V.V. Semenov, S. Yu. Tolstyakov, M.M. Kochergin, G.S. Kurskiev, K.A. Podushnikova, D.A. Kirilenko, A.A. Sitnikova, A.E. Gorodetsky, V.L. Bukhovets, R.Kh. Zalavutdinov, D.P. Zakharov, I.I. Arkhipov, V.S. Voitsenya, V.N. Bondarenko, V.G. Konovalov, and I.V. Ryzhkov. High reflective mirrors for in-vessel applications in ITER. *Nuclear Instruments and Methods in Physics Research Section A: Accelerators and Spectrometers and Detectors and Associated Equipment*, 623(2):809 – 811, 2010. 1st International Conference on Frontiers in Diagnostics Technologies.
- [80] E. Rebhan, D. Reiter, R. Weynants, U. Samm, W. J. Hogan, J. Raeder, and T. Hamacher. *5 Controlled nuclear fusion: general aspects*, volume 3B of *Landolt-Börnstein - Group VIII Advanced Materials and Technologies*. Springer-Verlag Berlin Heidelberg, 2005.
- [81] J. Reich, W. Gardebrecht, B. Hein, B. Missal, J. Tretter, M. Wanner, F. Leher, and S. Langone. Manufacture of the vacuum vessels and the ports of Wendelstein 7-X. *Fusion Engineering and Design*, 75–79:565–569, 2005. Proceedings of the 23rd Symposium of Fusion Technology SOFT 23.
- [82] D. Reiter, M. Baelmans, and P. Börner. The EIRENE and B2-EIRENE codes. *Fusion Science and Technology*, 47(2):172–186, February 2005.
- [83] S. Rohem. MCNP radiation transport calculations for CXRS-core “Large M1” optical layout. Forschungszentrum Jülich IEK-4 internal technical report, Dezember 2012.
- [84] S1 Optics GmbH. Company home page. <http://www.s1optics.com/>. Online; accessed 18 Mar 2014.
- [85] G. Sannazzaro. Load Specifications (LS). ITER Organisation technical document. v6.0. 28 Apr 2012.
- [86] K. Sato, T.A. Stolarski, and Y. Iida. The effect of magnetic field on fretting wear. *Wear*, 241(1):99–108, 2000.
- [87] W. Schneider, B. Wiegel, F. Grünauer, R. Burhenn, S. Koch, H. Schuhmacher, and A. Zimbal. Neutron diagnostics at the Wendelstein 7-X stellarator. *Journal of Instrumentation*, 7(03):C03025, 2012.

- [88] SCHOTT AG. Data sheet SCHOTT N-BK7 517642.251. [http://www.us.schott.com/advanced\\_optics/english/abbe\\_datasheets/schott-datasheet-n-bk7.pdf](http://www.us.schott.com/advanced_optics/english/abbe_datasheets/schott-datasheet-n-bk7.pdf). Online; accessed 03 Mar 2015.
- [89] M. Shimada, M. Loughlin, and M. Shute. Heat and nuclear load specifications for ITER. Internal requirements document ITER Organization, November 2009.
- [90] Yu. P. Shlykov, Eu. A. Ganin, and S. N. Tsarevsky. Contact thermal resistance. "Energia", 1977. (In Russian).
- [91] Sigmadyne, Inc. *SigFit Reference Manual Version 2012R1f*. Sigmadyne, Inc.
- [92] Snead, LL, Leonard, K, Jellison Jr, GE, Sawan, Mohamed, Lehecka, and Tom. Irradiation effects on dielectric mirrors in inertial fusion power reactor application. *Fusion Science and Technology and USA*, 56:1069–1077, 2009.
- [93] R. Subramanian. ITER Remote Handling Code of Practice. ITER Organisation technical document. v1.2. 04 Jan 2010.
- [94] T. Sugie, T. Hatae, Y. Koide, T. Fujita, Y. Kusama, T. Nishitani, A. Isayama, M. Sato, K. Shinohara, N. Asakura, S. Konoshima, H. Kubo, H. Takenaga, Y. Kawano, T. Kondoh, A. Nagashima, T. Fukuda, H. Sunaoshi, O. Naito, S. Kitamura, Y. Tsukahara, A. Sakasai, Y. Sakamoto, T. Suzuki, K. Tobita, M. Nemoto, A. Morioka, M. Ishikawa, S. Ishida, N. Isei, N. Oyama, Y. Neyatani, K. Itami, S. Sakurai, H. Tamai, K. Tsuchiya, S. Higashijima, T. Nakano, S. Nagaya, S. Chiba, S. Lee, and M. Shitomi. Diagnostics system of JT-60U. *Fusion Science and Technology*, 42:482–511, 2002.
- [95] Thermacore, Inc. Thermacore home page. <http://www.thermacore.com>. Online; accessed 25 Apr 2015.
- [96] K. Tokunaga, T. Fujiwara, N. Yoshida, A. Ebihara, M. Tokitani, A. Sagara, S. Nagata, and B. Tsushiya. Optical property change on metmetal mirror materials by low energy helium irradiation. *J. Plasma Fusion Res.*, 8:1374–1378, 2009.
- [97] Alan C. Tribble. *Fundamentals of Contamination control*. SPIE press, 2000. .
- [98] unnamed. *ZEMAX Optical Design Program User's Guide*. ZEMAX Development corporation, 2006.
- [99] G. Vayakis, E. R. Hodgson, V. Voitsenya, and C. I. Walker. Chapter 12: Generic diagnostic issues for a burning plasma experiment. *Fusion Science and Technology*, 53(2):699–750, February 2008.
- [100] V. Voitsenya, A.E. Costley, V. Bandourko, A. Bardamid, V. Bondarenko, Y. Hirooka, S. Kasai, N. Klassen, V. Konovalov, M. Nagatsu, K. Nakamura, D. Orlinskij, F. Orsitto, L. Poperenko, S. Solodovchenko, A. Stan, T. Sugie, M. Taniguchi, M. Vinnichenko, K: Vukolov, and S. Zvonkov. Diagnostic first mirrors for burning plasma experiments (invited). *Review of Scientific Instruments*, 72(1):475–482, 2001.

- 
- [101] M. G. von Hellermann, G. Bertschinger, W. Biel, C. Giroud, R. Jaspers, C. Jupen, O. Marchuk, M. O'Mullane, H. P. Summers, A. Whiteford, and K-D. Zastrow. Complex spectra in fusion plasmas. *Physica Scripta*, T120:19–29, 2005.
- [102] K.Yu. Vukolov. Radiation effects in window materials for ITER diagnostics. *Fusion Engineering and Design*, 84:1961–1963, 2009.
- [103] C.A. Wang, M.L. Grossbeck, and B.A. Chin. Threshold helium concentration required to initiate cracking during welding of irradiated stainless steel. *Journal of Nuclear Materials*, 225(0):59–68, 1995.
- [104] Wen-Hsiang Wang and Shiuh Chao. Annealing effect on ion-beam-sputtered titanium dioxide film. *OPTICS LETTERS*, 23(18):1417–1419, September 1998.
- [105] M. Wanner, V. Erckmann, J.-H. Feist, W. Gardebrecht, D. Hartmann, R. Krampitz, H. Niedermeyer, H. Renner, Th. Rummel, F. Schauer, L. Wegener, F. Wesner, G.A. Möller, W. Kasperek, M. Thumm, and G. Dammertz. Status of Wendelstein 7-X construction. *Nuclear Fusion*, 43(6):416, 2003.
- [106] A.H. Wapstra and G. Audi. The 1983 atomic mass evaluation: (I). Atomic mass table. *Nuclear Physics A*, 432(1):1–54, 1985.
- [107] J. Wesson. *Tokamaks*. Clarendon press - Oxford, third edition edition, 2004.
- [108] J. Williams. KL11 in-vessel tube thermal analysis. Technical Report EAG09/T005, EFDA JET, 2009.
- [109] L. Worth. ITER Vacuum handbook v2.3. Internal design document ITER Organization, June 2009.
- [110] F. Zernike. Beugungstheorie des Schneidenverfahrens und seiner verbesserten Form, der Phasenkontrastmethode. *Physica I*, 1(7–12):689–704, 1934.
- [111] J. Zimmerman. Strain-free mounting techniques for metal mirrors. *Optical Engineering*, 20(2):202187–202187, 1981.

# List of symbols

Symbol	Meaning	Formula	Unit
A	Area		$m^2$
B	Magnetic field		$T$
E	Young's modulus		$N \cdot mm^{-2}$
$e^-$	'Electron'		
F	Force		$N$
H	Enthalpy		$J$
I	Electric current		$A$
$k_B$	Boltzmann constant		$8.617 \times 10^{-5} \text{ eV K}^{-1}$
L, l	Length		$m$
Q	Heat energy		$J$
q	Heat energy per area	$\frac{Q}{A}$	$J \cdot m^{-2}$
R	optical reflectance; reflectivity		1
Rx, Ry, Rz	Rotation around mirror local x, y, z		mrاد
$S_y$	Yield strength of a material		$N \cdot mm^{-2}$
T	Temperature		$^{\circ}\text{C}$
t	Time		$s$
V	Electric field		$V \cdot m^{-1}$
$X^0$	'Neutral atom'		
$X^{n+}$	'Atom with n-times positive charge'		
z	Thickness		$m$
$\alpha$	Instantaneous coefficient of thermal expansion	$\frac{1}{L} \frac{dL}{dT}$	$\text{K}^{-1}$

Symbol	Meaning	Formula	Unit
$\alpha_m$	Mean coefficient of thermal expansion over a temperature range $\Delta T$	$\frac{1}{L} \frac{\Delta L}{\Delta T}$	$K^{-1}$
$\dot{V}$	Volumetric heating		$W \cdot m^{-3}$
$\gamma$	'Photon'		
$\theta$	Angle to surface-normal incidence		$^\circ$
$\lambda$	Thermal conductivity		$W \cdot m^{-1} \cdot K^{-1}$
$\mu$	Magnetic permeability		$H \cdot m^{-1}$
$\mu_0$	Vacuum magnetic permeability		$4\pi \times 10^{-7} H \cdot m^{-1}$
$\rho$	Density		$kg \cdot m^{-3}$
$\varrho$	Electric resistivity	$\varrho = \frac{R \cdot A}{L}$	$\Omega \cdot m$

# List of abbreviations

---

Abbreviation	Definition
316L(N)-IG	The stainless steel grade 316, low carbon, controlled nitrogen in the ‘ITER Grade’ modification
ALARA	(principle) As low as reasonably achievable
BES	Beam emission spectroscopy
CFD	Computational fluid dynamics
CXRS-core	Charge exchange recombination spectroscopy on the plasma core (ITER)
DEMO	Demonstration fusion power plant
DOF	Degree of freedom
dpa	Displacements per atom
DSM	Diagnostic shield module
D-T	Deuterium-Tritium
EM	Electromagnetic
EP	Equatorial port (ITER)
FEM	Finite element method
FPY	Full power years
FZJ	Forschungszentrum Jülich
HIP	Hot isostatic pressing
ITER	ITER fusion reactor (name); also Latin for ‘The way’.
JT60U	Upgraded Japan Torus; fusion experiment
KL11	Port number KL11 in the JET fusion experiment
MCNP	Monte Carlo N-particle code
MSE	Motional Stark effect (ITER diagnostic system)

---

---

Abbreviation	Definition
PCS	Polycrystalline silicon
RH	Remote handling
SRD	System requirements document (ITER)
TCWS	Tokamak Cooling Water System (ITER)
TEXTOR	Tokamak EXperiment for Technology Oriented Research; fusion experiment
TIRR	Tolerance on surface IRRegularity (ZEMAX software)
UDW	Uniaxial diffusion welding
UP	Upper port (ITER)
UPP	Upper port plug (ITER)
VDE	Vertical displacement event
ZEMAX	Optical ray tracing software (name)

---

# Appendices

## A Fitting of optical tolerances

The node movement obtained by FEM software does not allow an immediate statement on the suitability of a design with regard to its optical performance. For example, ripples with an amplitude in the  $\mu\text{m}$  range might be out of specification while a change in focal length with an associated local node movement of some mm is acceptable.

To interpret the FEM result of a mirror, two approaches are available: ray tracing taking the deformed surface into account and splitting the surface deviations into a set of defined movements and surface aberration shapes for which tolerances are known. The ray tracing provides a definite answer on whether a certain mirror shape is acceptable or not, assuming that the FEM simulation is accurate. But the ray-tracing approach provides only limited information as to why a certain mirror shape may not be acceptable: All deformations are mixed together and the impact of single influences is masked.

More useful during initial development is the decomposition of node shifts into a set of rigid body movements, surface shape changes and aberrations. With the decomposed mirror surface changes, the effects of the loads can be understood, but a statement on mirror adequacy is trickier.

For numerical tolerance calculations and systems with shape deviations comparable to the classical aberrations such as tilt, focus and astigmatism, a convenient way of specifying the tolerances are the Zernike polynomials [110]. The fringe formulation of the Zernike polynomials, which is normalized to unity magnitude at the edge of the pupil may be written in the form

$$Z_{\text{even}}(\rho, \theta) = R_n^m(\rho)\cos(m\theta) \quad (\text{A.1})$$

$$Z_{\text{odd}}(\rho, \theta) = R_n^m(\rho)\sin(m\theta) \quad (\text{A.2})$$

where  $n, m \in \mathbb{Z}_{\geq 0}$ ,  $n - m \geq 0$  and even.  $\rho$  and  $\theta$  describe a unit circle in polar coordinates,  $0 \leq \rho \leq 1$  and  $0 \leq \theta < 2\pi$ . The radial polynomials  $R_n^m$  are 0 for  $n = m$  and, otherwise, are defined as

$$R_n^m(\rho) = \sum_{s=0}^{(n-m)/2} \frac{(-1)^s (n-s)!}{s!((n+m)/2-s)!((n-m)/2-s)!} \rho^{n-2s} \quad (\text{A.3})$$

The Zernike polynomials evaluated on a non-point-symmetric mirror are not orthonormal at higher orders, thereby losing one of the main advantages of this formulation.

As they are only used to communicate the tolerances in this work and are not evaluated for the classical aberration effects, no normalization of the polynomials to the mirror outside shape was done.

Fitting the rigid body motions and Zernike polynomials for the mirrors in fusion devices was found to be problematic because of the non-circular mirrors coupled with significant shifts and thermal expansion. Especially the thermal expansion of non-circular mirrors can lead to the calculation of a non-physical X and Y shift if not accounted for. In addition, the difference in absolute node shift for the different tolerances easily exceeds three orders of magnitude. Thus, it is critical that the fitting of the rigid body motion is accurate in order to still be able to calculate the remaining tolerances.

### A.1 ANSYS APDL script for tolerance fitting

The fitting procedure, as described in the following, was implemented in the ANSYS APDL scripting language. The script allows direct evaluation of the fitted results within the ANSYS FEM software and allows full control over all inputs for testing. The shape of the mirror surface is not limited.

The node location after meshing does not exactly coincide with the mirror surface as described by either the 3D model surface or mathematical description of the surface shape. In ANSYS version 14.4, the limit on position accuracy lies at 10 significant digits, which are used for communicating the node locations to the solver (see Figure A.1a). In addition, single nodes, especially on edges, are subject to additional initial shifts; see Figure A.1b for an example where the effect was found on mid-side nodes. No instance with accuracy of less than seven significant digits was found. The deviation of the nodes is small enough to not affect the thermal and mechanical simulation of the mirrors.

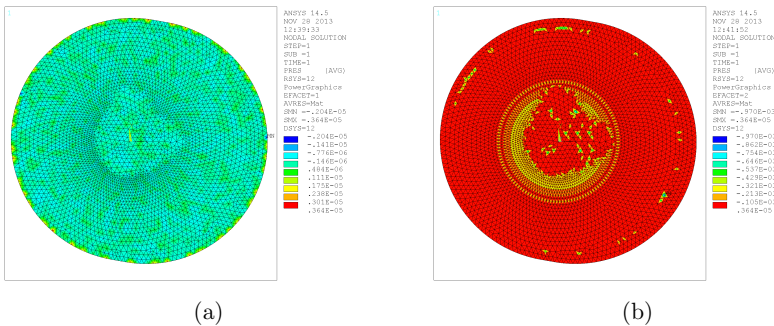


Figure A.1: Deviations in sag [mm] of meshes generated by the ANSYS Workbench. (a): Deviations in sag on edge nodes due from the limit of 10 significant digits with a 3D model located at 4 m from the model origin, calculated in mm. (b): Larger, single node deviations on mid-side nodes in the same model.

The six rigid body motions are calculated with the transformation also used by the software SigFit [91] and fitted by weighted linear least-squares regression analysis.

The transformation is linearised with a small-angle assumption in the three rotational directions. The best-fit node movement  $m_i$  is given by the formulas

$$m_{xi} = T_x + z_i * R_y - y_i * R_z \quad (\text{A.4})$$

$$m_{yi} = T_y - z_i * R_x + x_i * R_z \quad (\text{A.5})$$

$$m_{zi} = T_z + y_i * R_x - x_i * R_y \quad (\text{A.6})$$

where  $x_i$ ,  $y_i$  and  $z_i$  represent the deviated locations of the  $i$ -th node.  $T$  and  $R$  are the best-fit rigid body motion translations and rotations in directions  $x$ ,  $y$  and  $z$ . For the least squares fitting, the sum of the squared differences of node deviations  $d_i$  and single-node best-fit movements  $m_i$  is minimised. The weight for each node,  $w_i$ , is calculated from the surface area associated with the node.

$$\min\left(\sum_{i=0}^n w_i((d_{xi} - m_{xi})^2 + (d_{yi} - m_{yi})^2 + (d_{zi} - m_{zi})^2)\right) \quad (\text{A.7})$$

The rigid body motion is evaluated on a circular area around the mirror optical centre only (see Figure A.2). By restricting the fit of rigid body motion to an area point symmetric on the mirror centre, thermal expansion does not result in a lateral shift of the mirror. The circular shape is used as it allows a uniform mesh, minimising mesh influence. Restricting the fitting of rigid body motion to a smaller area on the surface does not pose a problem for the accuracy of the fit, as a mirror should not be warped to a degree where body motion fit is impacted significantly. Rotations in  $X$  and  $Y$  are not subtracted when non-point-symmetric Zernike polynomials are fitted.

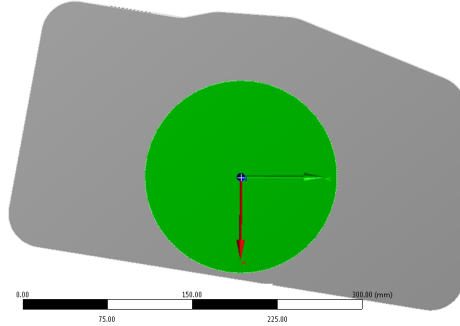


Figure A.2: Rigid body motion fitting is limited to nodes in a point-symmetric area centred on the optical centre to account for influences of thermal expansion. The Zernike polynomials are evaluated on the whole mirror surface.

Solving Equation A.7 can be reformulated as solving for  $b$  the expression [28]

$$X^T W X b = W^T W Y$$

with the matrices

$$b = \begin{pmatrix} T_x \\ T_y \\ T_z \\ R_x \\ R_y \\ R_z \end{pmatrix}, Y = \begin{pmatrix} m_{x1} \\ m_{y1} \\ m_{z1} \\ m_{x2} \\ \vdots \\ m_{zn} \end{pmatrix}, \quad (\text{A.8})$$

$$W = \begin{pmatrix} w_1 & 0 & 0 & 0 & \dots & 0 \\ 0 & w_1 & 0 & 0 & \dots & 0 \\ 0 & 0 & w_1 & 0 & \dots & 0 \\ 0 & 0 & 0 & w_2 & \dots & 0 \\ \vdots & \vdots & \vdots & \vdots & \ddots & \vdots \\ 0 & 0 & 0 & 0 & \dots & w_n \end{pmatrix} \text{ and } X = \begin{pmatrix} 1 & 0 & 0 & 0 & z_1 & -y_1 \\ 0 & 1 & 0 & -z_1 & 0 & x_1 \\ 0 & 0 & 1 & y_1 & -x_1 & 0 \\ 1 & 0 & 0 & 0 & z_2 & -y_2 \\ \vdots & \vdots & \vdots & \vdots & \vdots & \vdots \\ 0 & 0 & 1 & y_n & -x_n & 0 \end{pmatrix} \quad (\text{A.9})$$

where  $n$  is the number of nodes to fit. In cases where less than the full six DOF, as described by rigid body motion, are fitted, the matrices are assembled as required for the reduced case.

Rigid body shift and rotation are balanced after subtraction of the initial mesh aberration. The small-angle assumption is not used for rotating the body. By abstaining from the small angle linearization, artificial deformation of the mirror surface is avoided, which is especially prominent in the case of mirrors with short focal length and the relatively large rotation angles encountered in fusion diagnostic systems.

The tolerances based on the change in sag are fitted on the whole mirror surface. For the core CXRS system, weighted least-squares fitting of the formulas, as given in A.1 and A.3, is done for the desired set of aberrations. In case the rigid body motions movement in Z-direction (bias) and rotations around x and y (tip/tilt) are included, the resulting tolerances are added to the rigid body motions of the first fit to arrive at the best fit in the least-squares sense.

Surface irregularity is calculated as the residual change in sag after subtraction of all fitted shape deviations. The irregularity is calculated as peak-to-valley (P-V) and as a plot of the mirror surface area (see Figure 6.20 for examples).

## A.2 Achieved fitting accuracy

The accuracy of the fit achieved with the described method was tested by applying the script to models with deviations of known amplitude. It was found that the relationship of the fitting accuracy exhibits a complex relationship with the deviations applied, which was expected based on the non-linear behaviour of the least-squares fitting on the non-circular mirror surface. Because of this complex dependency of

fit accuracy and applied deviation, only deviations up to values relevant for the core CXRS were tested.

Testing was done by the fitting of test cases constructed in CATIA and ANSYS with known shifts, expansions and deviations. For deviations at the upper limit of core CXRS allowed tolerances, the six DOF for the rigid body motion were always fitted within 2% of the tolerance with thermal expansion of 70 °C present. With no thermal expansion, fitting succeeded within 0.02% of the tolerance, including all inaccuracies from the geometry description in .stp format, meshing errors and the limited accuracy of the math in ANSYS (variables as double). Based on the test cases, the script is considered capable to also fit the first four terms of the Zernike polynomials in the presence of the movements and thermal expansions, as encountered in core CXRS. Fitting of further Zernike aberrations seems feasible based on the results but was not tested.

## **B M2 welded prototype drawings**

The two drawings are of the front and rear plates of the diffusion-welded internal cooling channel prototype. The two plates are positioned during welding with two pins in the edges of the blocks outside the mirror substrate volume. The pin holes are not shown in the part drawings.







Band / Volume 328

**Conductivity and Structure of Sputtered ZnO:Al on Flat and Textured Substrates for Thin-Film Solar Cells**

N. Sommer (2016), vii, 195, XIV pp

ISBN: 978-3-95806-156-9

Band / Volume 329

**Glaslotfügen von Festoxid-Brennstoffzellen durch Laseraufschmelzung**

M. Willberg (2016), 99 pp

ISBN: 978-3-95806-157-6

Band / Volume 330

**The Role of Natural Nanoparticles and Colloids for Phosphorus Binding in Forested Headwater Catchments**

N. Gottselig (2016), VIII, 116 pp

ISBN: 978-3-95806-160-6

Band / Volume 331

**Numerische Modellierung der thermomechanischen Fluid-Struktur-Interaktion im SOFC-Stack**

A. Al-Masri (2016), iii, 165 pp

ISBN: 978-3-95806-161-3

Band / Volume 332

**Analysis of biomixtures to determine the fate of pesticides**

S. Mukherjee (2016), xix, 136 pp

ISBN: 978-3-95806-163-7

Band / Volume 333

**Temperature Dependence of Carbon Kinetic Isotope Effect for The Oxidation Reaction of Ethane by Hydroxyl Radicals Under Atmospherically Relevant Conditions: Experimental and Theoretical Studies**

T. Piansawan (2016), 196 pp

ISBN: 978-3-95806-166-8

Band / Volume 334

**Konzeption von Membranmodulen zur effizienten Abtrennung von Kohlendioxid aus Gasgemischen**

S. Luhr (2016)

ISBN: 978-3-95806-170-5

Band / Volume 335

**Einfluss fehlpassungsinduzierter Spannungsfelder auf den Transportprozess bei ionischer Leitung**

J. Keppner (2016), viii, 171 pp

ISBN: 978-3-95806-171-2

Band / Volume 336

**Production and Characterization of Monodisperse Uranium Particles for Nuclear Safeguards Applications**

A. Knott (2016), A-H, 123, xxviii, xiii pp

ISBN: 978-3-95806-172-9

Band / Volume 337

**3D hydrological simulation of a forested headwater catchment: Spatio-temporal validation and scale dependent parameterization**

Z. Fang (2016), XVII, 119 pp

ISBN: 978-3-95806-174-3

Band / Volume 338

**Influence of Thermomechanical Treatment on High Temperature Properties of Laves Phase Strengthened Ferritic Steels**

M. Talík (2016), xxiii, 130 pp

ISBN: 978-3-95806-175-0

Band / Volume 339

**Groundwater recharge in Slovenia  
Results of a bilateral German-Slovenian Research project**

Mišo Andjelov, Zlatko Mikulič, Björn Tetzlaff, Jože Uhan & Frank Wendland (2016)

ISBN: 978-3-95806-177-4

Band / Volume 340

**Atomic oxygen derived from SCIAMACHY O(<sup>1</sup>S)  
and OH airglow measurements in the Mesopause region**

Y. Zhu (2016), 206 pp

ISBN: 978-3-95806-178-1

Band / Volume 341

**Diagnostic Mirror Concept Development for Use in the Complex Environment of a Fusion Reactor**

A. Krimmer (2016), x, 123 pp

ISBN: 978-3-95806-180-4

Weitere *Schriften des Verlags im Forschungszentrum Jülich* unter  
<http://www.zb1.fz-juelich.de/verlagextern1/index.asp>



**Energie & Umwelt /  
Energy & Environment  
Band / Volume 341  
ISBN 978-3-95806-180-4**

